

SINGLE ELECTRON CAPTURE AND IONIZATION
INVOLVING ATOMIC (AND MOLECULAR) H AND HE AT
LOW TO INTERMEDIATE IMPACT ENERGIES

by

ERGE EDGÜ-FRY

B.Sc., Istanbul Technical University, Turkey, 1994

M.Sc., Bosphorus University, Turkey, 1996

A DISSERTATION

submitted in partial fulfillment of the
requirements for the degree of

DOCTOR OF PHILOSOPHY

Department of Physics
College of Arts and Sciences

KANSAS STATE UNIVERSITY
Manhattan, Kansas

2003

ABSTRACT

Single electron capture from atomic (and molecular) hydrogen by 0.32, 0.5 and 0.75 a.u. Ar^{8+} ions, and electron ejection from atomic hydrogen by 0.775, 1 and 1.415 a.u. protons and from helium by 0.895 to 2 a.u. protons were studied. Proton impact on helium experiments were done to close an existing energy gap studied in this system. Atomic hydrogen bombarded by a proton forms a true three body system which makes our ionization experiments involving atomic hydrogen unique. They are the first set of experiments which provide ejected electron momenta that can be compared without theoretical compromise to existing theories. Because hydrogen normally exists in nature as H_2 , it must be dissociated to obtain H . We have built a hydrogen source that dissociates molecular hydrogen used in both of the hydrogen experiments. This source consists of a discharge tube in a microwave cavity. The technique used for all these experiments is momentum imaging spectroscopy, whereby the partners of the collisions are detected in coincidence. From the electron-capture experiments, energy-gain information was extracted, which allowed us to determine into which states of the projectile ion the electron was captured. We obtained and compared results of atomic and molecular hydrogen targets. Our results showed that the electron was captured into the n -states expected from theory, but not in the ratios that were predicted. From our single ionization experiments involving both helium and atomic hydrogen targets, we were able to extract the ejected electron momentum spectra for different impact energies.

Contents

Table of Contents	i
List of Tables	iii
List of Figures	iv
Acknowledgement	ix
Dedication	xi
1 Introduction	1
2 Review of Low Energy Electron Capture Theory	5
2.1 Classical Over-The-Barrier Model	5
2.2 Quantum Mechanical Theory	11
2.2.1 Close Coupling Theory For One Electron Systems	12
3 Review of Low-Intermediate Energy Ionization Theory	15
3.1 The Collision Problem in Molecular Orbital Expansions	15
4 COLTRIMS Technique	22
4.1 Experimental Setup	22
4.2 Atomic Hydrogen Target	26
4.2.1 Slevin-Type Atomic Hydrogen Source	28
4.2.2 Evenson Cavity Microwave Discharge Atomic Hydrogen Source	31
5 Electron Capture Experiments	47
5.1 The Technique	47

5.2	Evaluation of Energy Gain	49
5.2.1	Calibration of $p_z = 0$	51
5.2.2	Time-of-Flight and Recoil Position Spectra	51
5.3	Results	56
5.3.1	$Ar^{8+} + H$	56
5.3.2	$Ar^{8+} + H_2$	61
6	Electron Momentum Imaging With A Helium Target	67
6.1	Results of $H^+ + He$ Experiment	70
6.1.1	Comparison of Theoretical and Experimental Results	75
7	Electron Momentum Imaging With An Atomic Hydrogen Target	80
7.1	The Experimental Method	80
7.2	Results Of $H^+ + H$ Experiments	87
8	Conclusions	95
9	Appendix	98
9.1	Electronics Setup	98
9.2	The Data Analysis Program For Capture Experiments	101
9.3	The Data Analysis Program For Ionization Experiments	110
	References	117

List of Tables

- 5.1 Timing parameters of the capture experiments. v is the beam velocity, p is projectiles, r is recoils, TOF is time-of-flight and d stands for ‘delayed by’. 49
- 5.2 Comparison of relative cross-sections in percent. Close-coupling calculations are done for $v = 0.3$ a.u. and the experimental results are for $v = 0.3$ a.u. 61
- 5.3 Comparison of relative cross-sections in percent. Close-coupling calculations are done for $v = 0.45$ a.u. and the experimental results are for $v = 0.5$ a.u. 62
- 5.4 Comparison of relative cross-sections in percent. Close-coupling calculations are done for $v = 0.7$ a.u. and the experimental results are for $v = 0.75$ a.u. 62

List of Figures

1.1	Cross-sections for proton impacts on atomic hydrogen at low collision velocities. (a) for charge transfer to 2s and 2p states of atomic hydrogen, (b) for ionization. Solid lines are the calculations of Fritsch and Lin. (adapted from [17])	4
2.1	Schematic of over-the-barrier model for an ion with charge 4+ incident on H. As the two centers come closer it can be seen that the potential barrier between them decreases. (Taken from [21])	10
3.1	Coordinate system used to describe the collision.	16
3.2	Electronic energy curves for H^{2+} .(Adapted from [22].)	17
3.3	Ejected electron momenta for a 10 keV He^+ beam on He . The left hand side of this figure show ejected electron velocity distributions scaled to the impact velocity. The right hand side shows projections of these distributions onto the transverse axis.	20
4.1	A schematic of the beamline.	23
4.2	Coordinate system and the setup of the detectors.	25
4.3	A schematic of the target setup (not to scale) showing the collision region.	27
4.4	Schematic of Slevin-type atomic hydrogen source	29

4.5	Arrangement of the atomic hydrogen source setup (not to scale)	32
4.6	Atomic hydrogen source.	33
4.7	The x-z manipulator for the atomic hydrogen source.	36
4.8	The gas ‘jet’ observed on the recoil ion detector for ionization of atomic hydrogen for 25 keV proton impact. the conversion from channels to atomic units of momentum is such that 8.5 channels correspond to one atomic unit for H^+	37
4.9	Sample TAC spectrum for $H^+ + H, H_2$ ionization at $25keV$ gated on the gas jet.	39
4.10	Sample wavelength spectrum in the discharge region.	41
4.11	A sketch of the nozzle-skimmer-beam crossing setup. The nozzle is 1 mm in diameter and the skimmer is 0.5 mm in diameter. The beam crosses the jet 50 mm upstream.	43
4.12	Expected momentum distribution of the target gas along the y direction. .	44
4.13	Velocity profile of the hydrogen target showing the thermal shift for the case of 25 keV proton impact on hydrogen. The squares correspond to all the data projected and the triangles correspond to the background hot gas projection along the y axis. The subtraction of background from the projection off all the data gives the resulting y distribution.	46
5.1	Pictures of the capture experiment setup.	48
5.2	(a) p_z , (b) Q -value and (c) Q vs θ for $v_p = 1$ a.u. protons on hydrogen. . . .	52

5.3	left hand side is the raw TAC spectra and right hand side is the recoil position spectra gated on the raw TAC spectra for Ar^{8+} on H and H_2 . The calibration for the TAC spectra is 1.7 ns/ch while for the position spectra it is 0.5 mm/ch, which corresponds to 8.5 ch/a.u. for H^+	54
5.4	left hand side is the raw recoil position spectra and right hand side is the TAC spectra gated on the raw position spectra. The calibrations are the same as Figure 5.3.	55
5.5	Q -value spectra for Ar^{8+} on H at $v_p = 0.32a.u.$	58
5.6	Q -value spectra for Ar^{8+} on H at $v_p = 0.5a.u.$	59
5.7	Q -value spectra for Ar^{8+} on H at $v_p = 0.75a.u.$	60
5.8	The potential energy curves for $(ArH)^{8+}$ molecule. Note the crossings at 7 – 10 a.u. and 20 a.u.	63
5.9	Q -value spectra for Ar^{8+} on H_2 at $v_p = 0.32a.u.$	64
5.10	Q -value spectra for Ar^{8+} on H_2 at $v_p = 0.5a.u.$	65
5.11	Q -value spectra for Ar^{8+} on H_2 at $v_p = 0.75a.u.$	66
6.1	(a) collision region showing the aperture, (b) top view of the spectrometer and the collision region showing the gas inlet.	69
6.2	Density plots of the electron velocity spectra projected onto the $x - z$ plane. The recoil momentum is defined to be in the $-y$ direction.	72
6.3	Longitudinal momentum distributions of the ejected electrons. (a) Experiment, (b) Theory ($b = 1.5$ a.u.). To guide the eye we have shifted each curve vertically by 0.25 for each increasing energy.	73

6.4	Transverse momentum distributions of the ejected electrons. (a) Experiment, (b) Theory ($b = 1.5$ a.u.). To guide the eye we have shifted each curve vertically by 0.25 for each increasing energy.	74
6.5	Calculated vt dependence of the momentum distributions for ejected electrons. (a) Transverse momentum at 20 keV, (b) transverse momentum at 100 keV, (c) longitudinal momentum at 20 keV and (d) longitudinal momentum at 100 keV. to guide the eye each curve is shifted vertically by 0.25 for each increasing energy.	77
7.1	Double aperture used to collimate the ion beam. The outer aperture has a 2,5 mm diameter while the other one has a 1 mm diameter.	82
7.2	left hand side is the raw TAC spectra and right hand side is the recoil position spectra gated on the raw TAC spectra.	83
7.3	p_{rx} vs p_{ry} and p_{rtr} vs phi for 25 keV proton impact on H . This plots are obtained after the gates are set on events corresponding to H^+ coincidences and ionization.	84
7.4	Recoil ions directed on to the electron detector. The center of the detector is observed at $(z, y) = (52, 62)$	86
7.5	v_{ey}/v_p vs v_{ez}/v_p for proton impacts at 15, 25 and 50keV.	88
7.6	Projections of Figure 7.5 onto the longitudinal axis.	89
7.7	Projections of Figure 7.5 onto the transverse axis.	90
7.8	Results from [14] for 15 and 25 keV. These are calculated projections of electron velocity distributions on to the transverse axis. The recoil ions are moving along $-y$ direction.	91

7.9	v_{ey}/v_p vs v_{ez}/v_p for 25 keV proton impact on H , showing different choices of the transverse momentum.	92
7.10	Projections of figure 7.9 on to the beam axis.	93
7.11	Projections of figure 7.9 transverse to the beam axis.	94
9.1	Block diagram of basic electronics for capture experiments. The abbreviations used are FTA: fast timing amplifier, TFA: timing filter amplifier, CFD: constant fraction discriminator, TAC: time-to-amplitude converter, GDG: Gate and delay generator, ADC: analog-to-digital converter.	99
9.2	Block diagram of basic electronics for ionization experiments. The abbreviations used are FTA: fast timing amplifier, TFA: timing filter amplifier, CFD: constant fraction discriminator, TAC: time-to-amplitude converter, GDG: Gate and delay generator, ADC: analog-to-digital converter.	100

Acknowledgement

Over the course of my studies many people have helped me. My advisor, Lew Cocke has been a great role model and thought me how to think like a ‘scientist’. I can not thank him enough for his guidance and patience through the years. I also would like to thank Pat Richard for following my research closely. Starting from my first days of graduate school here, Larry Weaver’s door was always open for questions and he always challenged me to think harder.

I thank my undergraduate and Masters advisor Avadis Hacinliyan for convincing me to pursue my studies in the States. He is not only a good friend, but also a great teacher.

I have learned a great deal on vacuum technology, electronics and mechanics from Mike Wells. Without him I don’t know how I could have finished this work. Charles Fehrenbach was always available to help with the ion sources, even at the last minute. Whenever I had problems with the computers I ran down to Vince Needham and Kevin Carnes’ office whom always had a smile on and helped me no matter how much time I demanded of them.

Itzhik Ben-Itzhak and Chii-Dong Lin were not only helpful in the classes I took from them, but also were there to challenge me at times during this work. The greater JRM family has helped me over the years. Among those, Al Rankin, Bob Geering, Scott Chainey, Ron Jackson, Dave Hill, Tracy Tipping and Dea Richard are only a few. Kim Coy, Jane Peterson, Peggy Matthews and Deanna Selby were not only great friends, but always helped with the administrative issues.

Over the years I had the privilege of being able to discuss my work and share ideas with my friends and colleagues Ingrid Reiser, Emil Sidky, Teck Lee, Mohammad Abdallah, Allen Landers and Timur Osipov. Through the REU program I got the chance to work with Jeff Stuhlman who proved to be a great working partner. A lot of his time and patience is also represented in this work.

Of course I would not even be here today if it was not for my dear mom and dad, Fahiman and Erdinç Edgü. They are the ones who first thought me to love science. They have always believed in me and supported me no matter the choices I make. I will forever be in debt to them. My second set of parents, Dan and Pam Williams were always supportive and helped me through the roughest of times. I also would like to thank the extended Fry Family for taking me in as their own. My sister Erincik Edgü has been great support through the years, we had the chance to become ‘doctors’ together and gave each other the

push whenever the other one was lacking motivation.

Most importantly, I must thank my dear husband, Danny Fry for his patience and love. We have been through very rough times during the course of our graduate work and I always kept my head above water with the pull of of his hand. I only hope he is half as proud of me as I am of him.

Dedication

to my angels: Erin, Lara (01/15/01) and Maya (04/21/03)

two in my arms, one in His

Chapter 1

Introduction

Ionization and capture are two possible outcomes of an ion colliding with an atomic or a molecular target. In this thesis, we understand the term ionization to mean a process whereby an atom loses one (or more) of its electrons to the continuum. When the target atom loses its electron to the projectile then this process is called capture. In this thesis we deal with both low-energy ionization and capture processes. ‘Low-energy’ collisions are those with impact velocities comparable to or less than the classical bound-electron velocity. These processes take place in interstellar environments and low-temperature plasmas. These are some possible applications. However, the purpose of this study is basic advancement of understanding the details of electron capture and ionization in low and intermediate-energy collisions.

Our main goal in this work is to study ionization and capture in collisions with true one-electron targets since these are the ones that can be directly compared to existing theories. To be able to achieve this goal we study a series of collision systems. The measurements discussed here can be grouped into three different projects: (1) the capture of an electron from both atomic and molecular hydrogen targets by an Ar^{8+} beam (2) the ionization of He by proton impact and (3) the ionization of atomic hydrogen by proton impact.

To study these collisions, we use COLTRIMS (COLd Target Recoil Ion Momentum Spectroscopy) which allows us to reconstruct the full momentum vector of both ions and continuum electrons after the collision. This way we are able to determine the scattering plane, the impact parameter, and the energy release during the collision.

In Chapters 2 and 3 we give a brief theoretical review of theories that apply to low-energy ionization and capture mechanisms. The experimental technique and apparatus is described in detail in Chapter 4. Initially we describe the momentum imaging technique used widely in the literature [1, 2]. With this technique we are able to extract ejected electron velocity distributions for the case of ionization and energy release spectra for capture processes. In the second part of Chapter 4 we give details on the atomic hydrogen source used for the hydrogen experiments. This source is similar to the source used by Paolini et. al. [3]. It is very difficult to obtain an atomic hydrogen target that is ‘cold’ for use in COLTRIMS. We describe in detail how cold a target this source and the setup provides.

In Chapter 5 we give a brief discussion about the energy gain method used for the capture experiments followed by the results of our capture experiments. The main goal of these measurements is to identify the state-selective capture processes. Several groups have reported both experimental [4, 5, 6] and theoretical [7, 8, 9] work in this area. For the case of single electron capture, the final momentum of the target ion gives the electronic energy release in the reaction. The reason we choose Ar^{8+} as the projectile is due to the fact that it is a nearly one-electron ion, yet angular momentum splitting for the states the captured electron populates can be observed.

Chapter 6 gives the results of our first ionization experiments which involved a helium

target. Helium was chosen as a target due to its simplicity and also due to the fact that we can get ‘cold’ helium. These experiments bridged an existing gap in projectile energy between the low-energy ‘molecular’ region and the high-energy ‘perturbative’ region.

The results of the atomic hydrogen target ionization experiments are given in Chapter 7. In the low-energy collisions the basic mechanisms which lead to continuum electron production are poorly understood. The choice of using an atomic hydrogen target was made because this is the true one-electron target. Collisions at low projectile energies are dominated mostly by capture; ionization here is a very weak process. This can be seen in for example Figure 1.1. It was realized first by Olson [10] that at low energies the two-center effect on the electron from both the target center and the projectile center needed to be taken into account. He noted in classical trajectory monte carlo (CTMC) calculations that a large fraction of the electrons were emitted with velocities half the projectile velocity. These electrons have become known as ‘saddle-point’ electrons. This saddle-point refers to the point where the electron feels equal and opposite forces from both centers. After Olson, several groups have looked at ejected electron velocity distributions both theoretically [11, 12, 13, 14] and experimentally [15, 16].

We conclude our thesis with Chapter 8 summarizing what we have achieved in this thesis with a discussion of where the measurements should be carried out to in the future.

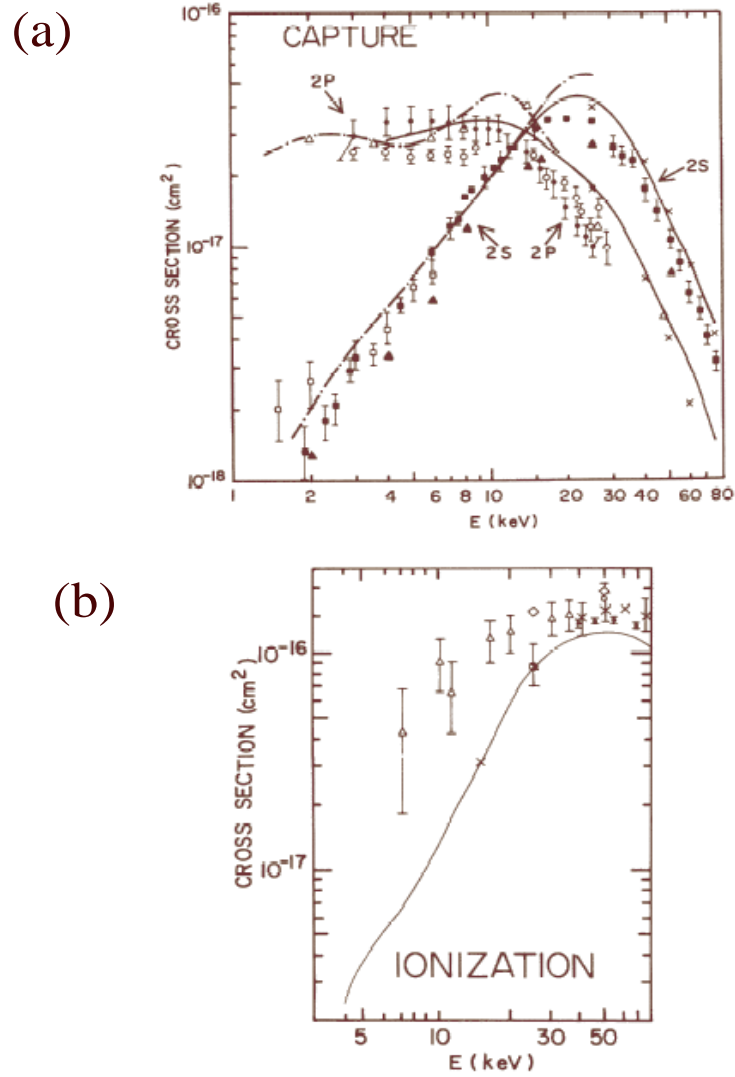


Figure 1.1: Cross-sections for proton impacts on atomic hydrogen at low collision velocities. (a) for charge transfer to 2s and 2p states of atomic hydrogen, (b) for ionization. Solid lines are the calculations of Fritsch and Lin. (adapted from [17])

Chapter 2

Review of Low Energy Electron Capture Theory

In this section we will focus on single electron capture or single charge exchange. Such a process in general is defined as:



where A^{q+} is the projectile ion, B is the target atom and ΔE is the kinetic energy release (or Q value) of the collision. First we will introduce a classical picture and see how parameters such as the collision velocity v and the charge state of the projectile q effect the outcome of the collision. Afterwards we will give a review of more rigorous quantum mechanical models applied to single electron capture in the low-energy regime.

2.1 Classical Over-The-Barrier Model

The over-the-barrier model was first introduced by Bohr and Lindhard [18] and was further extended to include a velocity dependence [19]. Bohr and Lindhard introduced two ion-atom interaction distances: release and capture radii. The electron can be released from the target nucleus when the projectile is close enough so that the force exerted by it on the

electron is equal to the binding force of the electron in the atom, i.e., when:

$$\frac{qe^2}{R_{rel}^2} = \frac{m_e v_e^2}{a} \quad (2.1.1)$$

where m_e , v_e and a are the mass, velocity and the orbital radius of the electron, respectively.

The release distance is then:

$$R_{rel} = (qaa_0)^{1/2}(v_0/v_e) \quad (2.1.2)$$

where $v_0 = e^2/\hbar$ is the first Bohr orbital velocity and $a_0 = \hbar^2/me^2$ is the corresponding orbital radius. In atomic units v_0 and a_0 are equal to 1. (Hereafter atomic units will be used). Equation 2.1.2 then reads:

$$R_{rel} = (qa)^{1/2}(1/v_e). \quad (2.1.3)$$

Bohr and Lindhard assume that the condition for capture to take place is that the potential energy of the electron is larger than its kinetic energy in the ion frame. The limiting condition for capture to happen at an internuclear distance $R = R_{cap}$ is given as:

$$\frac{q}{R_{cap}} = \frac{1}{2}v^2 \quad (2.1.4)$$

where v is the projectile ion velocity. Hence, capture is possible when $R \leq R_{cap}$ or:

$$R_{cap} = \frac{2q}{v^2}. \quad (2.1.5)$$

When $R_{rel} \leq R_{cap}$, the ion is close enough for release to take place and the cross-section for capture is:

$$\sigma_1 = \pi R_{rel}^2 = \pi qa \left(\frac{1}{v_e^2} \right). \quad (2.1.6)$$

Note that Equation 2.1.6 does not depend on the projectile-ion velocity v .

On the other hand, when $R_{rel} > R_{cap}$, release can take place before capture is possible. However, release is a gradual process and the time during which capture can happen is approximately R_{cap}/v . The capture cross-section then becomes:

$$\sigma_2 = \pi R_{cap}^2 \left(\frac{v_e R_{cap}}{a v} \right) \propto v^{-7}. \quad (2.1.7)$$

From these results, it can be seen that for low ion velocities, the cross-section for capture from a one-electron target is independent of the projectile-ion velocity v and for higher velocity ions it is proportional to v^{-7} . Comparisons of this model to actual experimental cross-sections can be found in for example [20]. As can be seen in Figure 1 of Chapter 1, as the ion velocity increases capture becomes a weaker process and ionization starts to dominate.

In this work, we are interested in low-energy collisions where capture is dominant. The low-collision-energy refinement of the Bohr-Lindhard model is the over-the barrier-model. This model introduces a quasi-molecular picture during the collision. To demonstrate this picture, consider a projectile ion A^{q+} approaching a neutral atom B . The potential energy barrier between the two centers decreases (Figure 2.1) as they come close to each other. According to the over-the-barrier model, when this barrier drops below the binding energy of the electron, at an internuclear distance $R = R_{mol}$, the electron can transfer from one nucleus to the other. This means that it can move in the joint potential energy well of the target and the projectile, thus becoming molecular. This quasi-molecular picture ends once the separation between the target and projectile increases again as the projectile moves away from the target, leaving the electron with some probability to be captured by the projectile ion. If the capture probability is unity at $R = R_{mol}$, as is nearly the case for

a highly charged projectile on a neutral target, then the cross section σ_c for capture is :

$$\sigma_c = \pi R_{mol}^2 \quad (2.1.8)$$

The absolute value of the binding energy I_B of the electron is given by:

$$I_B^*(R) = I_B + \frac{q}{R}. \quad (2.1.9)$$

This binding energy includes the increase due to the external Coulomb field of the approaching ion. A static approximation is assumed since $v_e \ll dR/dt$. Taking r to be the distance of the electron to the projectile center, the potential $V(r)$ experienced by the electron is:

$$V(r) = \frac{q}{|r|} + \frac{1}{|R-r|}. \quad (2.1.10)$$

To find the maximum $V = V_{max}$, we simply take the derivative of the above equation and set it equal to 0. Solving for V_{max} :

$$V_{max} = \frac{-(\sqrt{q} + 1^2)}{R}. \quad (2.1.11)$$

From 2.1.9 and 2.1.11 we obtain for R_{mol} :

$$R_{mol} = \frac{1 + 2\sqrt{q}}{I_B} \quad (2.1.12)$$

At infinite internuclear separation the binding energy I_A of the captured electron is given by:

$$I_A = I_B^*(R_{mol}) - \frac{1}{R_{mol}} = I_B + \frac{q-1}{R_{mol}}. \quad (2.1.13)$$

Here the shift induced by the target core is subtracted. Converting the binding energy I_A into a principal quantum number according to the hydrogenic approximation allows one to predict which states the electron will be captured into:

$$n = \frac{q}{\sqrt{2I_A}}. \quad (2.1.14)$$

For $Ar^{8+} + H$ collisions we expect that $R_{mol} = 1 + 2\sqrt{8}/0.5 \text{ a.u.} = 13.3 \text{ a.u.}$ and $I_A = 0.5 + 7/13.3 = 1.03$. Taking this I_A gives $n = 8/\sqrt{2 \times 1.03} = 5.57$. So we expect $n = 5$ and 6 levels of Ar^{7+} to be populated. It will be shown in Chapter 5 indeed this is the case.

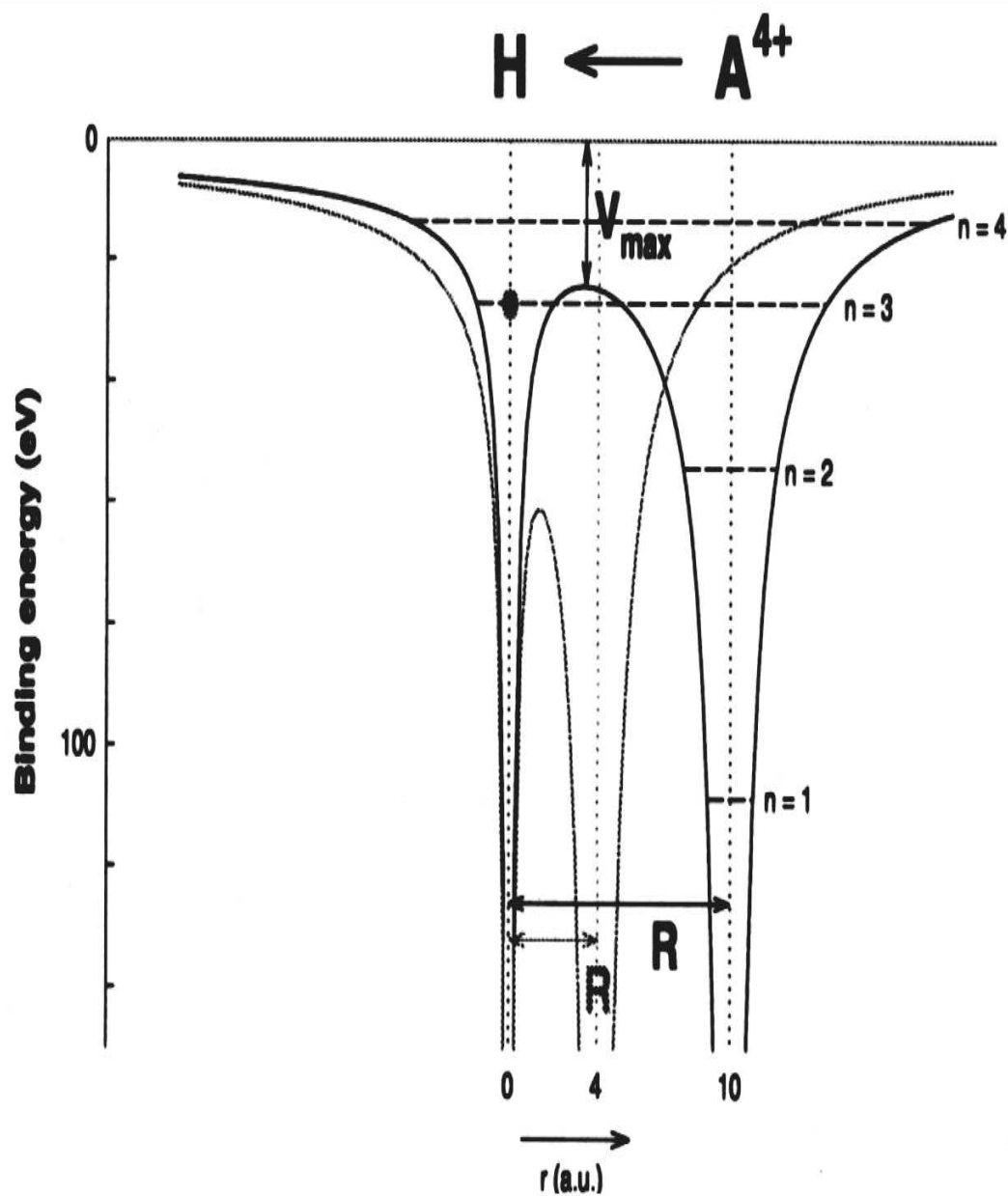


Figure 2.1: Schematic of over-the-barrier model for an ion with charge 4+ incident on H. As the two centers come closer it can be seen that the potential barrier between them decreases. (Taken from [21])

2.2 Quantum Mechanical Theory

In the previous discussion, we have treated the partners of the collision classically. In real life, the problem at hand requires solving the Schrödinger equation exactly. The time-dependent Schrödinger equation is:

$$H\psi(r, R, t) - i\frac{d\psi(r, R, t)}{dt} = 0, \quad (2.2.1)$$

where H is the full Hamiltonian including both target and nuclei potentials and kinetic energies and ψ is the electronic wave function. It is not easy to solve this equation exactly. The problem can be simplified with the Born-Oppenheimer approximation, whereby the nuclear motion is treated classically while the electronic motion is treated quantum mechanically. The Schrödinger equation then becomes:

$$H_{R(t)}\psi(r, t) - i\frac{d\psi(r, t)}{dt} = 0. \quad (2.2.2)$$

The aim here is to solve for $\psi(r)$ as a function of t . Notice that the wave function is implicitly a function of time, because H depends on R and R depends on time.

Several approaches to finding $\psi(r, t)$ have been reported in the literature. The group of Schultz et. al ([14]) solve Equation 2.2.2 in configuration space using a lattice expansion. This calculation requires a significant amount of computing time and the use of supercomputers, but can be carried out to infinite internuclear distances. Sidky and Lin [13] use a momentum-space grid and assume that the projectile motion is rectilinear with constant velocity v and impact parameter b . In this method, since the momentum space is finite, they do not require as much computing time, but are limited in the internuclear distance range over which they can carry out the calculation.

2.2.1 Close Coupling Theory For One Electron Systems

In the close-coupling description of the atomic collisions, it is assumed that the quantum mechanical states of the electron may vary within the limits of a given space configuration. This method is mainly good for describing dominant processes. Then the question of which states to populate takes on the form of which configurations may significantly be fed from an initial state in course of the collision to a specific final state.

Adopting a finite set of configurations which are orbitals of the target and/or the projectile system, the electron wave function at all times can be written as:

$$\Psi(r, t) = \sum_{k=1}^N a_k(t) \psi_k(r, t). \quad (2.2.3)$$

For a given trajectory with impact parameter b , collision velocity v , the occupation amplitudes $a_k(t)$ contain all the information about the collision. $\psi_k(r, t)$ are chosen so that they represent stationary states of the separated systems before and after the collision. At large negative t times, the amplitudes are zero for all f states, except for the initial state i for which $a_i(-\infty)$ can be set to 1. The transition probability for the electron to be found in states f is given by:

$$P_{i \rightarrow f}(v, b) = |a_f(+\infty)|^2 \quad (2.2.4)$$

and the partial cross section for this transition is:

$$\sum_{i \rightarrow f} = 2\pi \int_0^\infty b db P_{i \rightarrow f}(v, b). \quad (2.2.5)$$

The total cross-sections would be a sum of cross sections σ_f for a set of final states f . The capture experiments discussed in this thesis are state-selective. It is possible to determine relative partial cross sections for individual transitions with a coincidence experiment and compare them to Equation 2.2.5.

To construct the amplitudes $a_k(t)$, first consider the time-dependent Schrödinger equation within the space of basis configurations:

$$\langle \psi_j | i \frac{\partial}{\partial t} - H(R, r) | \Psi \rangle = 0 \quad j = 1 \dots N \quad (2.2.6)$$

where $H(R, r)$ is the electronic Hamiltonian:

$$H(R, r) = \frac{-1}{2} \nabla_r^2 + V_A(r_A) + V_B(r_B) \quad (2.2.7)$$

In Equation 2.2.7, r is the electron coordinate in the center of mass frame, and r_A and r_B are the same coordinate relative to atoms A and B . V_A and V_B are the potentials of the electron due to the interaction with A and B .

From Equation 2.2.6, a system of coupled equations follow for the amplitudes $a_k(t)$:

$$\sum_{k=1}^N N_{jk}(t) \frac{da_k(t)}{dt} = i \sum_{k=1}^N M_{jk}(t) a_k(t), \quad j = 1 \dots N \quad (2.2.8)$$

with the time-dependent overlap matrix elements:

$$N_{jk} = \langle \psi_j | \psi_k \rangle \quad (2.2.9)$$

and coupling matrix elements,

$$M_{jk} = \langle \psi_j | i \frac{\partial}{\partial t} - H(R, r) | \psi_k \rangle . \quad (2.2.10)$$

In the close-coupling method, efficient ways to compute the matrix elements is of importance. More detail on the close-coupling method and the choice of basis sets can be found in for example [23].

One possible choice is to expand the electronic wave function in terms of target and projectile states. This is called the atomic basis expansion:

$$\psi = \sum_i a_i(t) \phi_{T_i}(r) e^{i\vec{v}/2 \cdot \vec{r}} + \sum_j b_j(t) \phi_{P_j}(r) e^{-i\vec{v}/2 \cdot \vec{r}} \quad (2.2.11)$$

where \vec{v} is $\dot{\vec{R}}$ with the corresponding time-independent Schrödinger equations: $H_T\phi_{T_i} = E_{T_i}\phi_{T_i}(r)$ and $H_P\phi_{P_j} = E_{P_j}\phi_{P_j}(r)$. The subscripts T and P stand for the target and the projectile. This is a good choice for capture, but it does not work as well for ionization because it requires that one discretize the continuum levels. We have compared our capture results in Chapter 6 with calculations carried out by Lee and Lin [9] using this expansion.

Chapter 3

Review of Low-Intermediate Energy Ionization Theory

The atomic basis introduced in the previous section does not work as well for ionization as it does for capture. Low-energy ionization has been more heavily studied in terms of molecular basis set expansion. This basis set is defined by solving the time-independent Schrödinger equation for $\psi(r, R)$ for each R .

3.1 The Collision Problem in Molecular Orbital Expansions

Consider Figure 3.1, where A and B are the two nuclei, sharing an electron. In Figure 3.1 subscripts, T and P stand for the target and the projectile. In the center-of-mass frame, the Schrödinger equation for the electron is:

$$(H_e - i\frac{\partial}{\partial t})\psi(r, t) = 0 \quad (3.1.1)$$

with the electronic Hamiltonian:

$$H_e = \frac{-1}{2}\nabla_r^2 - \frac{Z_A}{|r_P|} - \frac{Z_B}{|r_T|} \quad (3.1.2)$$

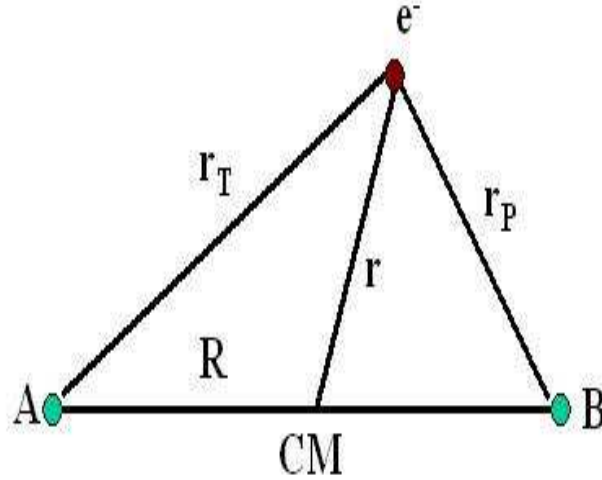


Figure 3.1: Coordinate system used to describe the collision.

In the molecular expansion R is taken as a parameter, and the wave function is written as:

$$\psi(r, t) = \sum a_n(t) \psi_n(R, r) \exp(-i \int^t E_n(R) dt') \quad (3.1.3)$$

The states ψ_n are solutions of the time-independent Schrödinger equation:

$$H_e \psi_n(R, r) = E_n(R) \psi_n(R, r) \quad (3.1.4)$$

Figure 3.2 shows $E_n(R)$ for H_2^+ for σ and π states. After substitution of 3.1.4, into 3.1.1, a set of coupled equations are obtained:

$$\begin{aligned} \dot{a}_m &= -\sum a_n \left[\langle \psi_m | \dot{R} \frac{\partial}{\partial R} | \psi_n \rangle \exp(i \int^t (E_m - E_n) dt') \right. \\ &\quad \left. - \langle \psi_m | \dot{\theta} \frac{\partial}{\partial \theta} | \psi_n \rangle \exp(i \int^t (E_m - E_n) dt') \right]. \end{aligned} \quad (3.1.5)$$

The term $\dot{R} \langle \psi_m | \frac{\partial}{\partial R} | \psi_n \rangle$ is called the radial coupling term. It couples molecular states that have the same angular momentum projection on the internuclear axis. This angular momentum is conventionally represented by the quantum number m . The radial coupling term, couples molecular states for which $\Delta m = 0$, for example σ states to σ states or π states to π states.

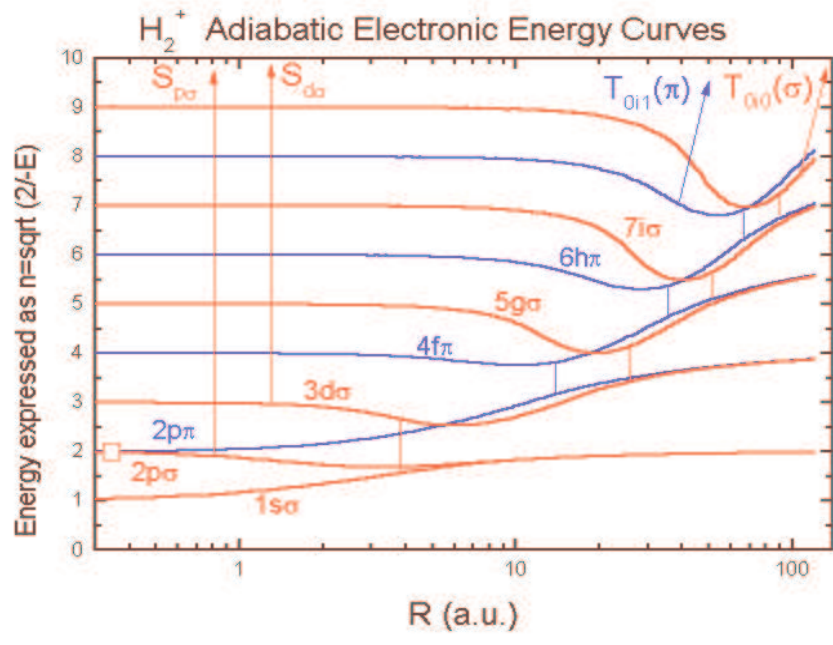


Figure 3.2: Electronic energy curves for H^{2+} .(Adapted from [22].)

With the help of Figure 3.2 one can identify several radial promotions widely discussed in literature. The mechanisms for ionization are labelled ‘S’ and ‘T’ processes. These labels come from hidden crossing theory [24]. The term ‘hidden’ refers to the fact that these crossings take place at complex values of the internuclear axis. There are several types of hidden crossings. The S-type crossings are associated with transition from a quasi-molecular system to a united atom region, meaning when the two nuclei are approaching each other. The ‘S’ process describes superpromotion of energy levels where the promotion is direct from the $2p\sigma$ and $3d\sigma$ levels. The ‘T’ process describes promotion of electrons through a ‘saddle-point’ mechanism. The saddle is defined as the top of the barrier when the pulls the electron feels from the centers are equal in size and opposite in direction, thus resulting in a zero force on the electron. When the two-nuclei start to separate, an electron that was stranded on the saddle gets promoted to the continuum through Rydberg levels and at some point the system ionizes.

The other term in Equation 3.1.5 can be written as $v_p b/r^2 \langle \psi_m | iL_y | \psi_n \rangle$ and is called the rotational coupling term. Here v_p is the projectile velocity, b is the impact parameter and $L_y = -i\partial/\partial\theta$ is the angular momentum perpendicular to the collision plane. The rotational coupling term couples states with $\Delta m = \pm 1$, for example σ states to π states or π states to δ . An electron can be promoted from σ to π by this coupling, when the two nuclei come close to each other. As can be seen from Figure ??, for the π -track T_{001} promotion mentioned above to take place first the electron has to go from the $2p\sigma$ state to the $2p\pi$ state through rotational coupling. This promotion is expected to be the dominant, but not only, T-ionization process.

Each of the above mechanisms is expected to produce a characteristic velocity space

distribution of the promoted electron. Several experiments have been done to look for electron velocity distributions in the low-energy regime. The findings of these experiments support the above promotion schemes. Dörner *et al.* ([15]) studied electron ejection in the proton-helium system for low impact energies. They found that ejected electrons lie mainly in the scattering plane. Their longitudinal velocities were found to lie between those of the target and the projectile as would be expected for a ‘saddle-point’ promotion. The velocity distributions in the scattering plane showed a two-finger structure, one finger extending away from the direction of the recoil ion and one toward it. This distribution can be thought of a signature of the quasi-molecular state through which the electron was promoted. For the case of protons colliding with He this was the $2p\pi$ state and the characteristic nodal line of this state is seen as an experimental minimum. Another finding of [15] was that the relative intensity of the fingers were found to oscillate with changing energy. The origin of this oscillation is attributed to the interference between σ and π amplitudes in the continuum, with a relative phase which varies with changing projectile velocity.

After Dörner *et al.*’s experiment several other experiments by other groups were carried out, including one by our group discussed in Chapter 6. The above explanations were found to hold for those velocity distributions as well. One such experiment was done by Abdallah *et al.* ([16]). Their findings are shown in Figure 3.3, where ejected electron velocity distributions are given for different choices of transverse momenta. Once again a nodal line, signature of a π structure, is observed.

One main problem in studying ionization at these energies is that most calculations done to reproduce the above results were done on the simplest system, i.e. proton impact

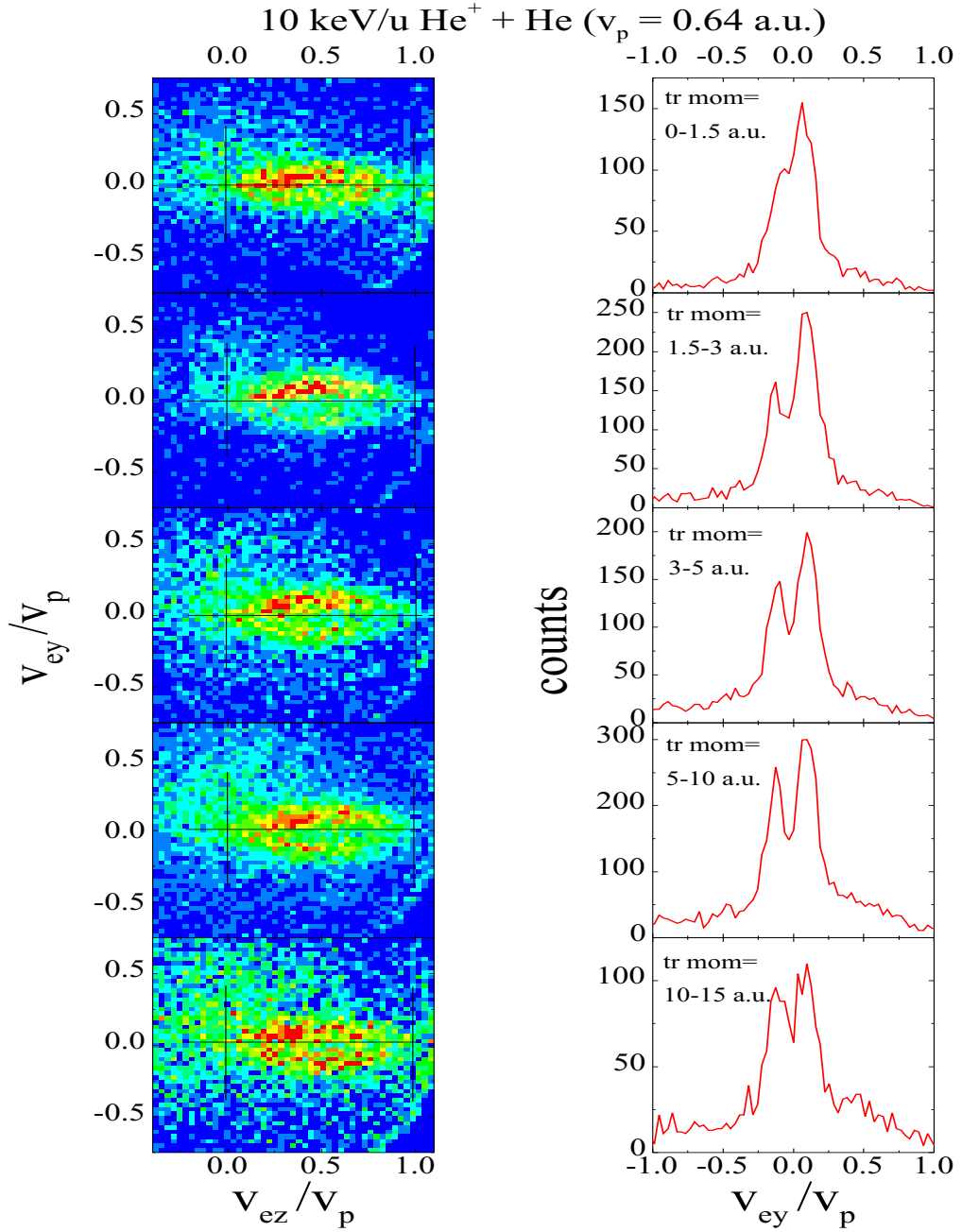


Figure 3.3: Ejected electron momenta for a 10 keV He^+ beam on He . The left hand side of this figure show ejected electron velocity distributions scaled to the impact velocity. The right hand side shows projections of these distributions onto the transverse axis.

on atomic hydrogen. It was found that the calculations are sensitive to the exact system ([16]). The qualitative results of different theoretical models do not quite match ([12, 13]). This results in the need for a true three-body experiment, namely one involving protons on atomic hydrogen.

Chapter 4

COLTRIMS Technique

The momentum imaging method used in all the experiments studied in this thesis is referred to as the COLTRIMS (COLd Target Recoil Ion Momentum Spectroscopy) technique ([15, 5]). With this method one can reconstruct the recoil ions' full momentum vectors at the time of their birth, by measuring their positions on the detector and their times-of-flight. This way, the scattering plane, the impact parameter, and the Q value of the collision can be determined event by event.

4.1 Experimental Setup

All of the experiments were conducted at the KSU-CRYEBIS facility [25]. A description of such an ion source can be found in [26]. The beamline is shown in Figure 4.1. The ion beam left the EBIS and passed the switching magnet and a focusing lens before it came to 4-jaw slits right before the chamber. The base pressure in the chamber was about 1×10^{-8} torr with the target gas off and increased to about 1×10^{-7} torr with it on. The schematic of the target setup is shown in Figure 4.3. The target gas intersected the ion beam at right angles. For the ionization experiments involving a helium target recoil ions

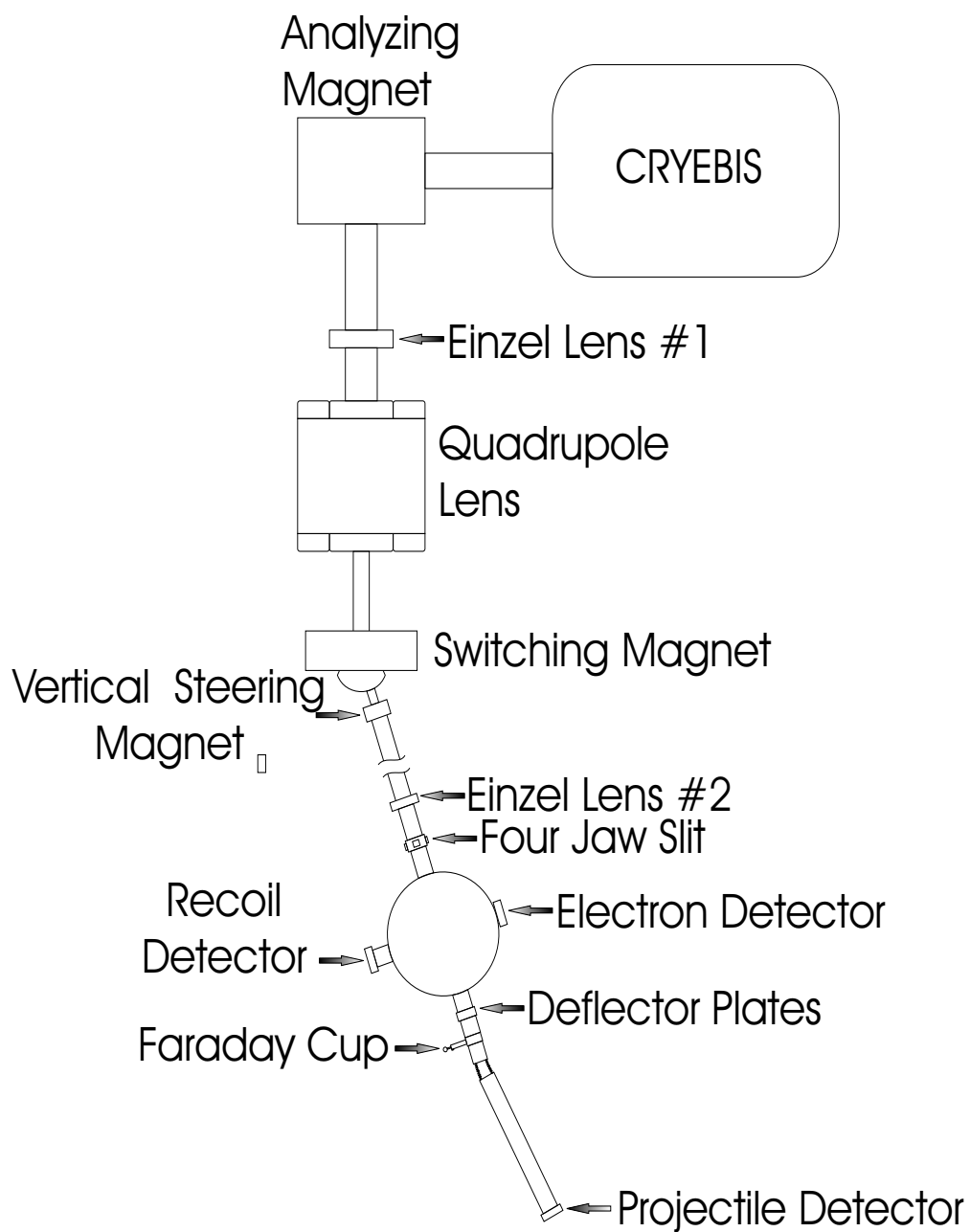


Figure 4.1: A schematic of the beamline.

and electrons were directed by an external electric field between 25 and 100 V/cm towards position sensitive channel plate detectors (PCSD). For the atomic and molecular hydrogen target experiments this field was 10 V/cm.

The coordinate system for our experiments is defined in Figure 4.2. The ‘longitudinal’ direction is taken parallel to the beam, or z direction and the ‘transverse’ direction is perpendicular to the beam, in the $x - y$ plane. The gas jet is in the y direction and the electric field is in the x direction.

For the ionization experiments the electrons and the recoil ions, and for the capture experiments the projectile ions and the recoil ions, were detected in coincidence. The electrons were detected after travelling through a short acceleration distance of 23 mm. A small negative bias voltage of -5 to -10 V was applied to the first channel plate of this detector to repel background electrons. The recoils were accelerated in the opposite direction over a distance of 86 mm and subsequently traversed a field free region of 305 mm. The extraction field was shaped slightly so as to focus a parallel beam from the interaction region onto the recoil detector and was arranged also to provide first-order time-focusing for the recoil ions. The times-of-flight of the electrons was only a few nanoseconds whereas it was a few microseconds for the recoil ions. The projectiles travelled a distance of 225 cm to arrive at the projectile 2D PSD. The projectiles passed a pair of electrostatic deflection plates on the way for charge separation. The spread in the time-of-flight of electrons was about 1 ns, which made measuring the third component of the electron velocity impossible. Instead, the time signal of the electrons was used to give the start signal for a time-to-amplitude converter, which was stopped by the recoil-ion signal. This allowed us to measure the time-of-flight of the recoil ions and thus the third component of their momentum.

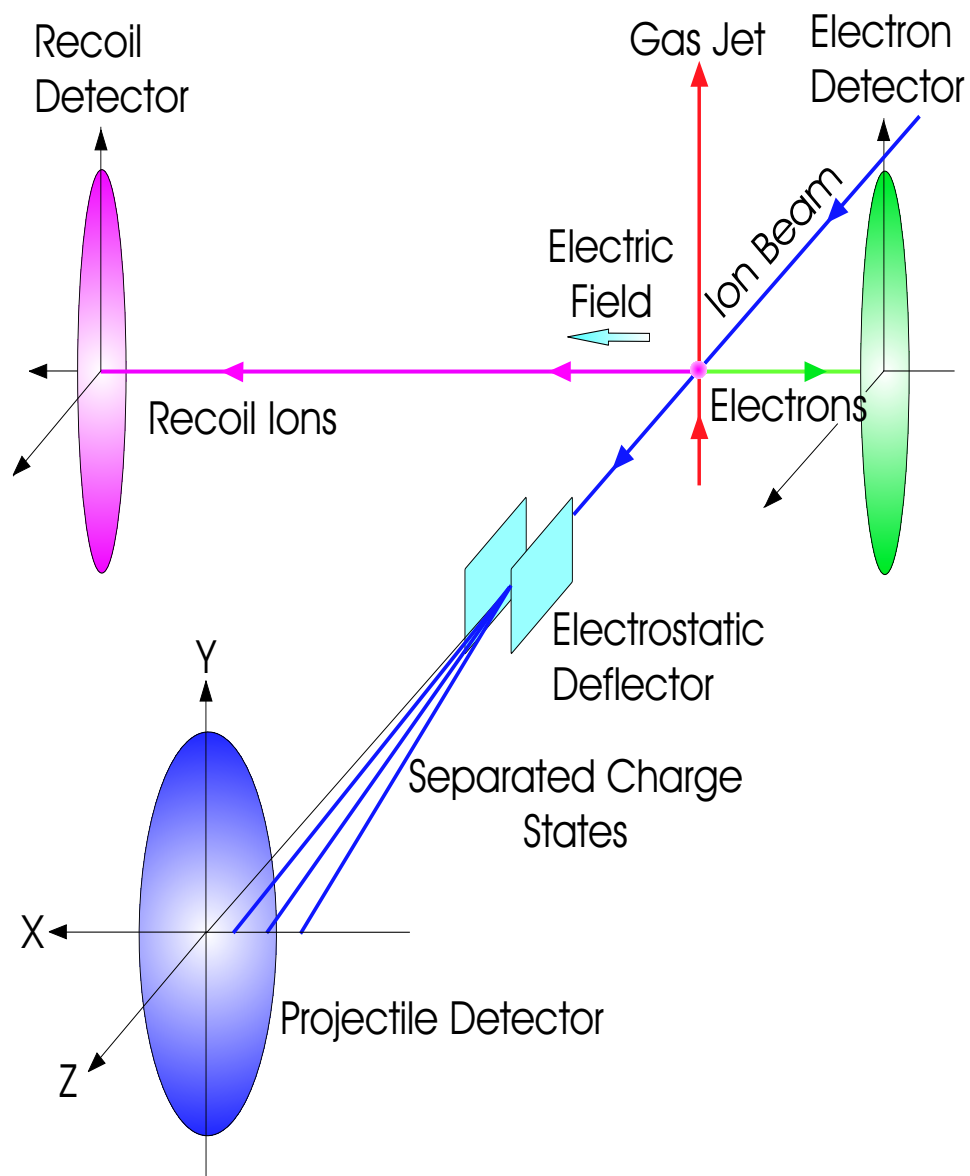


Figure 4.2: Coordinate system and the setup of the detectors.

From the position and the time-of-flight, we derived the longitudinal and the transverse components of the final state momentum of both electrons and recoiling ions, using the following equation. For p_z and p_y for both electrons and recoils, we have used:

$$p_z = m \frac{\Delta z}{\Delta t} \text{const} \quad (4.1.1)$$

and

$$p_y = m \frac{\Delta y}{\Delta t} \text{const}. \quad (4.1.2)$$

The *const* is a proportionality constant between position and momentum and can be calculated using the known dimensions and the electric field in the spectrometer. (The spectrometer used in this thesis is identical to the one used in [27]). The momentum along the x direction for recoils was calculated using the first-order approximation:

$$p_x = p_0 + qE\Delta t. \quad (4.1.3)$$

The software SIMION [28] was used to simulate the spectrometer and calculate qE . p_0 is the initial momentum along x and is approximated to be zero. Δt in formulae 4.1.1, 4.1.2 and 4.1.3 is the time-of-flight of the recoil ions. This time-of-flight was obtained from the TAC spectra.

4.2 Atomic Hydrogen Target

As mentioned in the previous chapter all theoretical work that attempted to explain the features seen in experiments in the low-energy regime solve the Schrödinger equation either for a one electron target or for a single electron interacting with the remaining ion via an effective potential. Yet experiments that exist to date have not been done with this system.

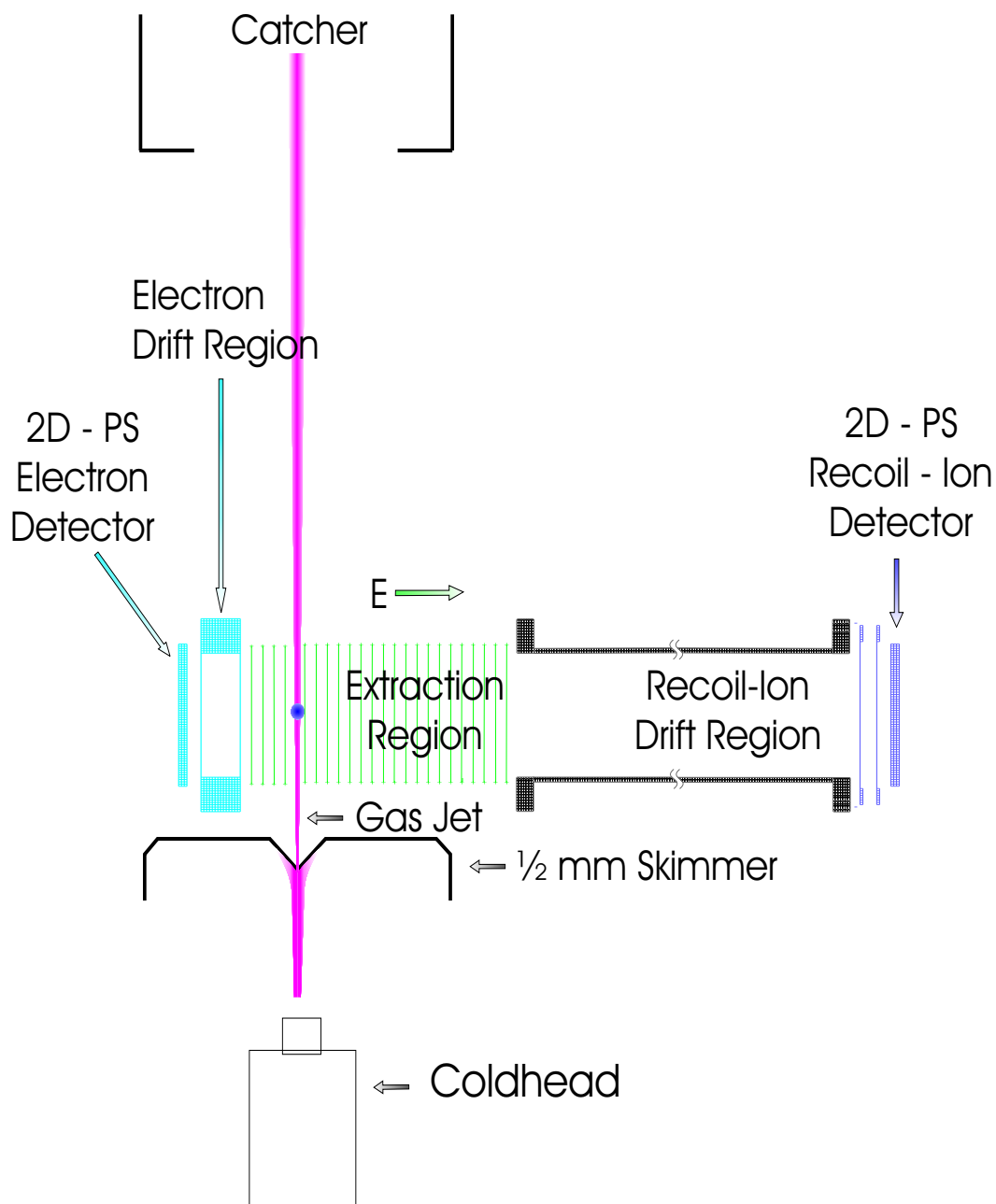


Figure 4.3: A schematic of the target setup (not to scale) showing the collision region.

The main reason for this is the difficulty of obtaining a cold atomic hydrogen target needed for the momentum imaging experiments. The theoretical models available, [13, 12, 14], are able to explain a somewhat qualitative picture for other systems, yet fail to agree among themselves. We have focused our work on trying to provide an atomic hydrogen target in the hopes of getting results directly comparable to theoretical models.

Initially a Slevin-type of atomic hydrogen source that was already in-house was used. Unfortunately we were never able to carry out our experiments with this source for the reasons stated below. We discarded this source in favor of an Evenson cavity microwave source which proved to be easier to manipulate and operate. Details on these sources are given in this chapter.

4.2.1 Slevin-Type Atomic Hydrogen Source

A description of this source is given by Slevin and Sterling [29]. Figure 4.4 shows a schematic of this source. The discharge tube is made of pyrex and has an inner diameter of 18 mm and a length of 240 mm. The helix coil is wrapped around the tube 12 turns and is enclosed by a copper shield. Discharge power was delivered via an RF generator oscillating at approximately 35 – 36 MHz with 10 – 12 watts of forward power. We were able to achieve standing wave ratios (SWR) of about 2 – 3. Smaller SWR's correspond to less reflected power back to the generator, thus more absorbed by the gas. We mounted the source on a three dimensional mechanical manipulator which allowed us to align the source so it collided with the ion beam at right angles and also to change the distance of the nozzle to the skimmer.

Our initial goal was to use atomic hydrogen in our ionization experiments, which meant

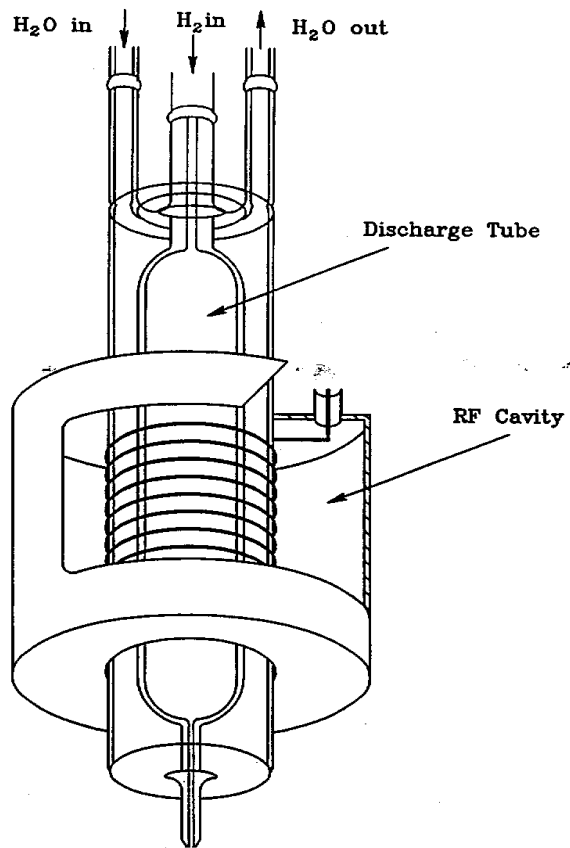


Figure 4.4: Schematic of Slevin-type atomic hydrogen source

we had to detect electrons. The first problem with this source arose from the fact that light emitted from the source made its way into the chamber, producing a substantial number of electrons generated by light hitting the spectrometer wires. We were able to reduce this problem somewhat by building a 'deviator' out of teflon that was attached to the tip of the nozzle. Even though the light problem was solved we had another type of noise that we could not eliminate: electronic noise due to the RF source. At the end we were never able to detect H coming from the source and after considerable time decided to not use it.

4.2.2 Evenson Cavity Microwave Discharge Atomic Hydrogen Source

This source uses microwave radiation at 2450 MHz to dissociate the hydrogen gas similar to one used by Paolini et. al. [3]. The effectiveness of such a source depends strongly on the ability to couple the gas as a reactive load into the microwave circuitry. Figure 4.5 shows the arrangement of our hydrogen source. A quartz tube with an outer diameter of 9 mm and 1 mm thickness was used for the main body of the discharge tube. The ends of the tube are made of 1/4" quartz. The exit has a constriction of 1 mm to keep a certain pressure inside the discharge region. We used research grade H_2 gas as input and did not see much of a difference when we switched to ultra high purity gas. The molecules left the gas bottle, passed a 1/4" copper tubing and arrived at a filter that had a 30 micron grid which was connected to a needle gas valve. The glass tube exit was connected to a 6" flange by a Cajon fitting.

Preparation Of The Source

Cleaning was quite important. The discharge tube, the teflon tube and the nozzle were soaked overnight in ortho-phosphoric acid then washed with water. Afterwards they were soaked in acid once again and let dry in a 100°C oven for 2 – 3 hours. Initially we did not apply this last coating of acid, but later found that it helped the discharge. Dust is found to be a major contributor to recombination, so great care was taken in mounting the source on to the manipulator system after cleaning. Foil was wrapped on the ends of the tube until the last installment stage to make sure no dust entered inside it.

During venting and pumping down procedures, care was taken to assure that the dis-

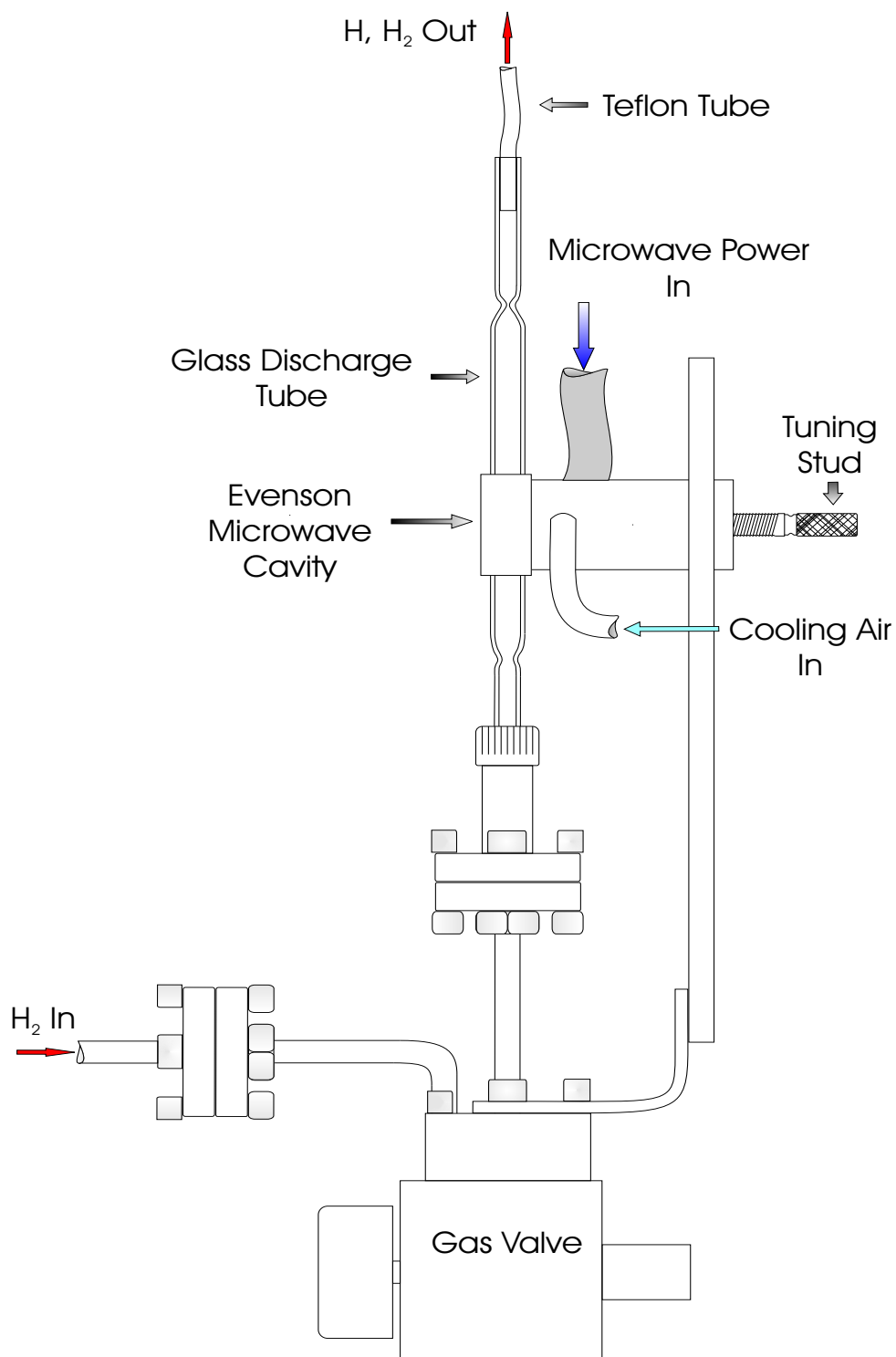


Figure 4.5: Arrangement of the atomic hydrogen source setup (not to scale) .

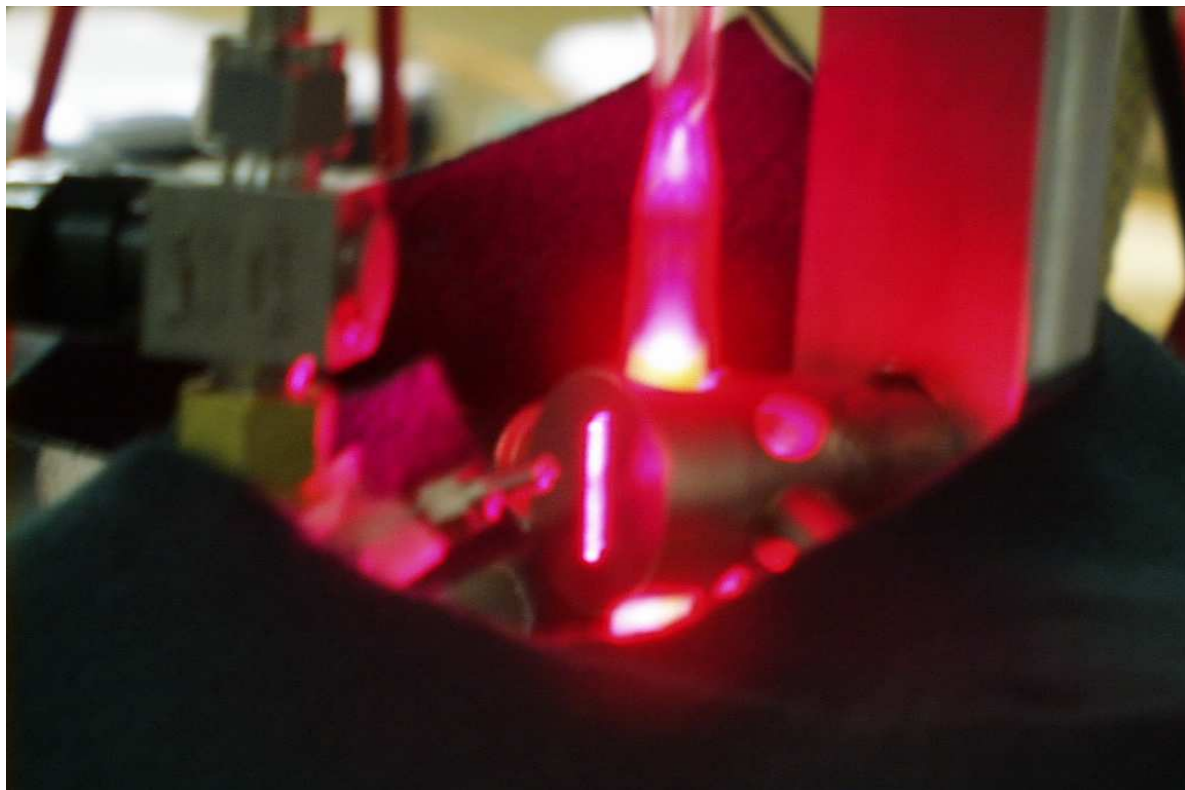


Figure 4.6: Atomic hydrogen source.

charge tube remained at a higher pressure than the rest of the chamber, to avoid any gas flowing back into the source and contaminating it.

Tuning Of The Source

The resonant frequency of the cavity was adjusted by means of the tuning stub and the coupling by means of an adjustable ceramic coupling slider (not pictured). In tuning the cavity with the discharge in operation, the tuning stub was adjusted for minimum reflected power, with minimum probe penetration. Next, the probe was adjusted. Since these two operations are not independent, successive readjustment improves the efficiency. With a 13 mm discharge tube, optimum tuning was obtained with the end tuning stub approximately 5 mm from the discharge tube. The operating pressure was between 6 and 8×10^{-7} torr in the nozzle region and about 800 mTorr in the discharge tube. The forward power was 45 – 50 Watts with a corresponding reflected power of 1 – 4 Watts.

The H atoms were transferred from the discharge region via Teflon spaghetti tubing 3 mm in diameter and 22 cm in length . Teflon has a very small recombination coefficient for H . Ground state H cannot recombine in a background of H_2 . The Teflon tubing was connected to the exit by a wrapping of Teflon tape. Since this connection was inside the vacuum chamber it was an acceptable one. Another advantage of using flexible tubing was that we could bend it easily to prevent light from the source from entering the chamber and producing background electrons. The Teflon tubing finally was connected to a thin capillary needle of 0.5 mm diameter. Figure 4.6 is a picture of the source while it is operating.

Alignment Of The Source

The alignment of the source was achieved by means of a two dimensional ($x-z$) manipulator that was connected to the exit teflon tubing (see Figure 4.7). High pressure of hydrogen was allowed into the chamber to collide with an ion beam while the position spectrum of the recoil detector was observed to see the ‘jet’ move as the manipulator settings were changed. Figure 4.7 shows a picture of our built-in-house manipulator attached to the hydrogen source. There was no y motion control. The nozzle was fixed at 10 mm from the skimmer. Figure 4.8 shows an example of what the position spectrum on the recoil detector looked like when alignment was achieved. This position spectrum was obtained from ionization of atomic hydrogen by 25 keV proton impact. The jet is clearly visible with the background hot gas due to H_2 in the chamber. The two vertical lines seen in the jet are identified to be on the left from the ionization and on the right from capture. The pink box in this figure is a gate that shows how one can choose the events to narrow them down to those that correspond to the collisions with the jet, but notice that this gate still has background gas in it. In actual analysis further gating is needed and how this is done is described in the following chapters.

Target Density

To calculate what the jet target thickness was obtained we had to go backwards, i.e. first find what the coincidence rate was through the experiment then calculate the target thickness. The coincidence rate is given by:

$$\gamma = N_B \sigma n l \epsilon_1 \epsilon_2. \quad (4.2.1)$$

We used the ionization experiment for 50 keV protons colliding with H to calculate

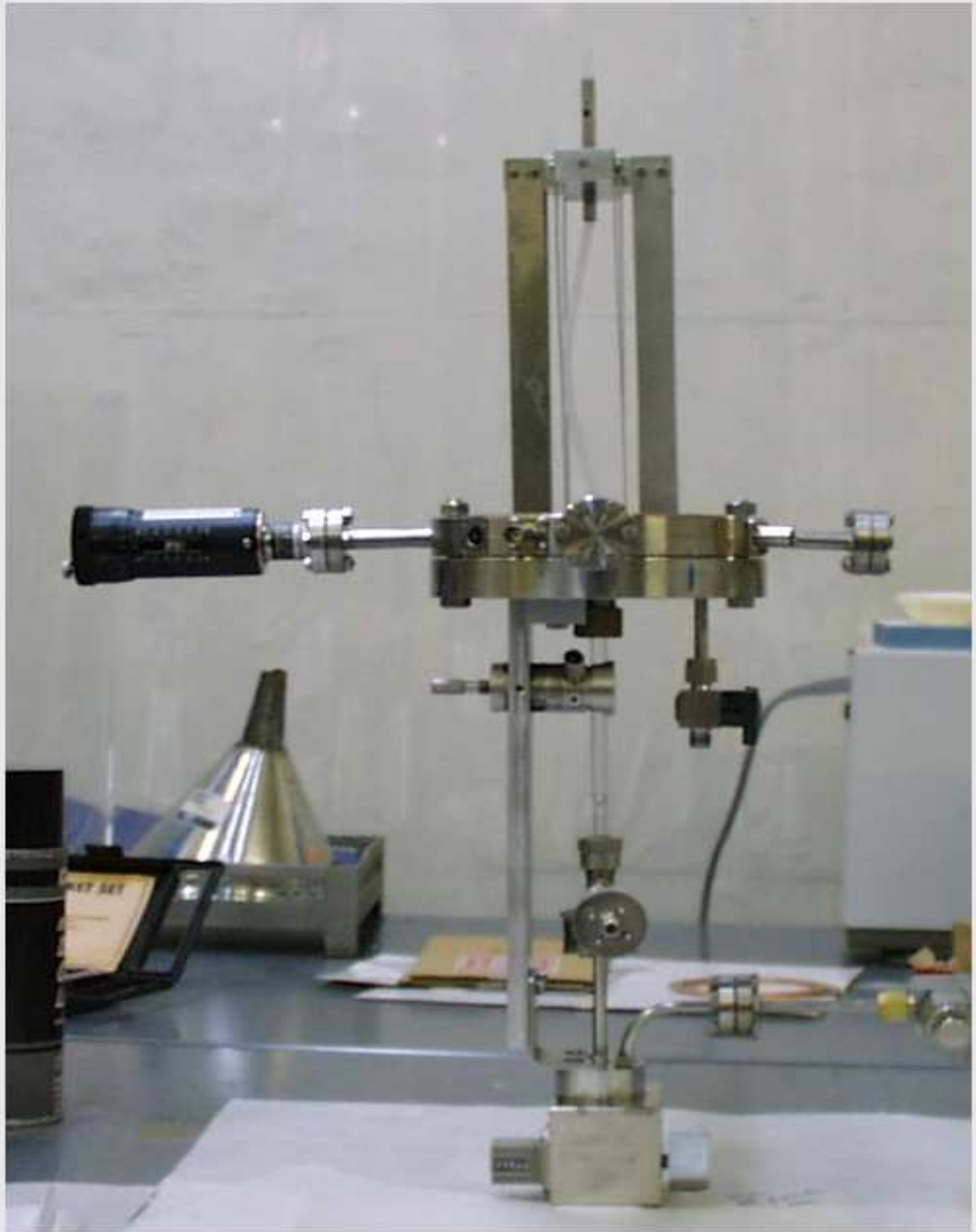


Figure 4.7: The x-z manipulator for the atomic hydrogen source.

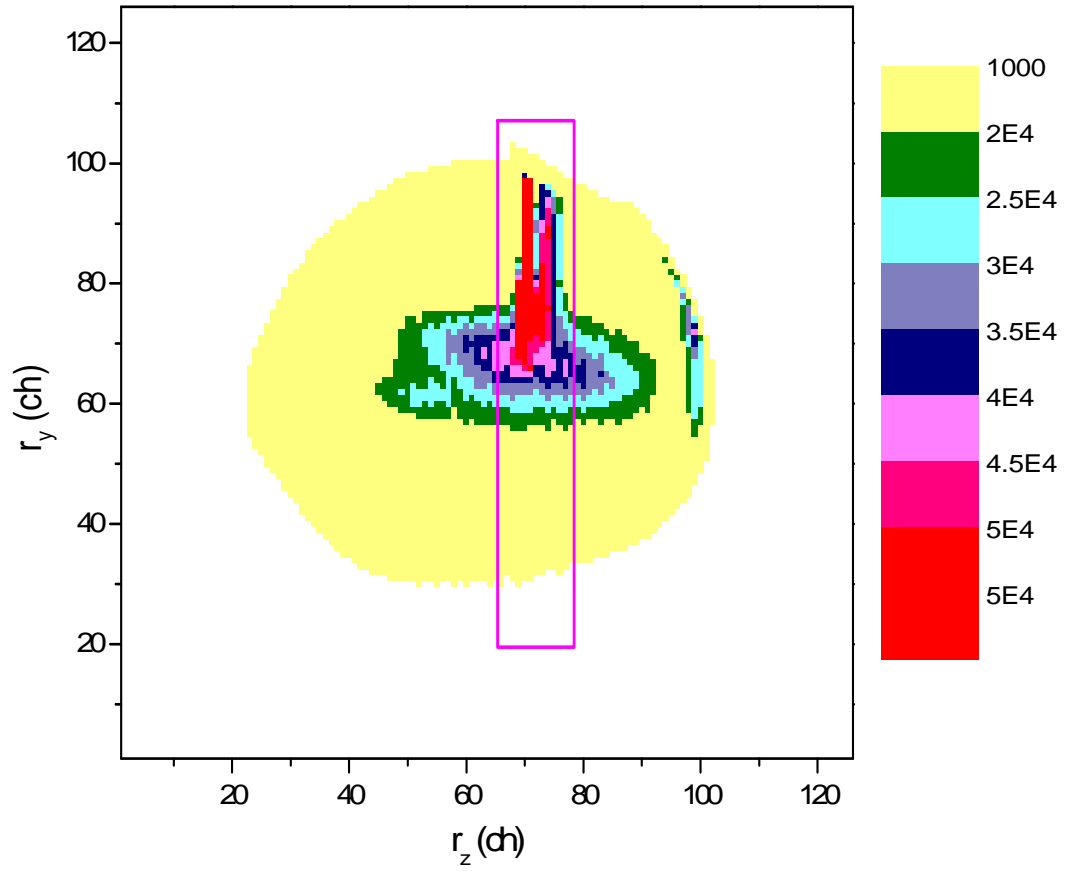


Figure 4.8: The gas ‘jet’ observed on the recoil ion detector for ionization of atomic hydrogen for 25 keV proton impact. the conversion from channels to atomic units of momentum is such that 8.5 channels correspond to one atomic unit for H^+ .

the target thickness. The electron-recoil ion coincidence rate (γ) was 10 /s for $e - H$ coincidences. N_B is ion beam current in particles per second. The beam current was 500 pA which corresponded to an N_B of 0.3×10^{10} /s. The corresponding cross-section (σ) for this process is 1.25×10^{-16} cm² ([?]). ϵ_1 and ϵ_2 are the detector efficiencies for both electron and recoil detectors. They are both taken to be 0.2. Inserting these values into Equation 4.2.1, we find that the target thickness (nl) is 6.67×10^8 /cm².

Dissociation Fraction

Figure 4.9 shows the TAC spectrum obtained for ionization for a 25 keV/q H^+ incident on our target gas of H and H_2 mixture (the TAC is gated on the total jet seen in Figure 4.8). Since the cross-sections for these reactions are similar, this spectrum is a good indication of the dissociation rate at the collision region. The dissociation fraction obtained in the jet region varied between 0.3 and 0.4 due to fluctuations in the gas pressure. This is a lower limit on the dissociation fraction since the gate in Figure 4.8 still includes considerable background H_2 gas. Due to impurities in the gas once the source was turned on it fluctuated before it reached the right characteristic red color. After 2-3 hours of operation the source turned a pale white color for about 10 minutes. During this operation mode a reduction of H content in the jet was observed. We observed this type of color change every 8-10 hours of operation. Except for these fluctuations, our source continued to produce H atoms continuously for 2 months on one discharge tube. After 2 months the source started to not perform as well and was ready for another cleaning process.

Figure 4.10 shows the wavelength spectrum of the hydrogen source at the discharge region. As can be seen from this figure we had strong population of atomic hydrogen in

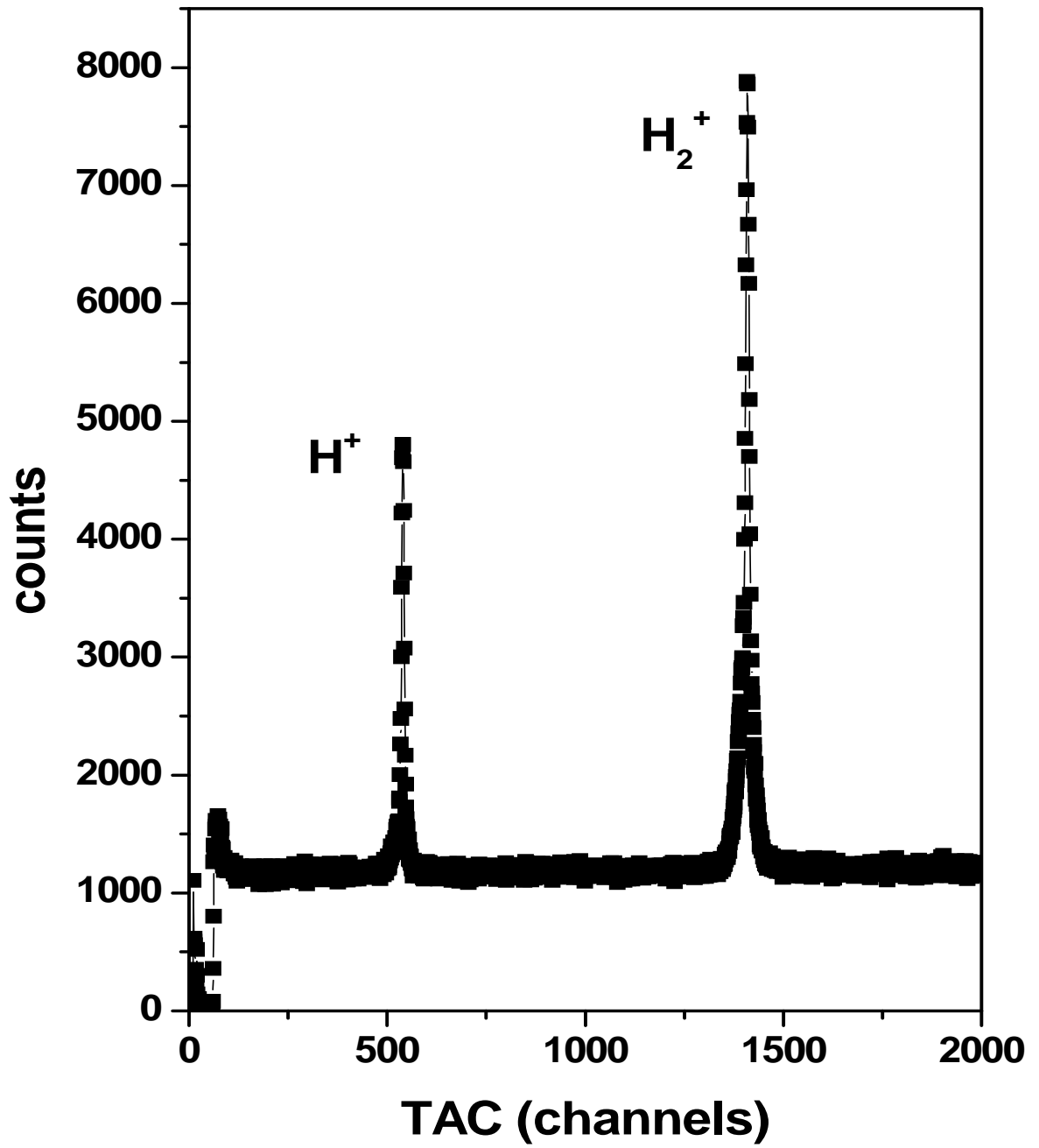


Figure 4.9: Sample TAC spectrum for $H^+ + H, H_2$ ionization at $25keV$ gated on the gas jet.

the discharge region. However, because of the long distance the H atoms have to travel before reaching the collision region, some recombination was inevitable.

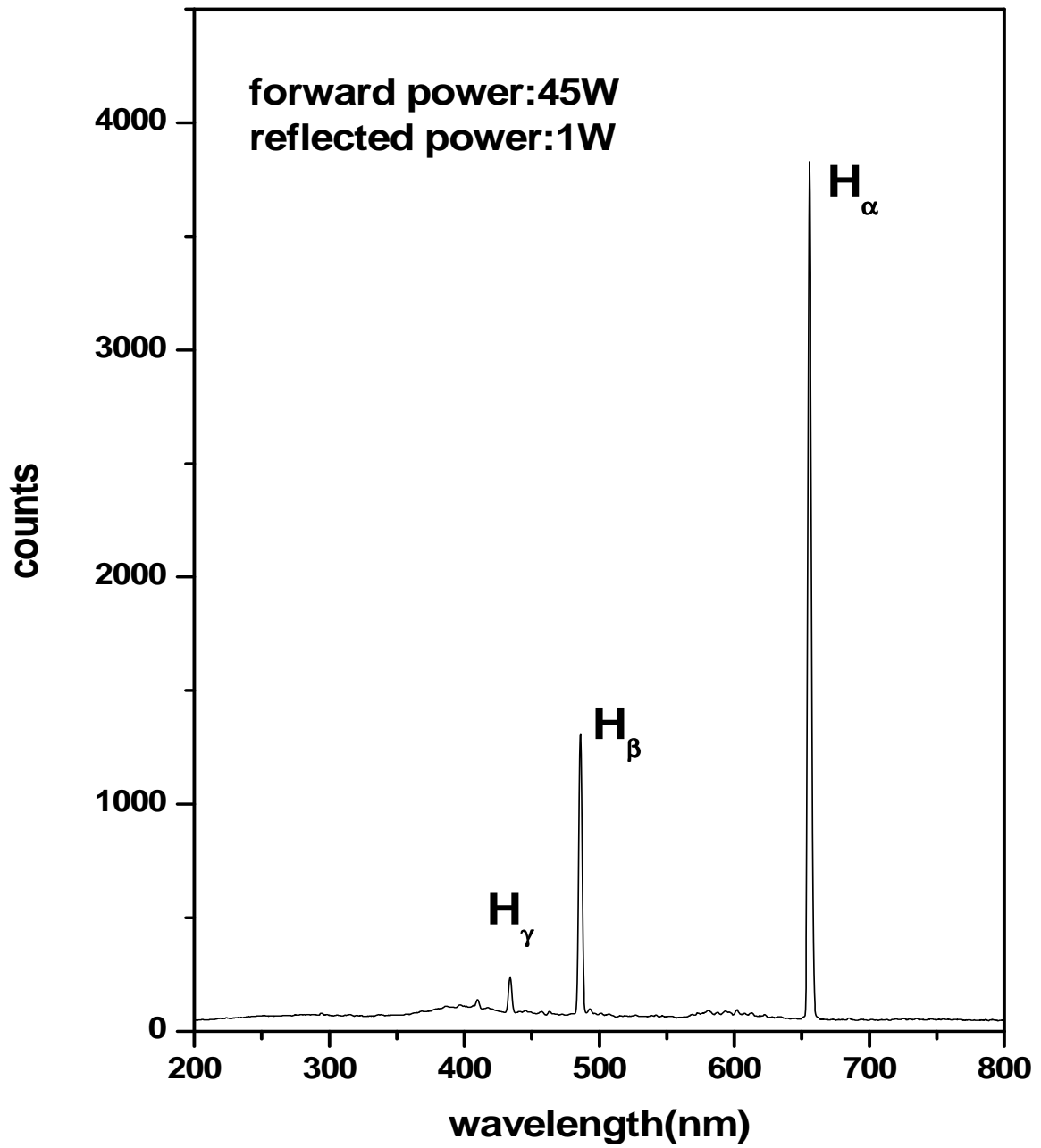


Figure 4.10: Sample wavelength spectrum in the discharge region.

Momentum Resolution and The Velocity Profile Of The Source

The H particles leave the 1 mm nozzle of the hydrogen source and travel 10 mm before they enter the chamber via the 0.5 mm skimmer. They then travel 50 mm before they cross the ion beam as sketched in Figure 4.11. In a H gas at room temperature, the momentum of the gas is given by:

$$p_0 = \sqrt{2mE} = 2a.u., \quad (4.2.2)$$

where $E = (3/2)kT$. From Equation 4.2.2 and from the distances given in Figure 4.11 we find the momentum resolution along z to be 0.1 a.u. In our experiments the momentum resolution for the recoil ions along the beam was measured to be less than 0.2 a.u. Along the x direction we expect a momentum resolution of about 0.05 a.u. from geometry of the setup. This is less than the resolution along y due to the collimation of the beam along the x direction. In the experiments, the upper limit for this resolution was measured to be 0.45 a.u.

The target is ‘hot’ along the jet direction. It effectively gets cooled somewhat by passing through the skimmer. We can calculate how much cooling happens and what resolution to expect in the jet direction. The velocity of a gas can be described using a Maxwell-Boltzmann distribution. This distribution is given by:

$$F(\vec{v}) = \left(\frac{m}{2\pi kT}\right)^{3/2} e^{-mv^2/2kT}. \quad (4.2.3)$$

From 4.2.3, the expected distribution along the jet can be found from:

$$\frac{dN}{dv_y} = Av_y^3 e^{-\beta v_y^2}, \quad (4.2.4)$$

where A is a normalization constant and $\beta = m/2kT$. A graph of what this distribution looks like in momentum ($p = mv$) is given in Figure 4.12.

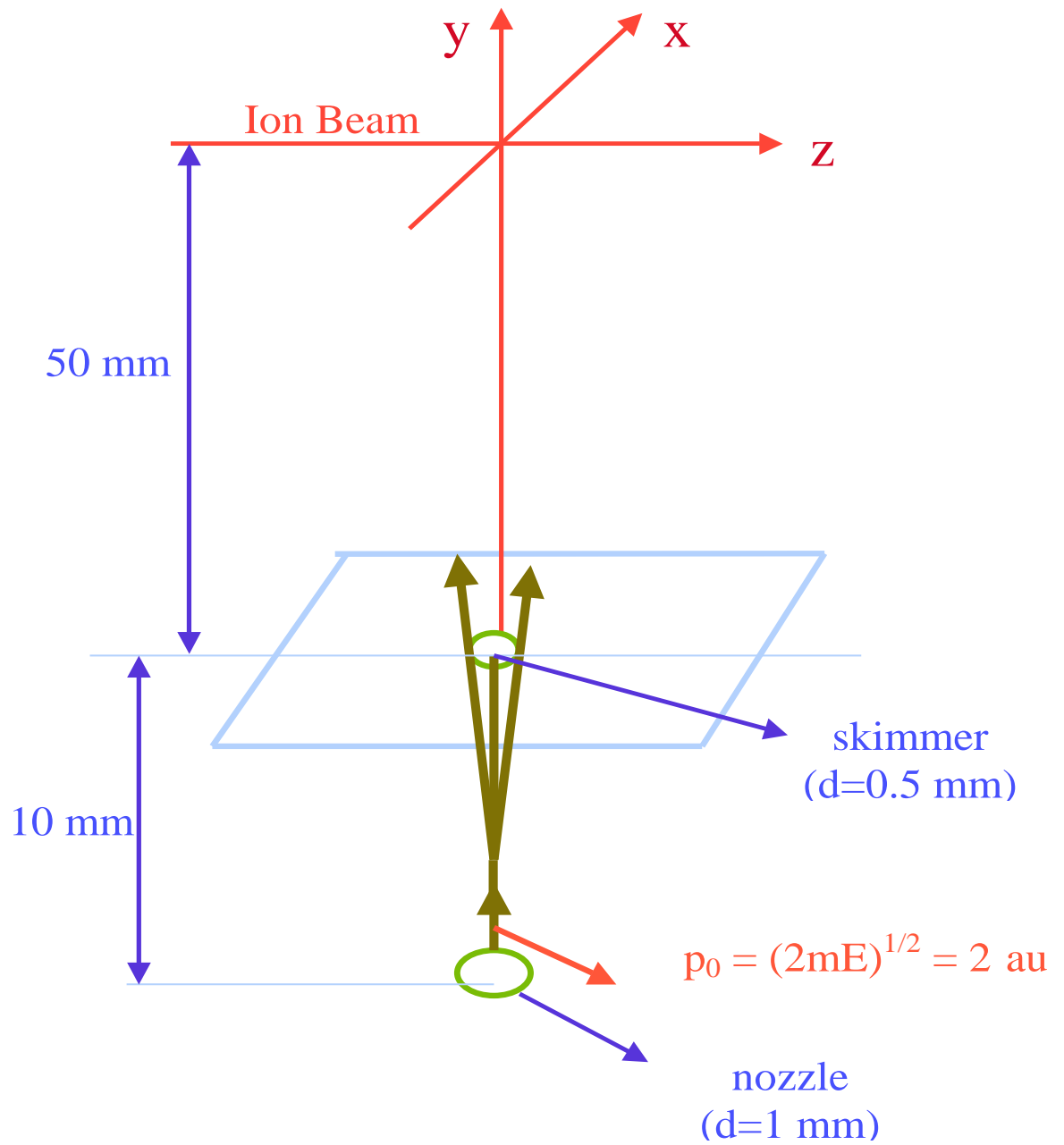


Figure 4.11: A sketch of the nozzle-skimmer-beam crossing setup. The nozzle is 1 mm in diameter and the skimmer is 0.5 mm in diameter. The beam crosses the jet 50 mm upstream.

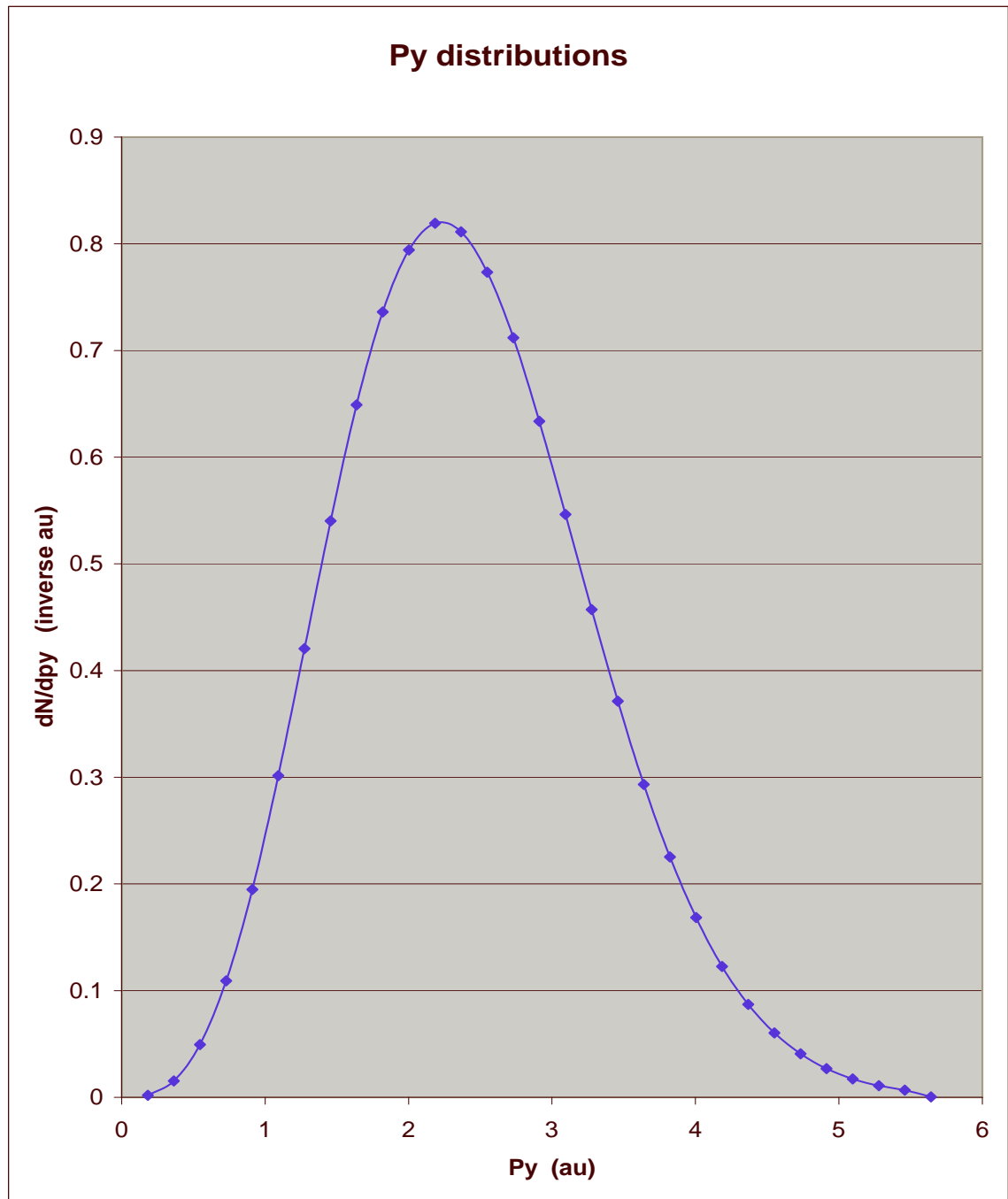


Figure 4.12: Expected momentum distribution of the target gas along the y direction.

It can be observed from Figure 4.12 that a momentum shift of about 2.2 a.u. is expected along y direction and the FWHM of the distribution is expected to be about 3 a.u. Figure 4.13 shows what was measured for the shift and the width of the distributions from the ionization experiment of 25 keV proton impact on atomic hydrogen. First all the p_y distribution including the jet was projected, than a gate was put on only the hot gas portion of the data and projected. A subtraction of the hot gas background gave the resulting distribution for the jet. After this analysis we came to the conclusion that our momentum resolution along the y direction is about 2.1 a.u.

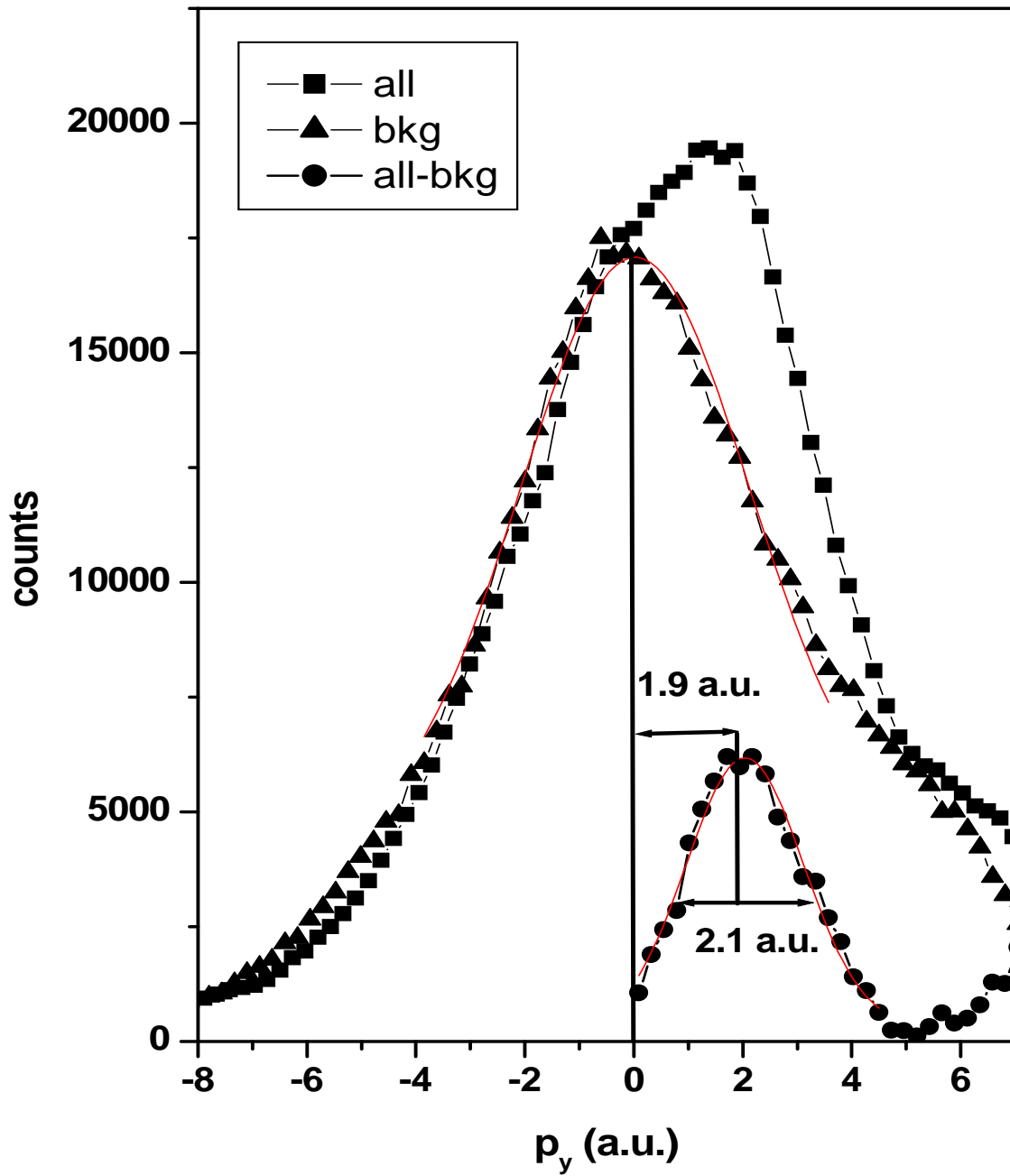


Figure 4.13: Velocity profile of the hydrogen target showing the thermal shift for the case of 25 keV proton impact on hydrogen. The squares correspond to all the data projected and the triangles correspond to the background hot gas projection along the y axis. The subtraction of background from the projection of all the data gives the resulting y distribution.

Chapter 5

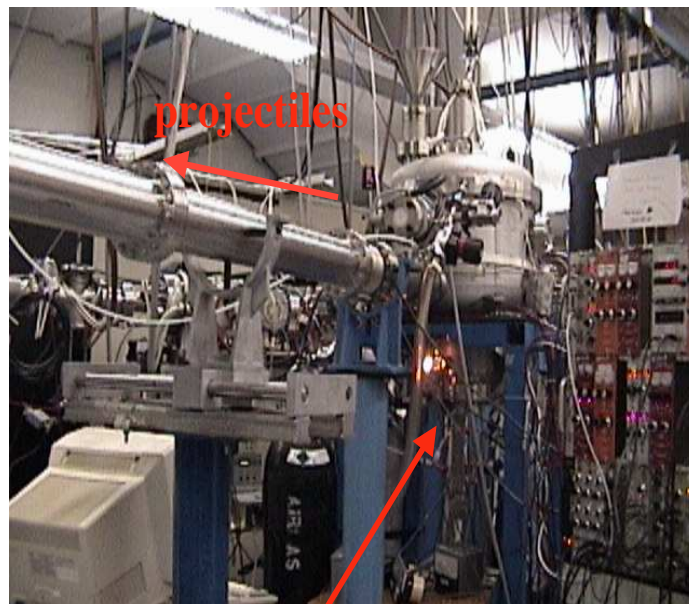
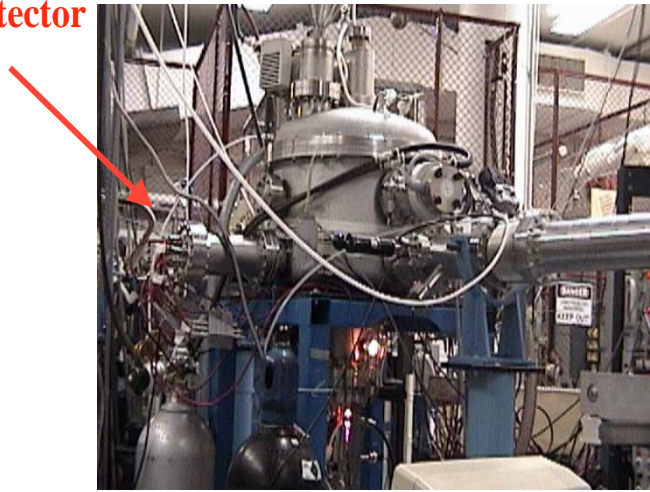
Electron Capture Experiments

5.1 The Technique

In the electron capture experiments studied, Ar^{8+} ions were produced by the KSU-CRYEBIS. The ions were accelerated to voltages between 10 and 70 kV with beam currents ranging from 50 to 150 pA in the collision region. The beam crossed the target jet at right angles. Figure 5.1 shows pictures of the setup for the capture experiments, while Table 5.1 shows the timing parameters. We detected the recoil ions and projectile ions in coincidence. An electric field of 10 V/cm was applied to push the recoils to a two-dimensional recoil position sensitive detector (2D PSD) . The projectiles travelled a distance of 225 cm to arrive at the projectile 2D PSD. The projectiles passed a pair of electrostatic deflection plates on the way for charge separation. This way we were able to deflect the main beam off of the detector and separate Ar^{7+} properly for investigating single electron capture. The TAC was started by the projectile timing signals and ended by the recoil ones. From the experiment the time-of-flight of the recoil ions was obtained.

From the TAC and position information on the detector, the recoil ion momentum was reconstructed by the method explained in Chapter 4 . In the following section, how this

**recoil
position detector**



hydrogen source

Figure 5.1: Pictures of the capture experiment setup.

v	p-TOF	Start	Stop	TAC range
0.32 a.u.	3.189 μs	p	2.5 μs d r	5 μs
0.5 a.u.	2.041 μs	1.5 μs d p	r	5 μs
0.75 a.u.	1.361 μs	1 μs d p	r	5 μs

Table 5.1: Timing parameters of the capture experiments. v is the beam velocity, p is projectiles, r is recoils, TOF is time-of-flight and d stands for ‘delayed by’.

information translated into energy gains of the collisions is explained.

5.2 Evaluation of Energy Gain

From conservation of energy and momentum we can deduce an expression for the longitudinal momentum transfer to the recoil ion ([30]). Taking first the conservation of energy, where E_0 is the initial kinetic energy of the projectile ion and Q is the exoergicity of the collision we can write:

$$E_0 + Q = E_p + E_r. \quad (5.2.1)$$

E_p is the final kinetic energy of the projectile ion (with its captured electrons) and E_r is the final recoil ion kinetic energy. Q is the difference in electronic binding energies of the target and the projectile. From conservation of momentum we can write for the longitudinal and transverse momenta:

$$p_0 = p_{p\parallel} + p_{r\parallel} \quad (5.2.2)$$

and

$$0 = p_{p\perp} + p_{r\perp} \quad (5.2.3)$$

where p_0 is the initial momentum of the projectile ion, p_p is the final momentum of the projectile ion and p_r is the momentum of the recoiling ion. Substituting these into 5.2.1

gives:

$$Q = \frac{p_{p\parallel}^2 + p_{p\perp}^2}{2(m_p + nm_e)} + \frac{p_{r\parallel}^2 + p_{r\perp}^2}{2m_r} - \frac{p_0^2}{2m_p} \quad (5.2.4)$$

where n is the number of electrons captured. Since the kinetic energy of the recoil ion is much less than that of the projectile ion we can neglect the second term in the above equation. Also since $m_e \ll m_p$ Equation 5.2.4 becomes:

$$\begin{aligned} Q &= \frac{p_{p\parallel}^2 + p_{p\perp}^2}{2m_p} \left(1 - n \frac{m_e}{m_p}\right) - \frac{p_0^2}{2m_p} \\ &= \frac{p_{p\parallel}^2 - p_0^2}{2m_p} + \frac{p_{p\perp}^2}{2m_p} - n \frac{m_e}{m_p} \left(\frac{p_{p\parallel}^2 + p_{p\perp}^2}{2m_p}\right), \end{aligned} \quad (5.2.5)$$

This equation can be simplified further by noting that $p_{p\perp} \ll p_{p\parallel}$. This way the square of the transverse momentum can be neglected to give:

$$Q = \frac{(p_{p\parallel} - p_0)(p_{p\parallel} + p_0)}{2m_p} - n \frac{m_e}{2m_p^2} p_{p\parallel}^2. \quad (5.2.6)$$

Now making the approximation that $(p_{p\parallel} + p_0)/m_p = 2v$, where v is the initial beam velocity, further arrangement gives:

$$Q = v(p_{p\parallel} - p_0) - \frac{nm_e v^2}{2}. \quad (5.2.7)$$

Realizing that $\Delta p_{p\parallel} = p_{p\parallel} - p_0$ gives:

$$Q = v\Delta p_{p\parallel} - \frac{nm_e v^2}{2}. \quad (5.2.8)$$

The longitudinal momentum for the recoil ion is given by $\Delta p_{r\parallel} = -\Delta p_{p\parallel}$. Substituting this into 5.2.8 gives:

$$Q = -v\Delta p_{r\parallel} - \frac{nm_e v^2}{2}. \quad (5.2.9)$$

Since we are dealing with single electron capture in this thesis, $n = 1$ and in atomic units $m_e = 1$. In our context, $\Delta p_{r\parallel} = p_z$ where z is the initial beam direction. Finally, 5.2.8

becomes:

$$Q = -v\Delta p_{r\parallel} - \frac{v^2}{2}. \quad (5.2.10)$$

In our experiments we were able to obtain p_z with a resolution between 0.15 to 0.2 a.u. This resolution allowed us to calculate the Q values and thereby separate the final states into which the electron is captured.

5.2.1 Calibration of $p_z = 0$

To be able to identify the right p_z values, the channel corresponding to $p_z = 0$ needs to be known. One way to identify this was to run an experiment with a known Q -value. We ran H^+ on H for which the Q -value is zero for $1s \rightarrow 1s$ transfer. The velocity we chose was $v_p = 1 a.u.$. Zero Q -value corresponds to a p_z of 0.5 a.u. From the physical size of the channel plates detectors (40 mm in diameter) and the time-of-flight information it is known how many channels correspond to an atomic unit of momentum. From this information one can identify the channel that corresponds to $p_z = 0$. Figure 5.2 shows (a) p_z , (b) Q -value and (c) Q vs θ (the scattering angle of the projectile) graphs for $H^+ + H$ at $v_p = 1$ a.u. The scattering angle can be calculated from $\theta = p_{r\perp}/p_0$, where p_0 is the initial projectile momentum. The first peak in the p_z graph of Figure 5.2 corresponds to $1s \rightarrow 1s$ transfer while the second peak is a combination of capture to $2s$ and $2p$ levels of atomic hydrogen.

5.2.2 Time-of-Flight and Recoil Position Spectra

The raw time-of-flight (TAC) spectra for Ar^{8+} on H and H_2 are shown on the left hand side of Figure 5.3. For Figures 5.3(a),(b) and (c) the conversion is 1.7 ns/ch. The recoil detector position spectra on the right side are obtained after putting gates on the raw TAC

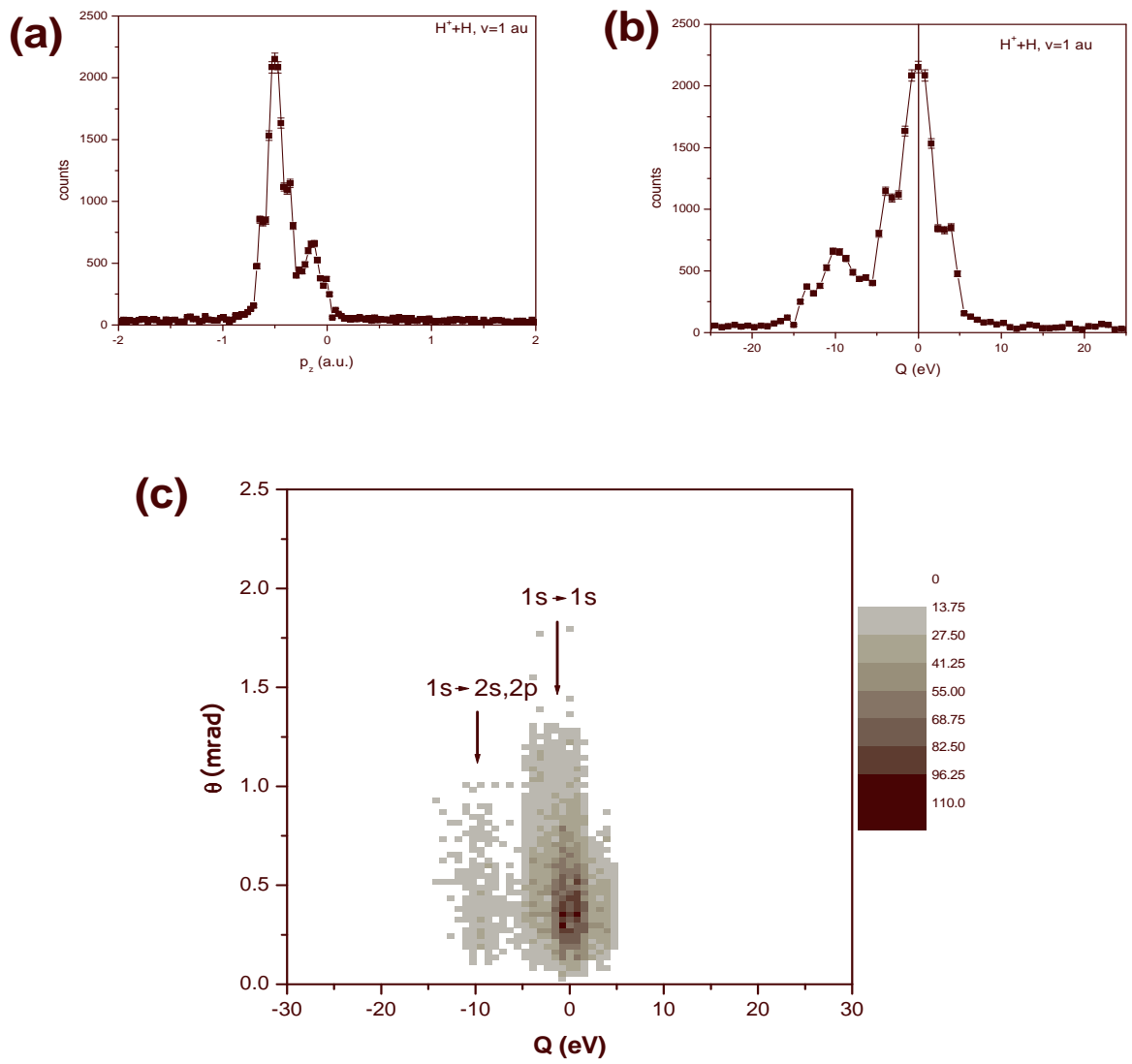


Figure 5.2: (a) p_z , (b) Q -value and (c) Q vs θ for $v_p = 1$ a.u. protons on hydrogen.

spectra on the H^+ peak. For these position spectra approximately 0.5 mm corresponds to one channel. This translates into 8.5 channels per atomic unit of momentum for H and 6 channels per atomic unit of momentum for H_2 . The gates are shown between the red lines on the TAC spectra. The horizontal axes on the recoil position spectra give the position information along the z -axis (beam axis). From this position information and the TAC one can calculate p_z and subsequently the Q -values. On these figures the different n states can be seen. Figure 5.3(d) corresponds to a gated recoil position detector picture under these conditions. Figures 5.3(b) and (c) correspond to the TAC spectra for impact velocities of 0.5 a.u. and 0.75 a.u., respectively. Figures 5.3(e) and (f) are the position spectra that correspond to the gates of Figures 5.3(b) and (c), respectively.

Figure 5.4 shows the raw recoil position spectra on the left hand side. The raw (non-coincidence) recoil spectra are dominated by hot gas. the jet is barely visible. On the right hand side of this figure are the TAC spectra gated on the raw recoil position spectra. The red boxes on the position spectra are the gates. These gates were set to eliminate much of the background due to the hot (non-jet) gas.

Placing this wide gate on the jet helps, but not much. Both H^+ and H_2^+ are visible, but the H_2^+ still has a considerable amount of hot gas contribution which is why the dissociation fraction looks so poor. However, gating the other way as in Figure 5.3, on H^+ first shows that a clear jet emerges. The remaining hot gas comes from the randoms in the TAC peak and it was subtracted by fitting a curve on the remaining background. Now, the different n 's are clearly visible on the recoil spectra. The spread in p_y is mainly due to the Δp_y resolution explained in Chapter 4 and also due to the kinematics of the collision.

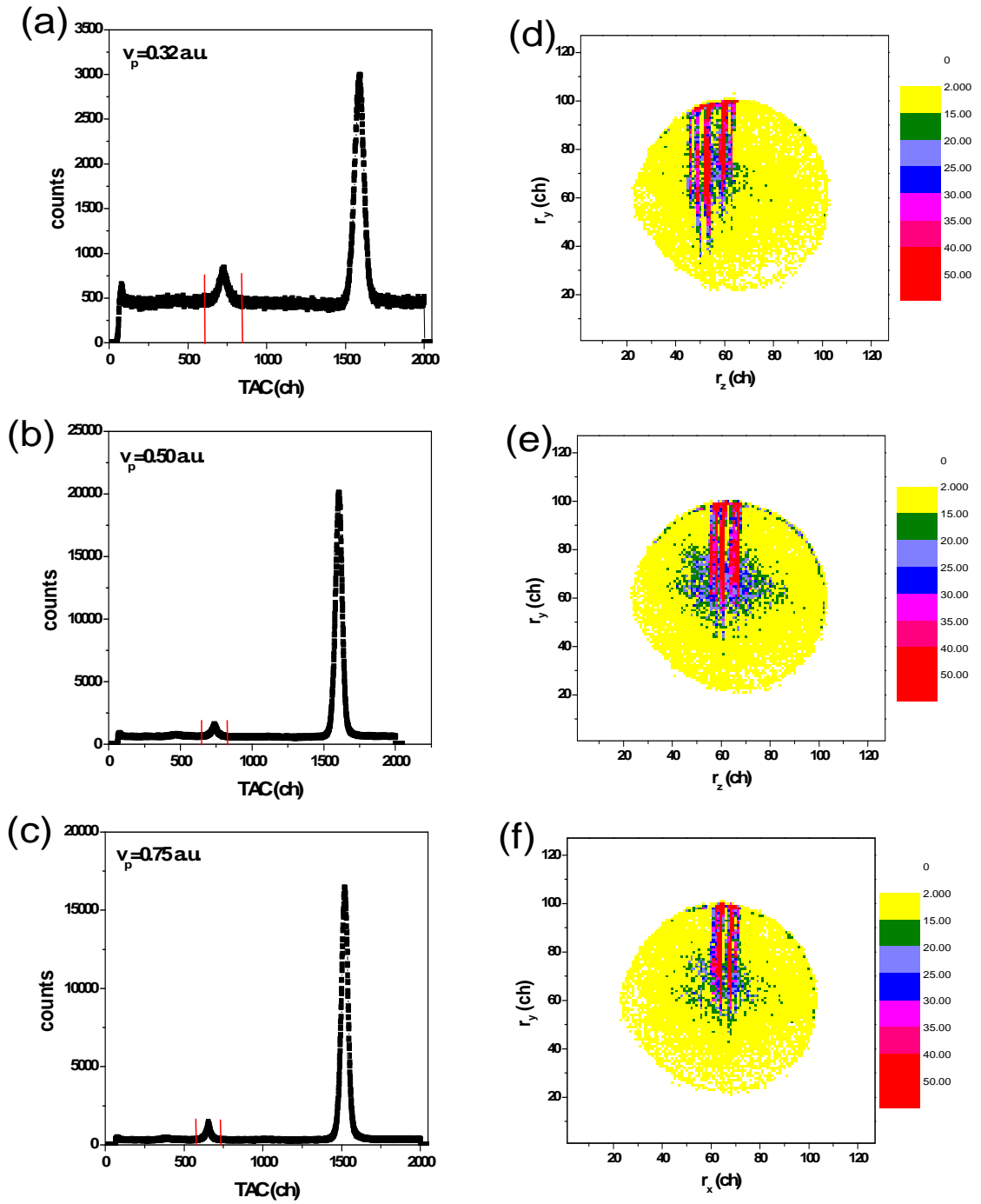


Figure 5.3: left hand side is the raw TAC spectra and right hand side is the recoil position spectra gated on the raw TAC spectra for Ar^{8+} on H and H_2 . The calibration for the TAC spectra is 1.7 ns/ch while for the position spectra it is 0.5 mm/ch, which corresponds to 8.5 ch/a.u. for H^+ .

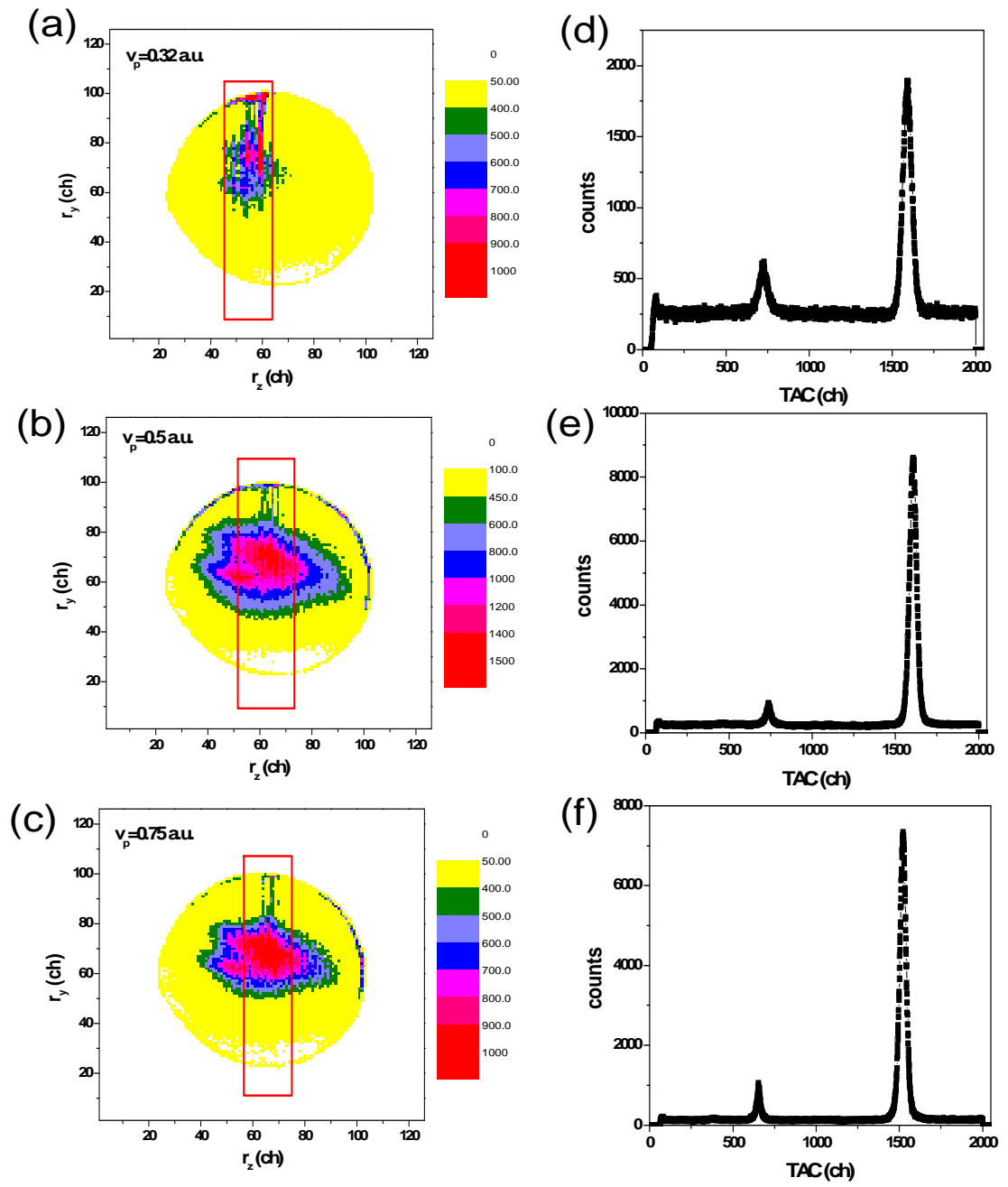


Figure 5.4: left hand side is the raw recoil position spectra and right hand side is the TAC spectra gated on the raw position spectra. The calibrations are the same as Figure 5.3.

5.3 Results

Since we could obtain both H and H_2 data from the same runs, our measurements give a good comparison of these two targets. Results from three different impact energies 0.32, 0.5 and 0.75 a.u. are obtained.

5.3.1 $Ar^{8+} + H$

Figures 5.5, 5.6 and 5.7 show Q -value spectra obtained for projectile velocities of 0.32, 0.5 and 0.75 a.u., respectively. (The remaining background on these figures were attributed to hot gas and subtracted via a fitting of a smooth line.) As predicted by the over-the-barrier model, mostly $n = 5$ and $n = 6$ states of Ar^{7+} are populated. For $v = 0.32$ a.u., the distribution is dominated by $5d$, $6s$ and $6p$ states. Once the velocity is increased to $v = 0.5$ a.u., higher n states start to populate. Also distributions for higher angular momentum states of $n = 5$ and $n = 6$ states start to increase and as the velocity is increased to $v = 0.75$ a.u. this group of higher angular momentum states start to dominate. Similar behavior has been seen previously by Abdallah et. al. ([4]) for Ar^{8+} impact on helium. A physical explanation of this increase is that, as the collision velocity increases, the target electrons have larger angular momenta in the rest frame of the projectile. As the collision velocity is increased rotational coupling starts to play a role which explains why higher l states start to populate.

We have compared our results to a close coupling calculation which uses an atomic basis by Lee and Lin ([31]) that was done for 0.3, 0.45 and 0.7 a.u. In this calculation all states up to $n = 7$ were implemented in the Ar^{8+} projectile center. The Ar^{8+} ion is treated as a

frozen core from which the electron see the potential:

$$V_{Ar}(r) = \frac{-8 - (10 + 5.5r)e^{-5.5r}}{r}. \quad (5.3.1)$$

Tables 5.2,5.3 and 5.4 compare relative cross-sections for different states obtained experimentally to the results of this close-coupling calculation. All cross-sections in these tables are in percent.

The velocity dependence of the higher l population is confirmed by our experiments, but the population of $n = 6$ level is substantially under-calculated. Figure 5.8 shows potential energy curves for $(ArH)^{8+}$ molecule. It is quite surprising that the crossing of curves around 20 a.u. internuclear distance can be so active, since active crossings around 7 – 10 a.u. are more common.

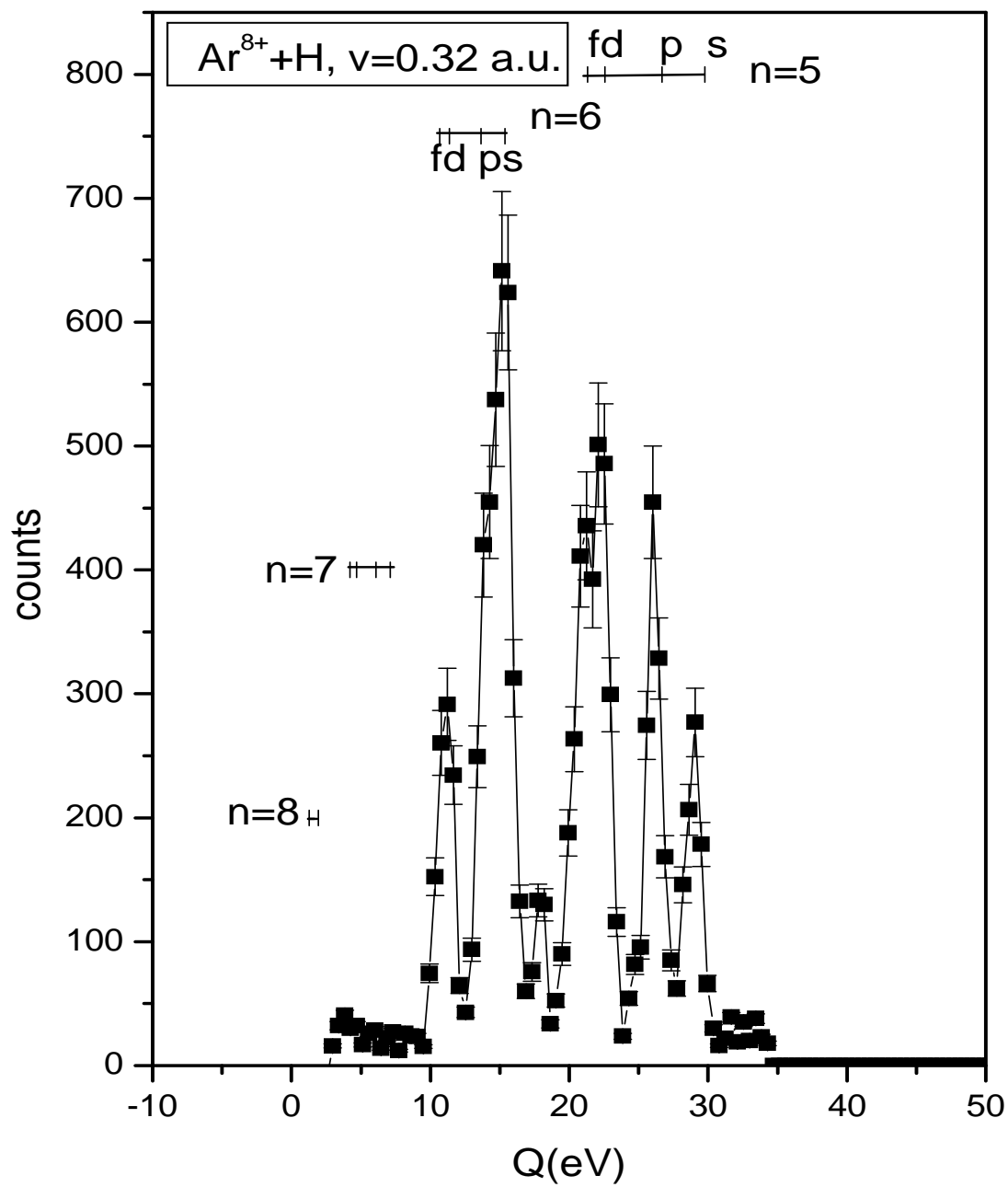


Figure 5.5: Q -value spectra for Ar^{8+} on H at $v_p = 0.32a.u.$

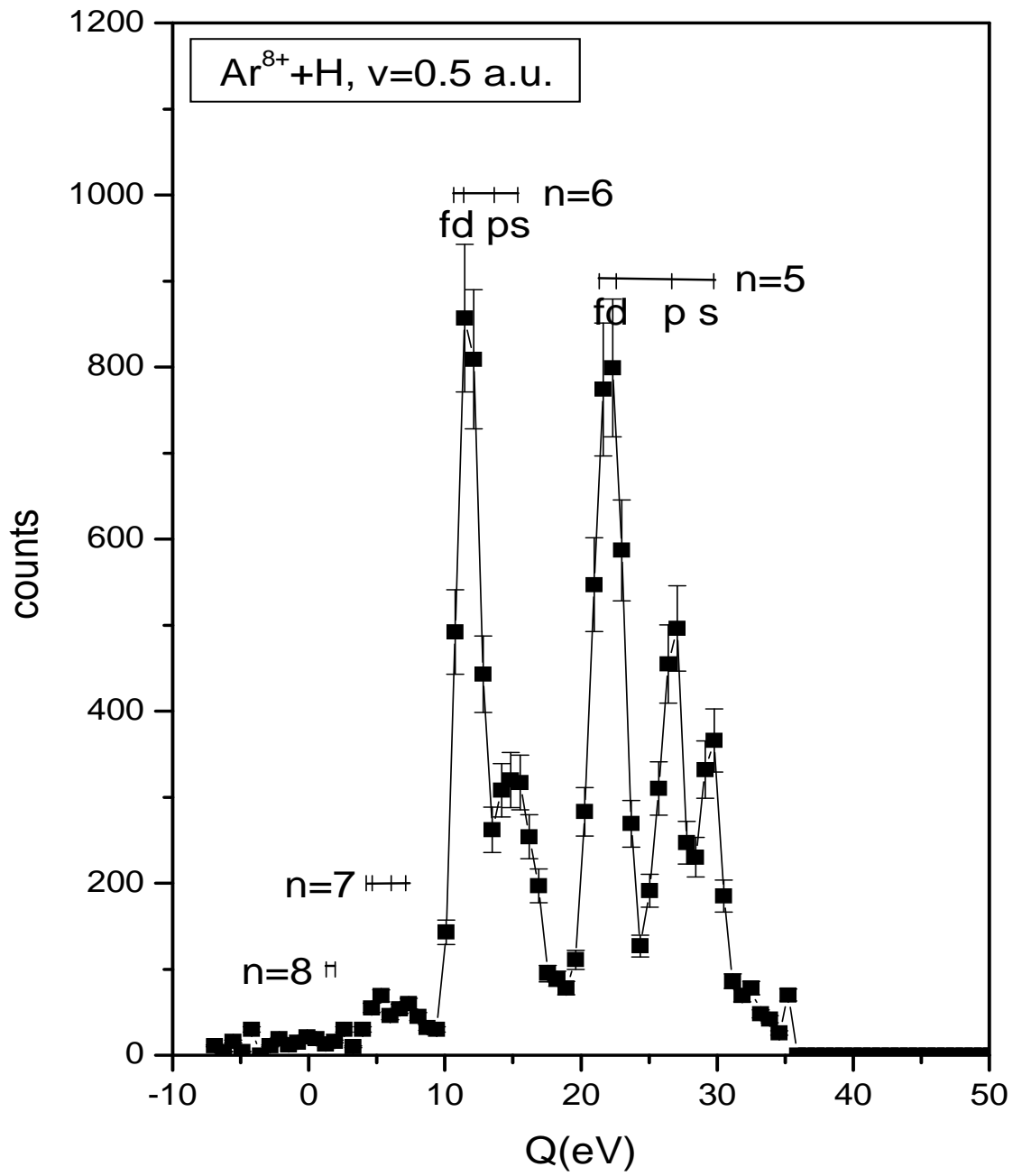


Figure 5.6: Q -value spectra for Ar^{8+} on H at $v_p = 0.5a.u.$

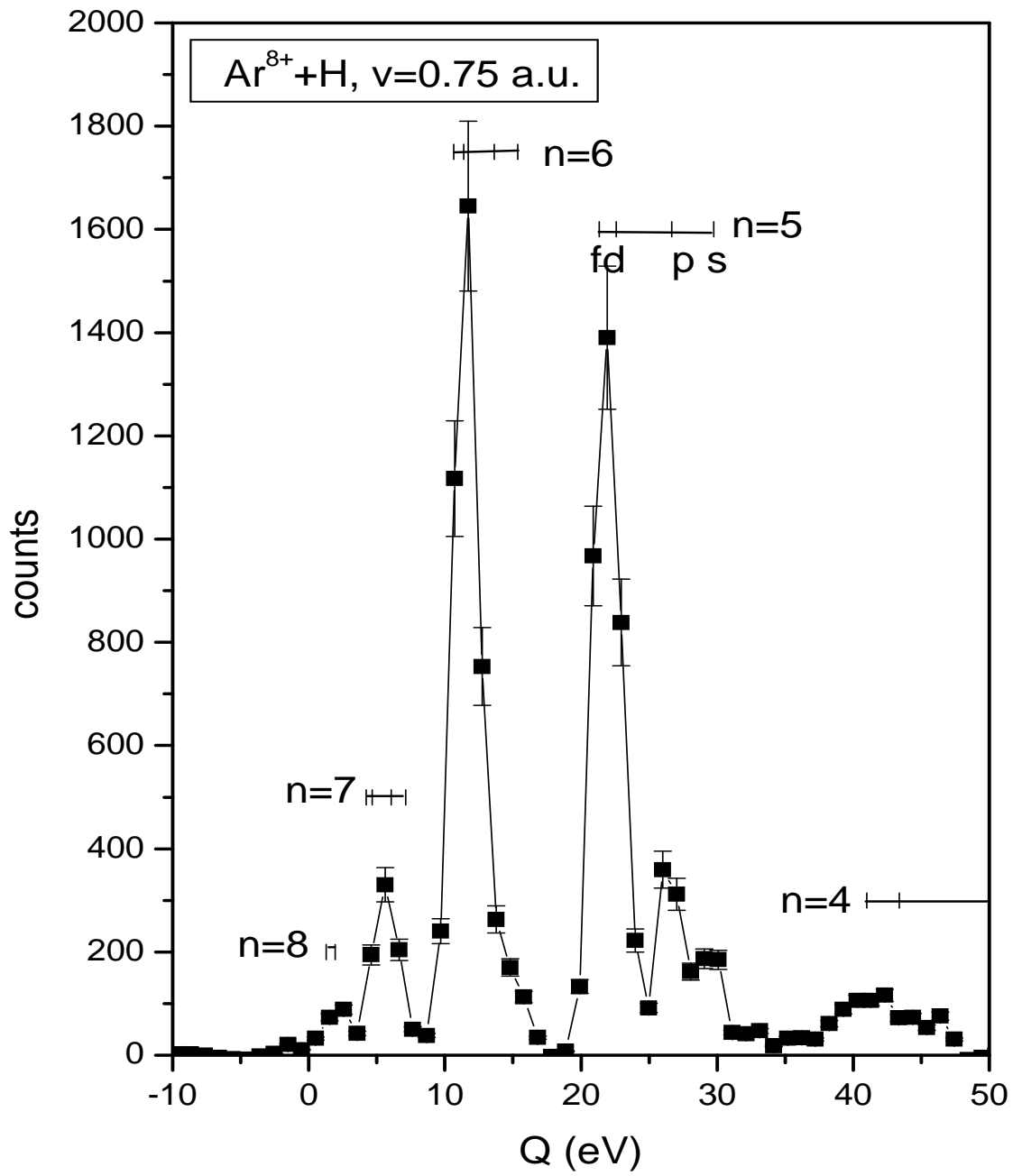


Figure 5.7: Q -value spectra for Ar^{8+} on H at $v_p = 0.75a.u.$

state	experiment	theory
5s	8.058	8.516
5p	14.652	19.64
5d+5f+5g	29.759	43.477
total n=5	52.479	71.633
6s	3.34	13.191
6p	32.5	6.3
6d+6f+6g	10.41	8.863
total n=6	46.25	28.354

Table 5.2: Comparison of relative cross-sections in percent. Close-coupling calculations are done for $v = 0.3$ a.u. and the experimental results are for $v = 0.3$ a.u.

5.3.2 $Ar^{8+} + H_2$

Figures 5.9, 5.10 and 5.11 show Q -value spectra obtained for Ar^{8+} impact on molecular hydrogen for velocities of 0.32, 0.5 and 0.75 a.u., respectively. For $v = 0.32$ a.u. the distribution is dominated by capture into $n = 5$ states. This result agrees very well with the results of Boudjema et. al. [7] for Ar^{8+} impact on D_2 . They also have seen a strong population of $n = 5$ states for this energy with a dominance of higher l states. Giese et. al. [32] also have found that capture into $n = 5$ states dominate for an Ar^{8+} impact on D_2 for $v = 0.28$ a.u. As the impact velocity increases we see a similar type of behavior as seen in atomic hydrogen target results, i.e., higher n (and l) states start to populate.

state	experiment	theory
5s	9.037	10.602
5p	16.298	20.515
5d+5f+5g	29.324	36.585
total n=5	54.659	67.702
6s+6p	15.19	14.537
6d+6f+6g	25.357	17.77
total n=6	40.547	32.303
total n=7	3.3	-

Table 5.3: Comparison of relative cross-sections in percent. Close-coupling calculations are done for $v = 0.45$ a.u. and the experimental results are for $v = 0.5$ a.u.

state	experiment	theory
total n=4	6.57	-
5s	4.212	6.44
5p	7.077	16.031
5d+5f+5g	31.936	42.097
total n=5	43.225	64.568
6s+6p	2.046	6.574
6d+6f+6g	36.568	29.067
total n=6	38.614	35.641
total n=7	7.268	-
total n=8	1.956	-

Table 5.4: Comparison of relative cross-sections in percent. Close-coupling calculations are done for $v = 0.7$ a.u. and the experimental results are for $v = 0.75$ a.u.

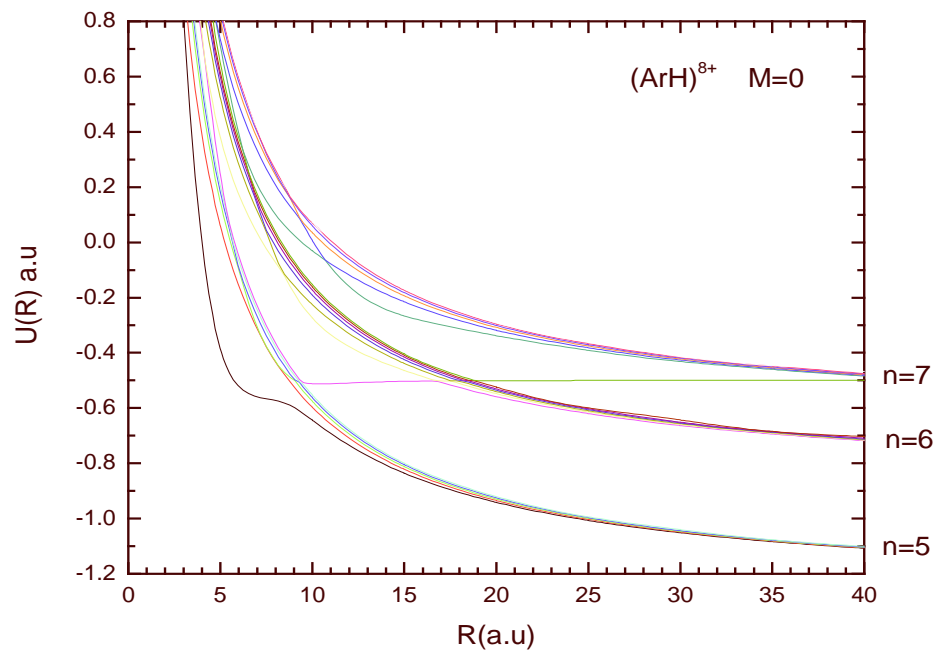


Figure 5.8: The potential energy curves for $(ArH)^{8+}$ molecule. Note the crossings at 7 – 10 a.u. and 20 a.u.

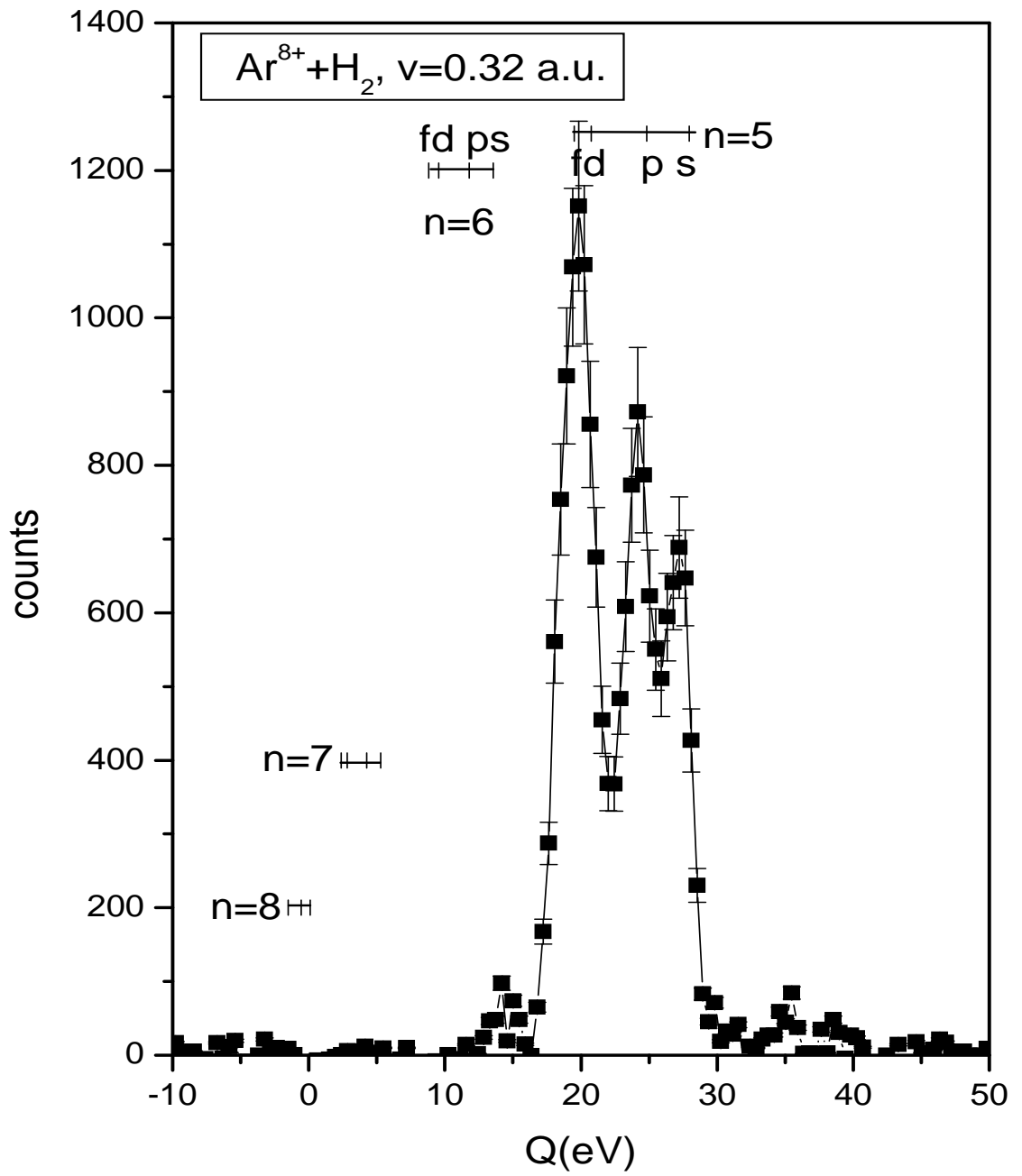


Figure 5.9: Q -value spectra for Ar^{8+} on H_2 at $v_p = 0.32 a.u.$

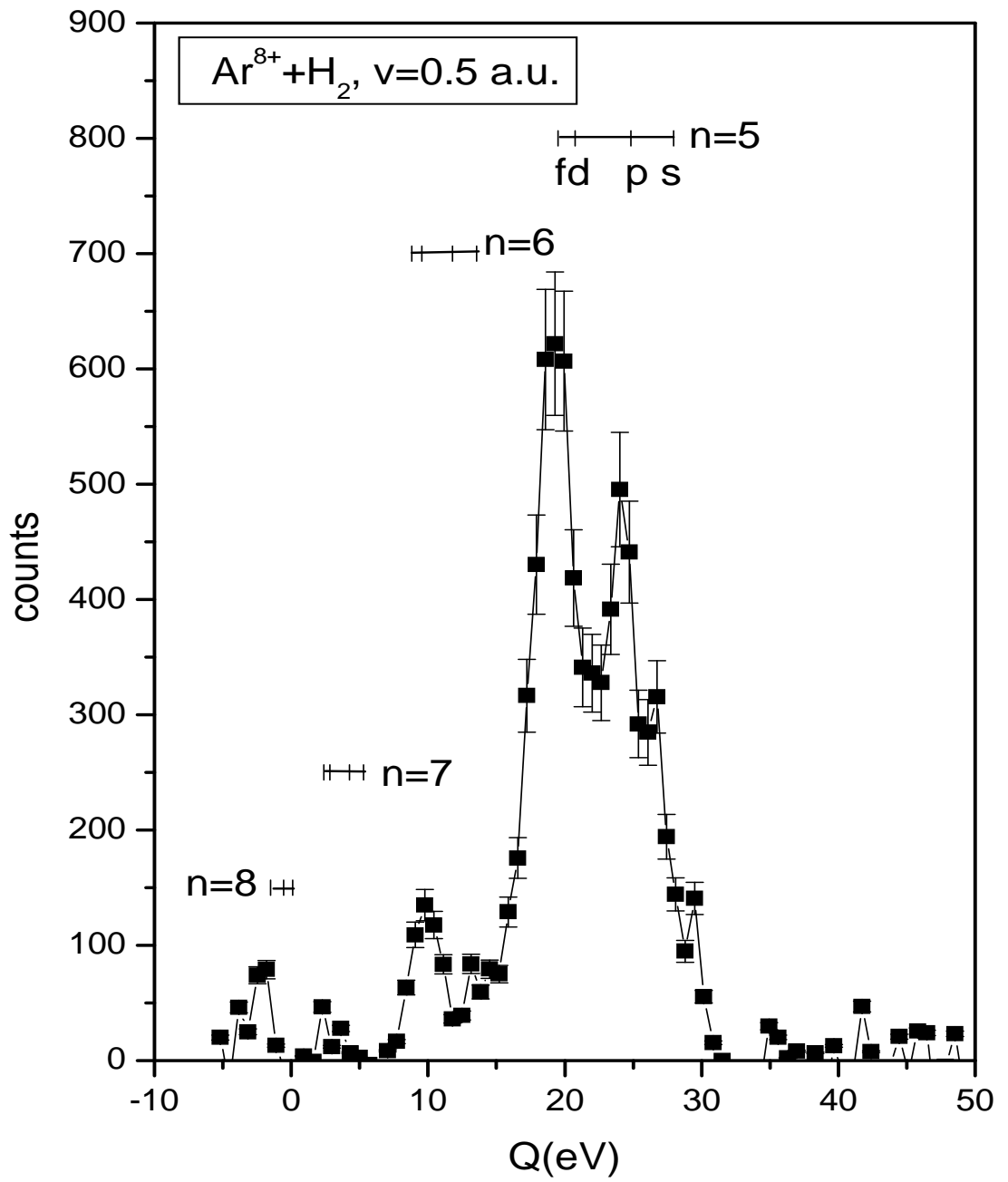


Figure 5.10: Q -value spectra for Ar^{8+} on H_2 at $v_p = 0.5 a.u.$

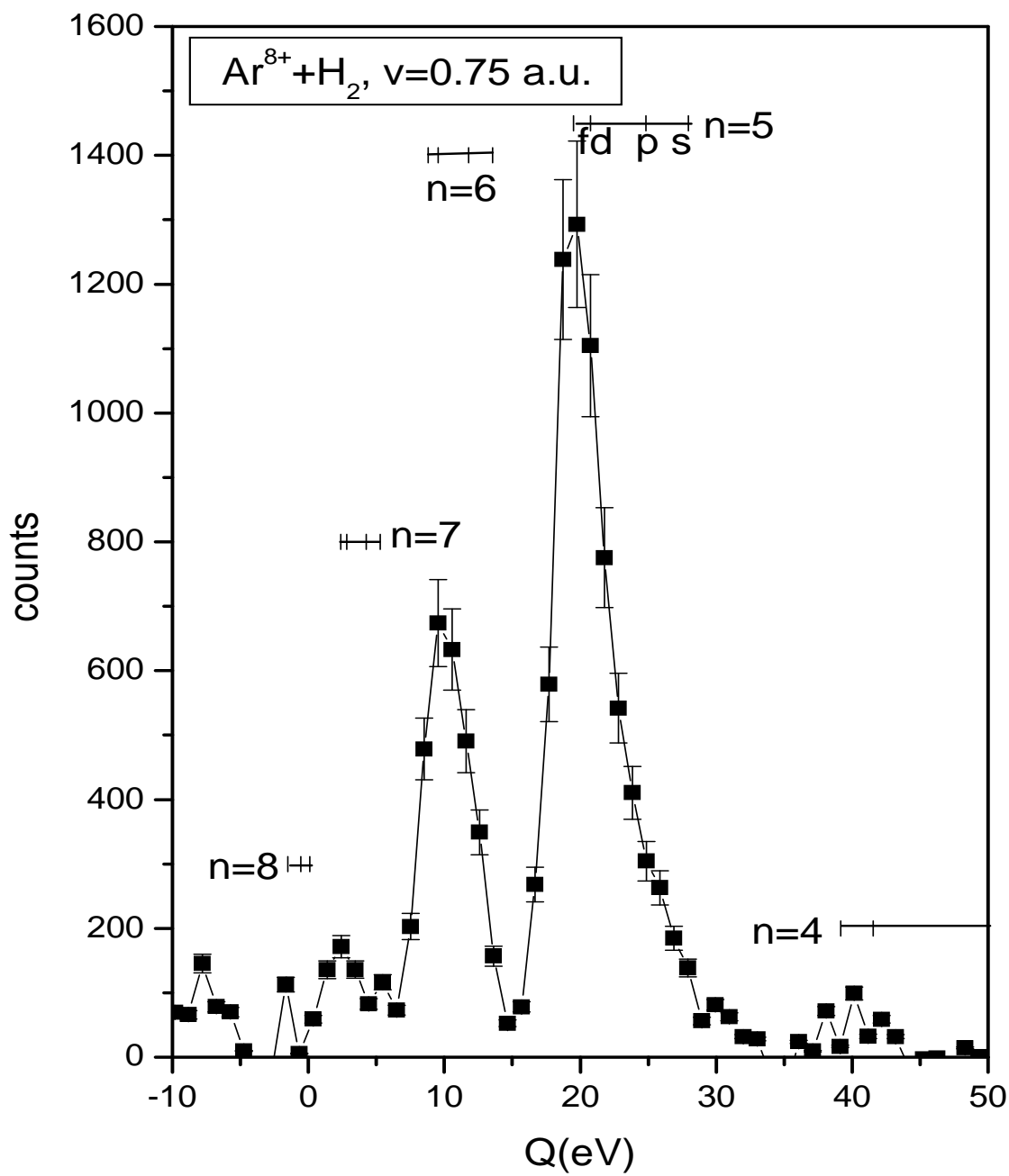


Figure 5.11: Q -value spectra for Ar^{8+} on H_2 at $v_p = 0.75 a.u.$

Chapter 6

Electron Momentum Imaging With A Helium Target

There have been several experiments in the last few years that studied the ionization of He by protons [15, 33]. and studied the electron velocity distributions. These experiments were done for either low or high energy regimes. Before attempting an atomic hydrogen target ionization experiment we decided to do preliminary experiments to reproduce the previous low energy results of proton impact on helium. We also carried out these experiments at intermediate impact energies to bridge the energy gap that existed for this system. These results have been published and most of this chapter is taken from that work [34].

For these experiments high current protons were needed as projectiles. It is very hard to get hundreds of pAmps of protons from the EBIS. We compensated this problem by mounting an ion gun [35] on the EBIS platform which could deliver the high current of protons for the energies we needed. The proton ion beam was collimated by a single aperture to about 1 mm in the collision area. Figure 6.1 shows a picture of this aperture and the collision region. The He target was in the form of a supersonic gas jet. The width of the jet in the collision area was about 3.5 mm and its length product was about 10^{11} atoms/cm². The He gas was first cooled through thermal contact with a cold head

cryopump to about 60 K. The cooled gas was then passed through an aperture of $30 \mu\text{m}$ in diameter. This produced a supersonic flow of the gas. This way most of the thermal velocity was converted into the drift velocity in the direction of the flow of the gas and produced target atoms localized in velocity space. The gas jet was further skimmed with an aperture of 0.5 mm which caused us to keep only the cooler inner part of the jet. In the collision region the internal temperature of the gas was below 1 K, corresponding to a momentum spread of below 0.2 a.u.

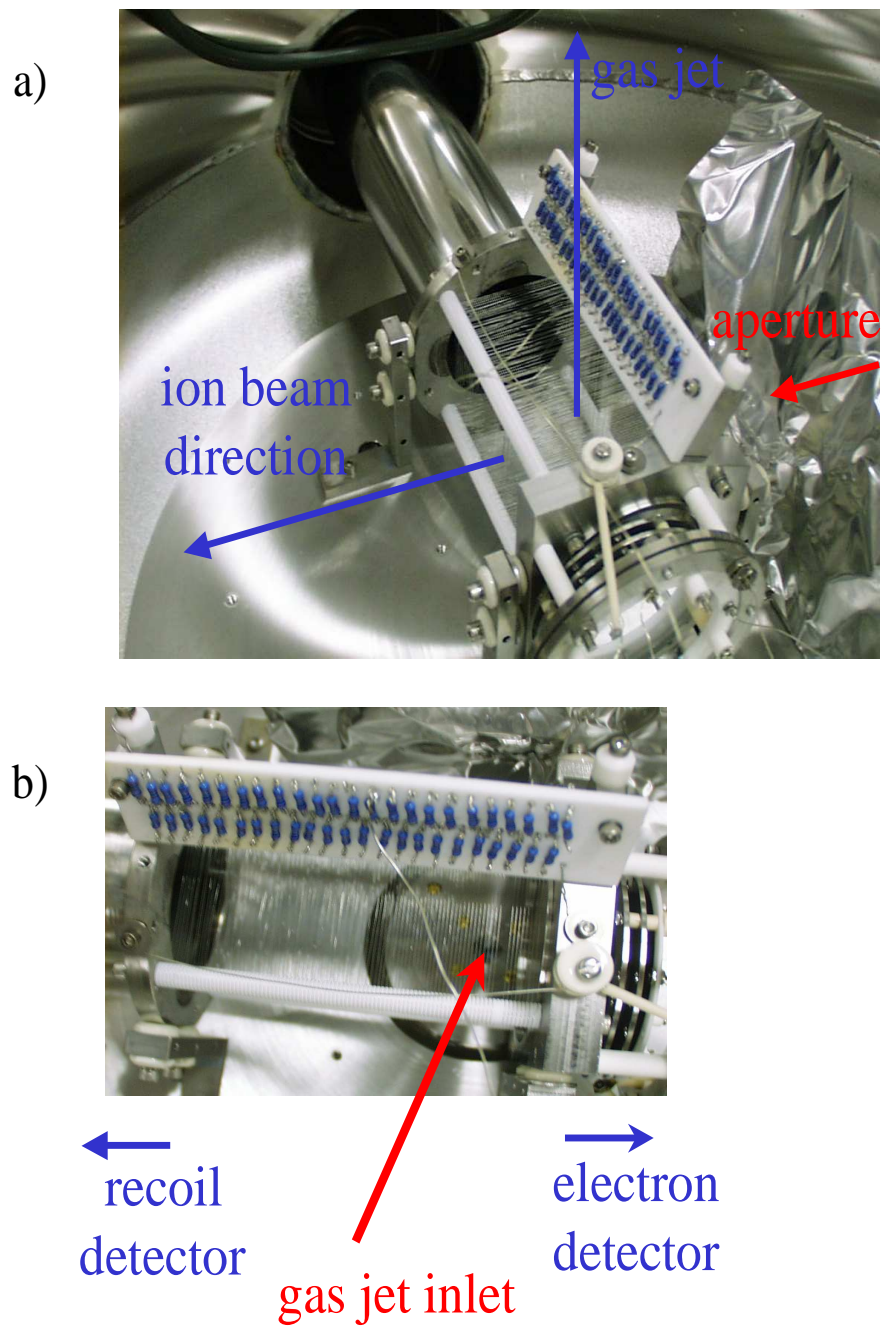


Figure 6.1: (a) collision region showing the aperture, (b) top view of the spectrometer and the collision region showing the gas inlet.

6.1 Results of $H^+ + He$ Experiment

Figure 6.2 shows two-dimensional density plots of the electron velocity spectra projected onto the $y - z$ plane. The recoil momenta have been selected to lie in the negative y -direction, so that these spectra represent pictures of the electron spectra viewed looking ‘down onto’ the collision plane from above, where the collision plane is defined by the beam axis and the direction of the recoil momentum. This view provides the maximum information on the character of the electron velocity distributions, because the electron velocities lie approximately in the collision plane [15]. The units are v_e/v_p where v_e is the electron velocity and v_p is the projectile velocity. Target-centered electron emission would be at the origin and electrons captured to the continuum of the projectile would appear close to the cross at $v_e/v_p = 1$. We see that the forward jet seen by Dörner et. al. remains visible at 20 keV, although the two-fingered structure seen by those authors is not visible at the higher energies. As the projectile velocity increases we see that the electron distribution becomes more and more target centered, as expected.

Figures 6.3(a) and 6.4(a) show projections of the data of Figure 6.2 onto the longitudinal and transverse axes, respectively. In the longitudinal projections of Figure 6.3(a), the progression of the distribution from a ‘saddle-centered’ distribution to a ‘target-centered’ one is apparent. These data thus document the transition from the molecular-orbital regime to the perturbative regime. The corresponding transverse projections are shown in Figure 6.4(a). The 20 keV transverse momentum distribution is consistent with the 15 keV results of [15]. Both distributions show an asymmetry biased toward the direction of the recoiling target ion. Going to higher impact energies, there is perhaps a very weak tendency in the present data for the oscillation to continue, shifting slightly to the opposite side of the recoil

at 40 keV and slowly coming back to being nearly symmetric at 100 keV. We note that the model proposed by Macek and Ovchinnikov [12] would not predict further oscillation of the distribution above 20 keV, since the phase difference between σ and π amplitudes has already become small at this energy and can only approach zero at higher energies.

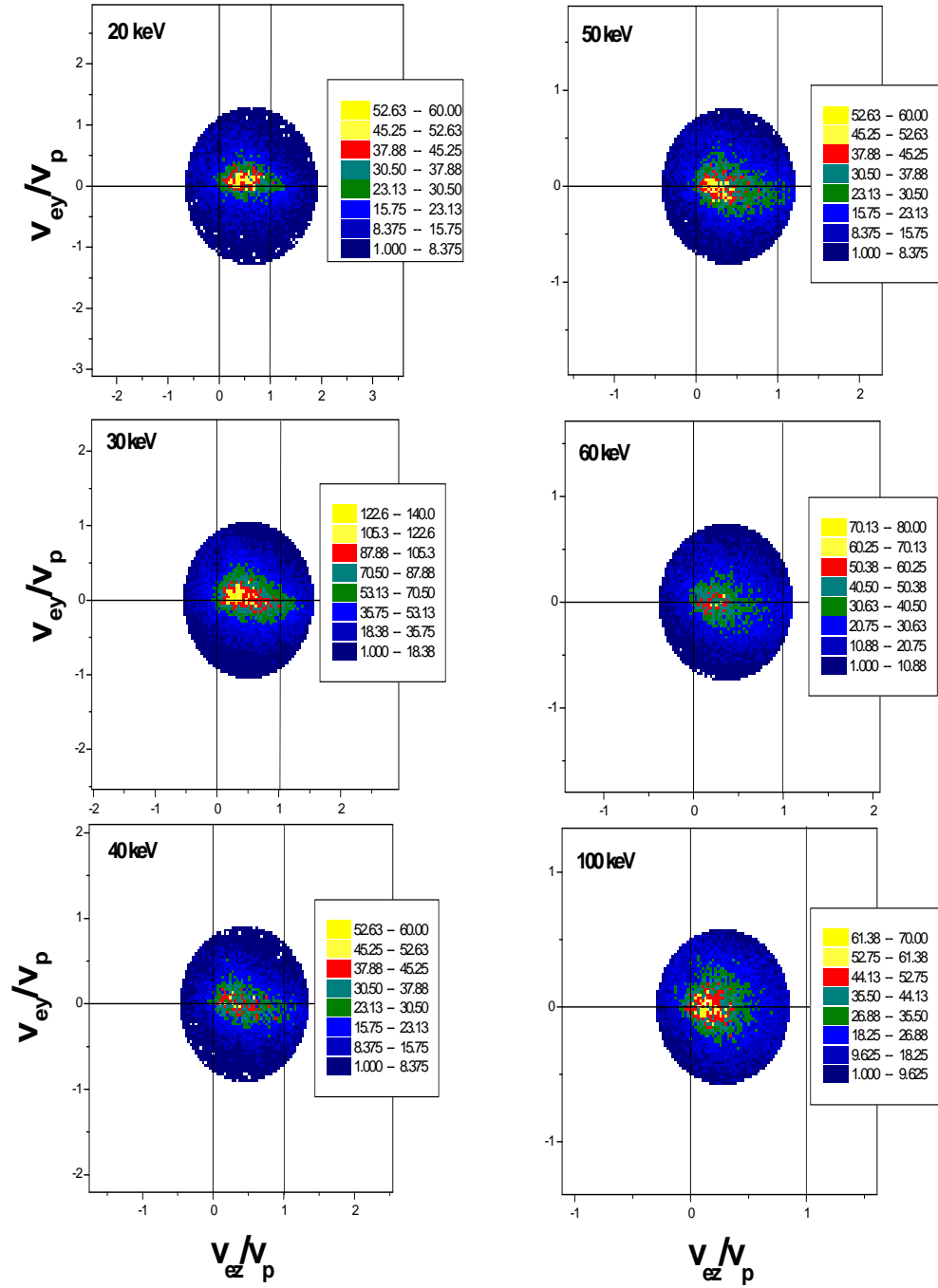


Figure 6.2: Density plots of the electron velocity spectra projected onto the $x - z$ plane. The recoil momentum is defined to be in the $-y$ direction.

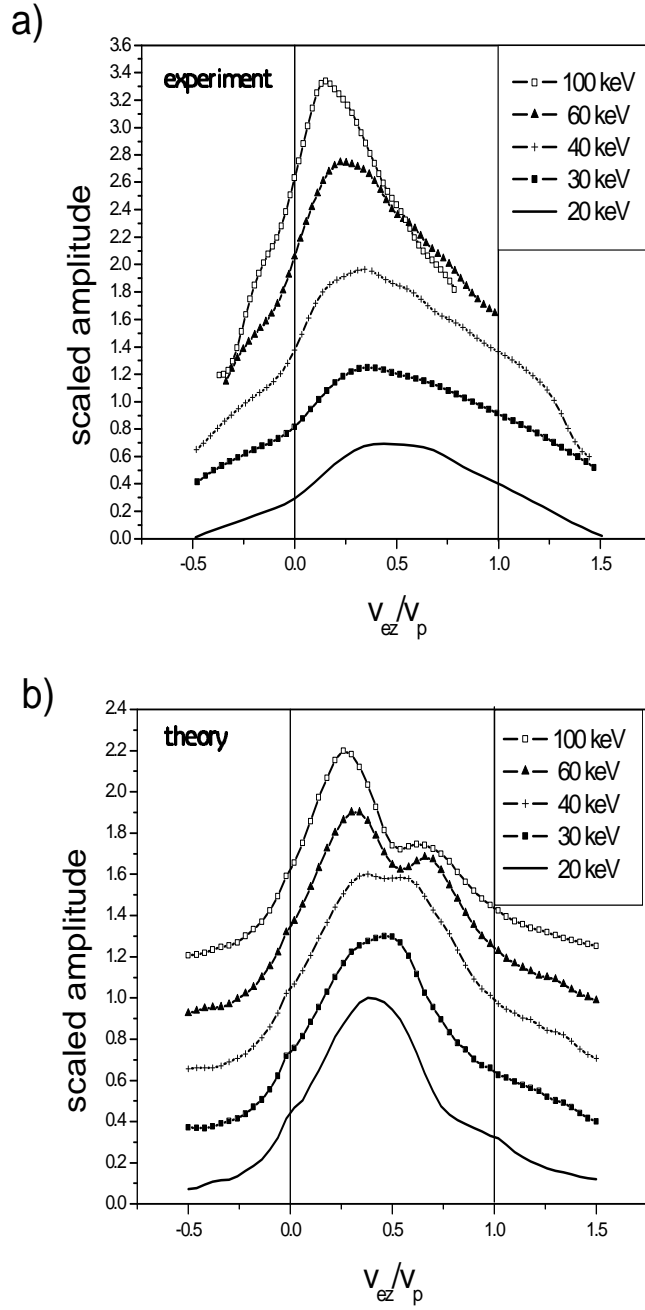
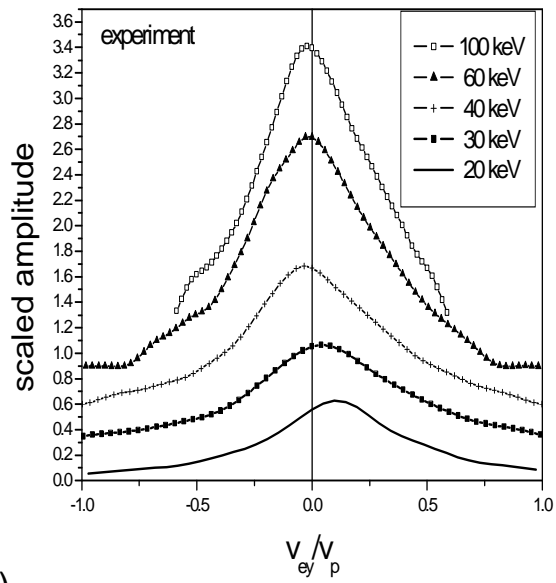


Figure 6.3: Longitudinal momentum distributions of the ejected electrons. (a) Experiment, (b) Theory ($b = 1.5$ a.u.). To guide the eye we have shifted each curve vertically by 0.25 for each increasing energy.

a)



b)

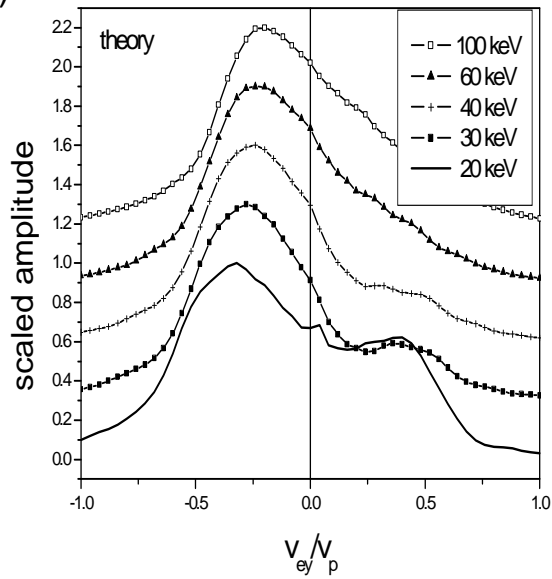


Figure 6.4: Transverse momentum distributions of the ejected electrons. (a) Experiment, (b) Theory ($b = 1.5$ a.u.). To guide the eye we have shifted each curve vertically by 0.25 for each increasing energy.

6.1.1 Comparison of Theoretical and Experimental Results

In order to provide a theoretical framework for the interpretation of the above results, we have compared them to the results of two-center momentum space discretization (TCMSD) method developed by Sidky and Lin [13]. This method assumes a hydrogenic target with a nuclear effective charge of 1.345 for the He target atom.

The TCMSD theory gives the wave function of the active electron in the form of a two-center expansion in momentum space, while the target is taken at rest. To obtain the ejected electron momentum distributions, the projections of the incoherent sum of the target and projectile probability distributions are taken. The TCMSD propagation is not capable of reaching very large times at which we could compare directly with experimental results, but there is still much that can be learned from the analysis of the momentum space wave function at and leading up to the final calculated time. Comparison directly with experiment should also involve an integration of the momentum distributions over the impact parameter, but for the qualitative discussion that follows one impact parameter is sufficient.

For the longitudinal distributions, experimental Figure 6.3a and Figure 6.3b results appear to be in reasonable agreement. Both theory and experiment show a peak near $v_p/2$ for the 20 keV collision. As the impact energy increases, both sets of results show a shift toward the target. The width of the theoretical longitudinal momentum distribution appears also to be consistent with the experiment. The major difference is that the theory shows a small bump near the projectile for the highest impact energies, which is not seen in the experiment. This, however, is not a serious discrepancy when one considers that the theory stops at a finite time and shows results for only one impact parameter. The results

for the longitudinal momentum distributions come as no surprise since it is known that the ejected electron momentum distribution is target centered at high energies, but the time evolution of the longitudinal momentum distribution, shows an interesting evolution towards this expected result.

For the transverse distributions, theoretical results, shown in Figure 6.4(b), do not show the same behavior as the experiment (Figure 6.4(a)). The theoretical distributions are wider than those of the experiment. Furthermore, the impact energy dependence is not the same. At 20 keV, the transverse momentum distribution of the ejected electron is nearly symmetric, showing a slight tendency to go away from the recoil. At 40 keV and higher, experiment and theory are in qualitative agreement, with both showing asymmetry away from the recoil. Although the experimental and theoretical result appear to disagree, the difference could be coming from the finite ending time of the theoretical calculation.

Much of the discrepancy between theory and experiment is probably due to the fact that it has not been feasible to carry out the calculation for a vt product beyond about 30 a.u. There is evidence that there is considerable evolution of the electron distributions after these times, even for such large distances from the collision region. Figures 6.5(a) and (b) show the evolution of the transverse momentum distribution of the ejected electron for the 20 keV and 100 keV collisions, respectively. A feature common to both figures is that they both show a narrowing of the distribution as time progresses. This is expected, since the Coulomb forces from both centers act to slow the electrons ejected transverse to the internuclear separation. An extrapolation of this narrowing could produce a result consistent with the width of the experimental measurements in Figure 6.4(a). Looking at the earliest frame from both collision energies, the distributions are asymmetric, tending

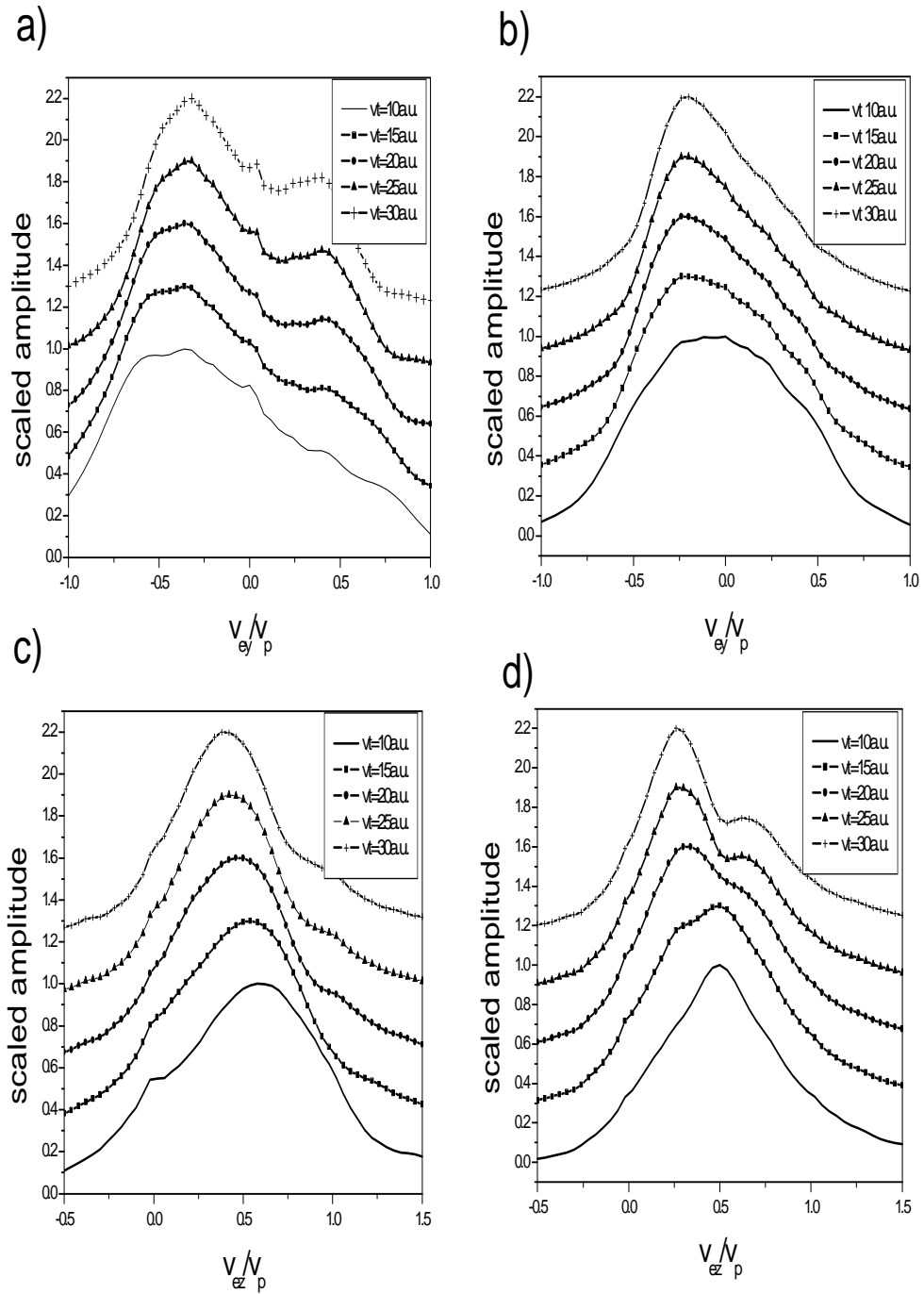


Figure 6.5: Calculated vt dependence of the momentum distributions for ejected electrons. (a) Transverse momentum at 20 keV, (b) transverse momentum at 100 keV, (c) longitudinal momentum at 20 keV and (d) longitudinal momentum at 100 keV. to guide the eye each curve is shifted vertically by 0.25 for each increasing energy.

to go in a direction opposite the recoil. (The recoil momentum is defined to be in the -y direction.) In fact, if one examines the distributions at approximately equal times, $vt = 10$ for the 20 keV collision and $vt = 20$ for the 100 keV collision, the transverse momentum distributions look very similar. This points to the possibility that the same mechanism is responsible for the initial ejection of the electron. As time goes on, the saddle potential plays a larger role for the low energy collision and causes the transverse momentum distribution to evolve toward the direction of the recoiling ion. The plots in Figure 6.5 stop at $vt = 30$, so it is not known whether or not the theoretical distribution will eventually move completely to the side of the recoiling ion as the experimental result in Figure 6.4(a) shows.

In Figures 6.5(c) and (d) the time evolution of the longitudinal momentum distributions corresponding to 20 keV and 100 keV collisions is respectively shown. The 20 keV collision at $vt = 10$ a.u. shows a distribution, though very broad, centered roughly at the saddle velocity (the saddle velocity is slightly faster than $v/2$ since the target ion charge is larger than the projectile charge in the TCMSD model). As vt increases the distribution sharpens slightly and shifts toward the target ion. If saddle point ionization were the only mechanism for ionization, the peak of the longitudinal momentum distribution would remain faster than $v/2$. Instead the distribution migrates toward the higher target nuclear charge. For the high-energy collision in Figure 6.5(d), longitudinal momentum peaks at the high velocity of $v/2$ immediately after the collision at $vt = 10$. Subsequently, the electrons slow rapidly to the velocity roughly consistent with experiment, Figure 6.3(a). As with the transverse distributions, there is a striking similarity of the longitudinal momentum distributions immediately after the collision at equal times and in unscaled momentum, see $vt = 10$ in

Figure 6.5(c) and $vt = 20$ in Figure 6.5(d). This again points to the interesting speculation that the mechanism for the initial electron ejection is similar in both collisions.

As discussed in several previous work, cooling on the ridge is an important link between ionization at finite vt and infinite vt [36]. The broad aspect ratios predicted by quantal calculations, which extend only to finite vt are now well established. The aspect ratios for classical-trajectory-monte-carlo (CTMC) calculations, which do extend to infinite vt , are much narrower and closer to the experimental results [38, 36, 15]. It would be quite helpful to have a general procedure, which will analytically continue the results at finite vt to infinity. A preliminary calculation of this type has recently been carried out by Macek, et al. [37], who used results from a configuration-space lattice calculation by Schultz et. al. [14], for p on H . They then analytically propagated these from finite time to infinite time, using a time-dependent harmonic-oscillator propagator. The results showed distinct narrowing of the transverse momentum distributions and the production of electron distributions with an aspect ratio much closer to the experiments for similar systems than has been calculated previously. The results of this calculation and those of TCSMD method both support the conclusion that the major disagreement between theory and experiment in the width of the transverse distributions can be attributed to a long-range transverse ‘cooling’ of the electrons in the gradually disappearing saddle potential as the collision partners depart.

Chapter 7

Electron Momentum Imaging With An Atomic Hydrogen Target

As discussed in the earlier sections of this thesis, all the theoretical work done on low energy ionization is based on assuming a one-electron hydrogenic target. There have not been full electron momentum imaging experiments carried out with the only true one-electron target atomic hydrogen directly to compare to these theories. In this section we discuss the use of our atomic hydrogen target for such an experiment. We have investigated ionization for proton impact on atomic hydrogen for proton energies of 15, 25 and 50 keV.

7.1 The Experimental Method

The method used here is along the lines of the COLTRIMS technique explained in the previous section. The coordinate system used throughout this thesis remains the same. The ion beam was collimated to 1 mm by a double aperture setup pictured in Figure 7.1. The reason for this double aperture was to reduce background electrons as much as possible. The H atoms left the discharge tube through a 1 mm nozzle and then entered the chamber via a 0.5 mm skimmer. This geometrical cooling allowed for cooling of the gas in the x and z directions, yet it remained hot in the y direction. More detail on the gas jet

characteristics was given in Chapter 3. The recoil ions and the electrons were extracted toward position sensitive detectors via an external field of 10 V/cm. A low negative bias voltage (-5 V) was applied on the top channel plate of the electron detector to reject background electrons. The spectrometer dimensions are same as describe in Chapter 3.

The data analysis was done as follows: from the raw TAC spectra the H_2 coincidences were eliminated and those of H coincidences were chosen via the gates shown on the left hand side of Figure 7.2. The corresponding recoil position spectra are shown on the right hand side of the same figure. These recoil ion spectra still include some random coincidences. However, most of these are associated with the hot gas. On the right hand side of Figure 7.2 2 stripes are seen on the recoil ion position spectra. These stripes correspond to ionization and capture events. For the rest of the data reduction only those events that corresponded to the ionization were chosen.

To identify the collision plane, we examined the transverse momentum vector of the recoil. The recoil momentum p_{rx} along the x direction was constructed first from the TAC. p_{ry} was obtained from the position information on the recoil detector. The top graph in Figure 7.3 shows p_{rx} vs p_{ry} . The transverse momentum is:

$$p_{rtr} = (p_{rx}^2 + p_{ry}^2)^{1/2}. \quad (7.1.1)$$

The bottom graph in Figure 7.3 shows p_{rtr} vs phi. The angle phi is the azimuthal angle defined by the angle the transverse momentum makes with the x axis. The red box on this graph is an example of a gate that can be chosen. By choosing different transverse momenta we are able to choose the collision plane. The angle phi was chosen to be 40° wide. Note that this selection allowed us to reduce the hot gas distribution and choose the recoil ions that were going ‘upward’ in the $+y$ direction.

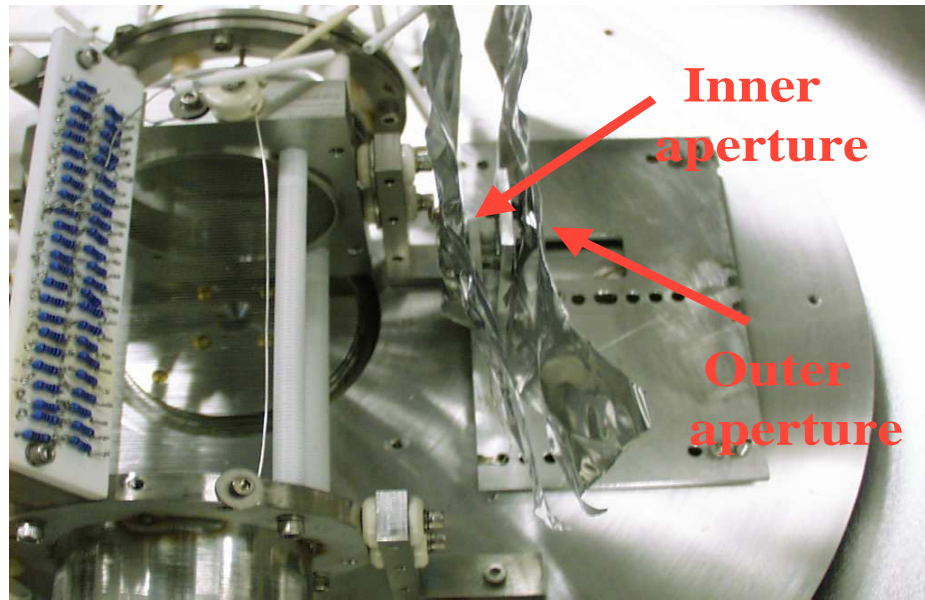


Figure 7.1: Double aperture used to collimate the ion beam. The outer aperture has a 2,5 mm diameter while the other one has a 1 mm diameter.

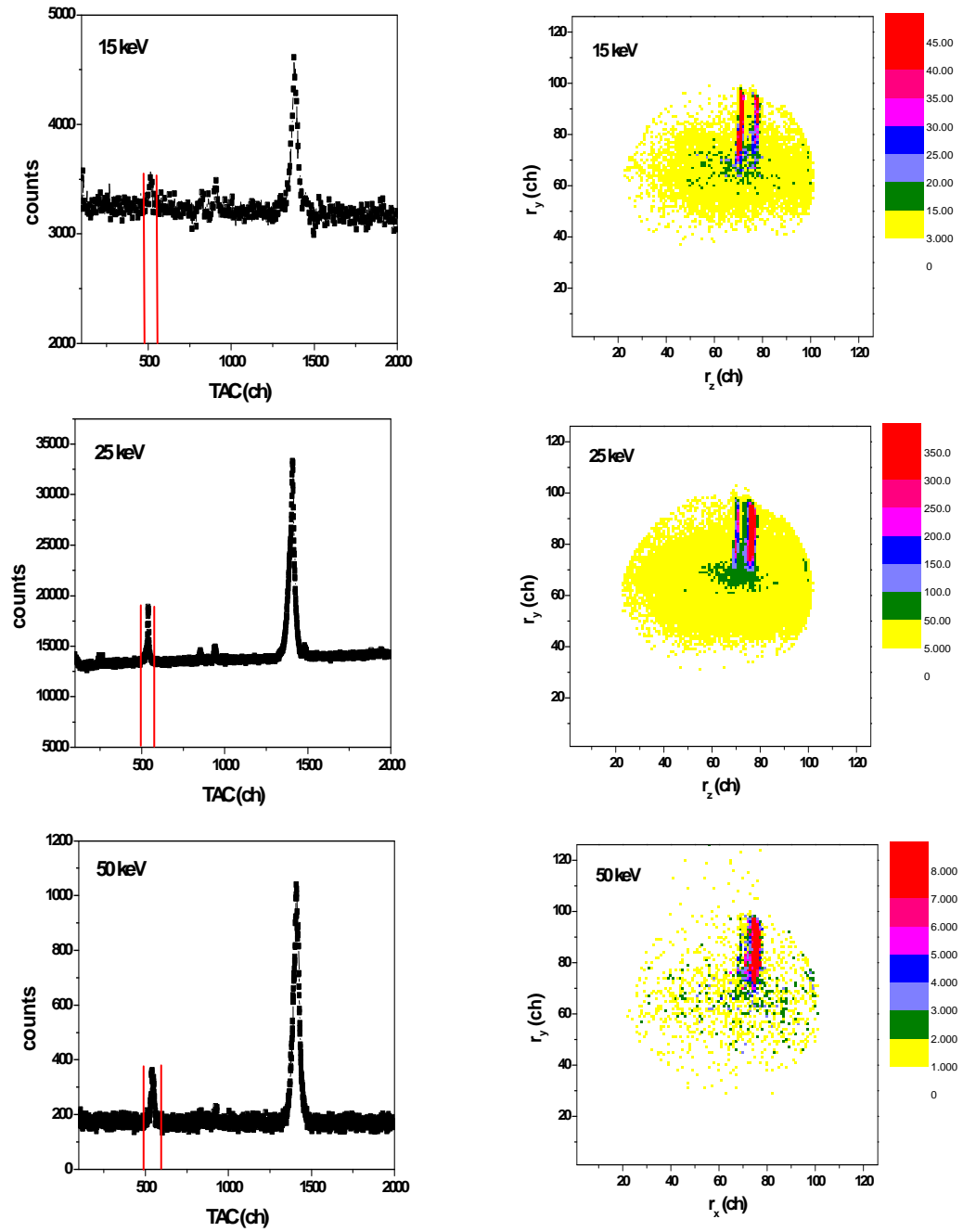


Figure 7.2: left hand side is the raw TAC spectra and right hand side is the recoil position spectra gated on the raw TAC spectra.

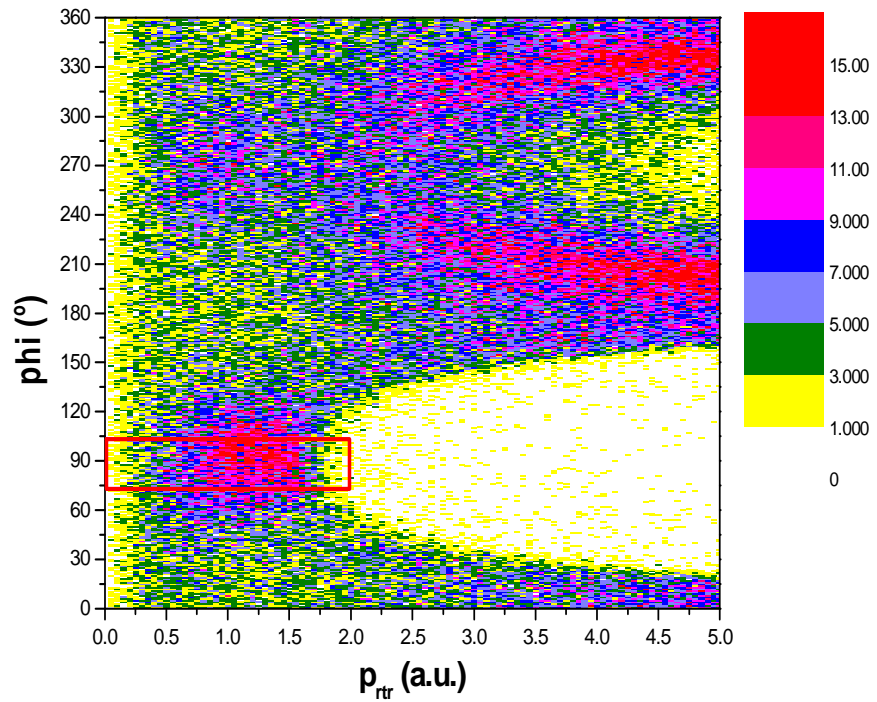
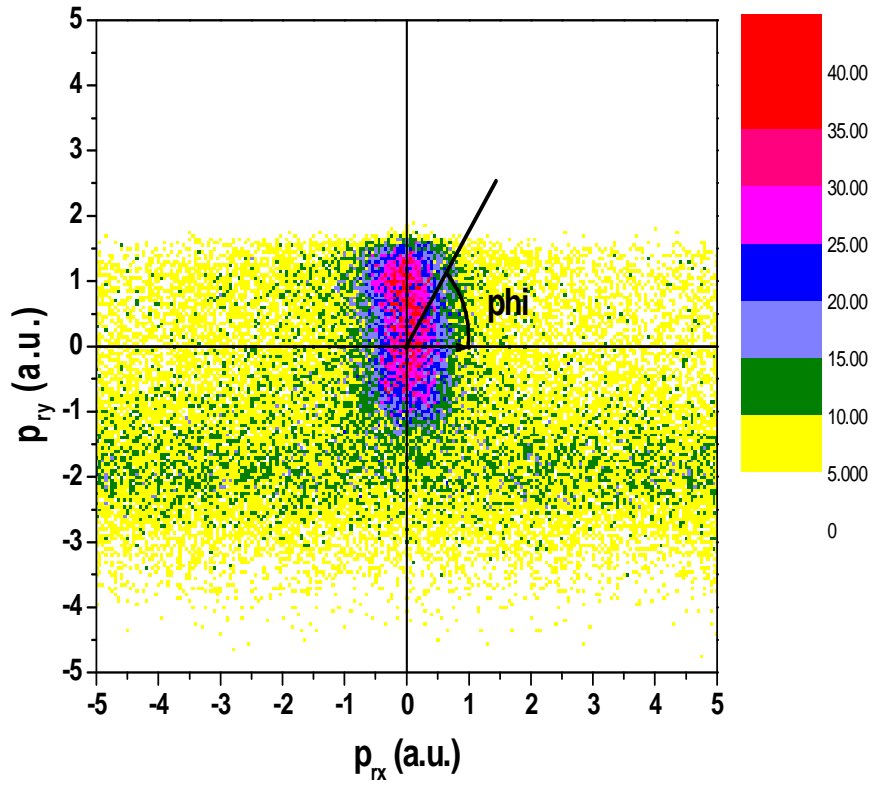


Figure 7.3: p_{rx} vs p_{ry} and p_{rtr} vs ϕ for 25 keV proton impact on H . This plots are obtained after the gates are set on events corresponding to H^+ coincidences and ionization.

Electron Detector Calibration

One needs to know where the center of the electron detector is to be able to create electron velocity distributions. The calibration of the detector for this purpose was achieved by reversing the spectrometer voltages and allowing the heavy recoil ions to hit the electron detector. Figure 7.4 shows the recoil ions on the electron detector and the projections of this detector onto the y and z axes.

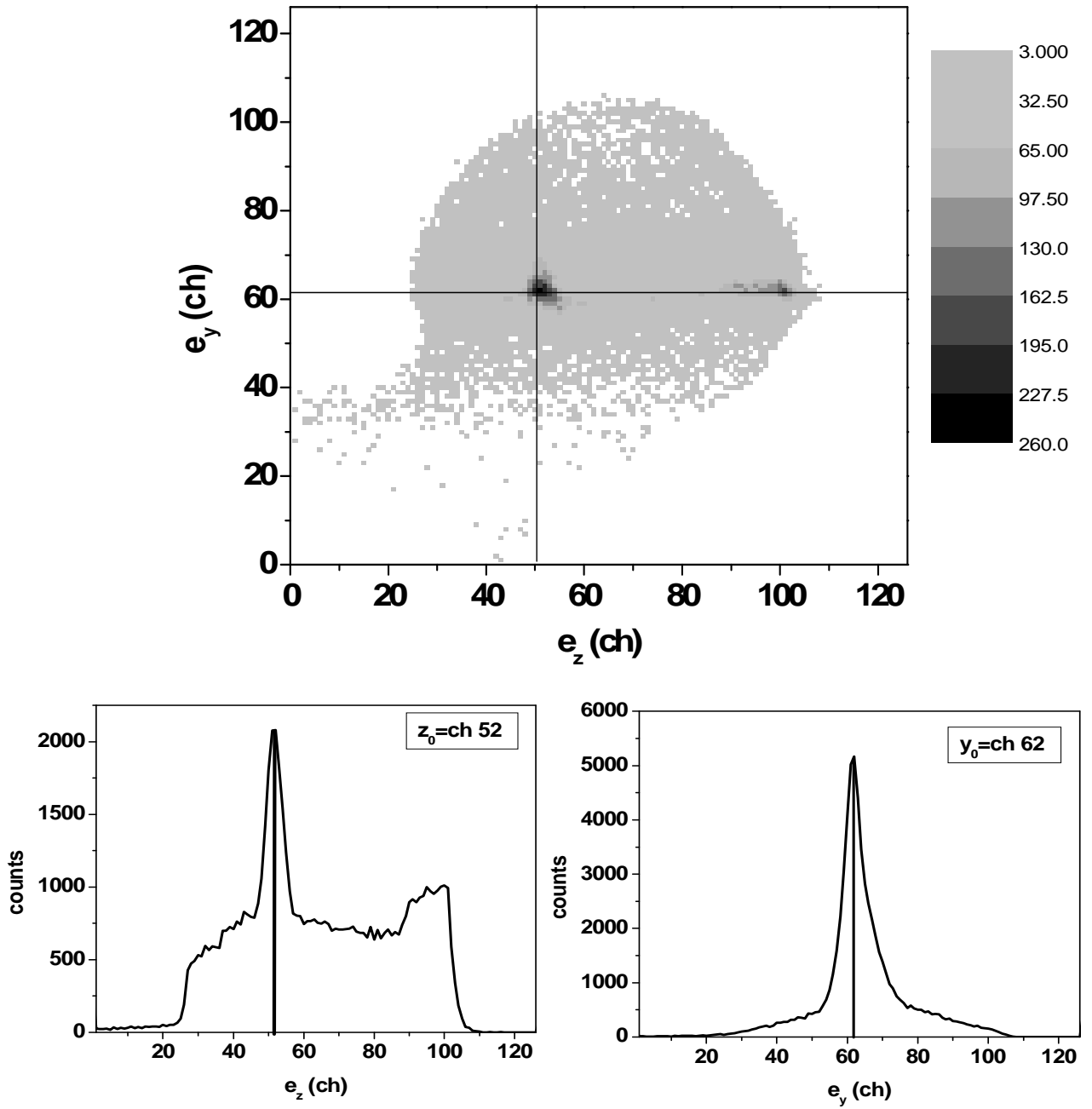


Figure 7.4: Recoil ions directed on to the electron detector. The center of the detector is observed at $(z, y) = (52, 62)$.

7.2 Results Of $H^+ + H$ Experiments

The experiments were done for proton impact energies of 15, 25 and 50 keV. With the choices of gates described in the previous part of this chapter, corresponding ejected electron velocity distributions projected onto the $x - z$ plane were extracted. These projections are given in Figure 7.5. Figures 7.6 and 7.7 are the projections of these data onto the longitudinal and transverse axes.

In the longitudinal direction, the progression of a saddle-centered distribution to a target-centered one is seen. In the transverse direction, only for the 15 keV case a slight preference opposite the recoil ion direction can be observed (the recoil ions are in the $+y$ direction). This is consistent with results of theoretical calculations [12, 13, 14]. Yet as the impact energy increases we do not see any direction preference nor any oscillations in the data. This result does not agree with the findings of [14] given in Figure 7.8. They observe a distinct asymmetry going from 15 keV to 25 keV. On the other hand results from [38] do not observe this asymmetry.

Along the jet direction the momentum resolution is about 2 a.u. which makes the selection of a scattering plane problematic. Note that in the top graph of Figure 7.3 the distribution is not circular, but instead stretched along the y direction. Since we have the capability to choose the transverse momentum window we might be able to see when the resolution starts to not play a role. Figure 7.9 gives examples of electron velocity distributions that correspond to various choices of transverse recoil momenta. Figures 7.10 and 7.11 are the projections of these spectra on to the longitudinal (beam direction) and transverse axes. After selecting various transverse momenta we still cannot tell exactly which way the recoil ion is moving due to the poor resolution along the y direction.

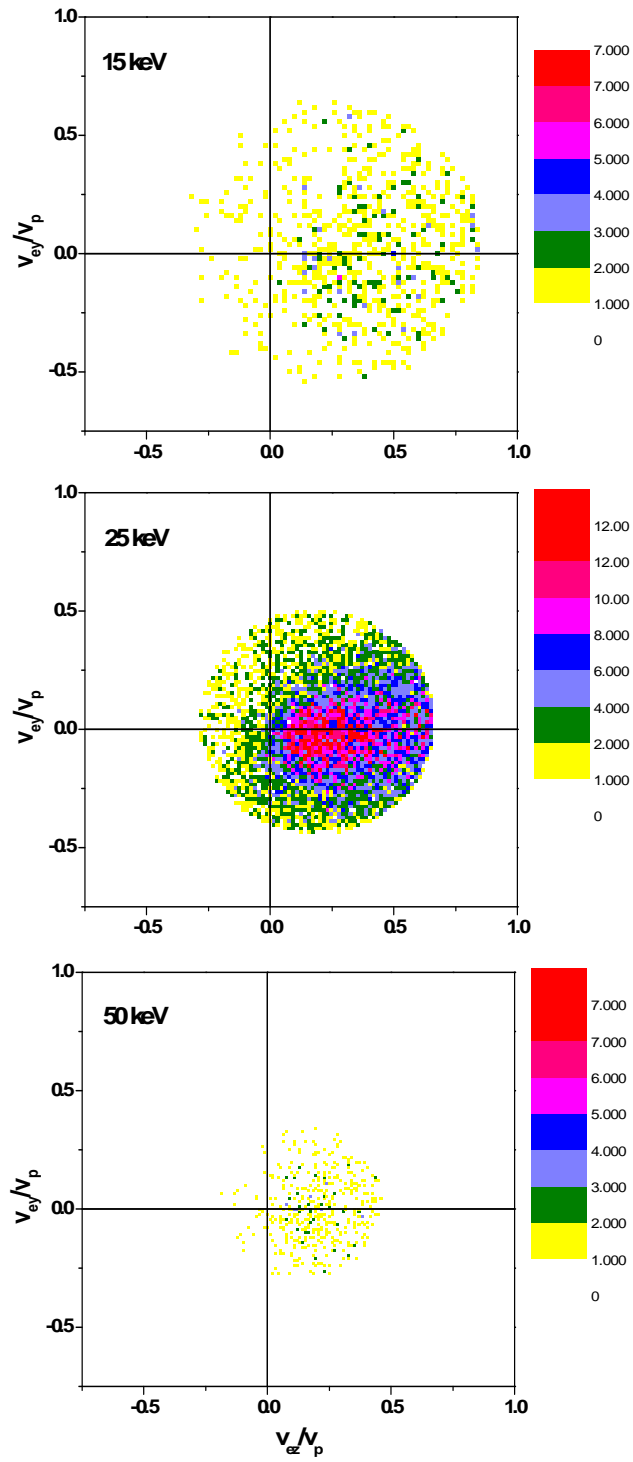


Figure 7.5: v_{ey}/v_p vs v_{ez}/v_p for proton impacts at 15, 25 and 50 keV.

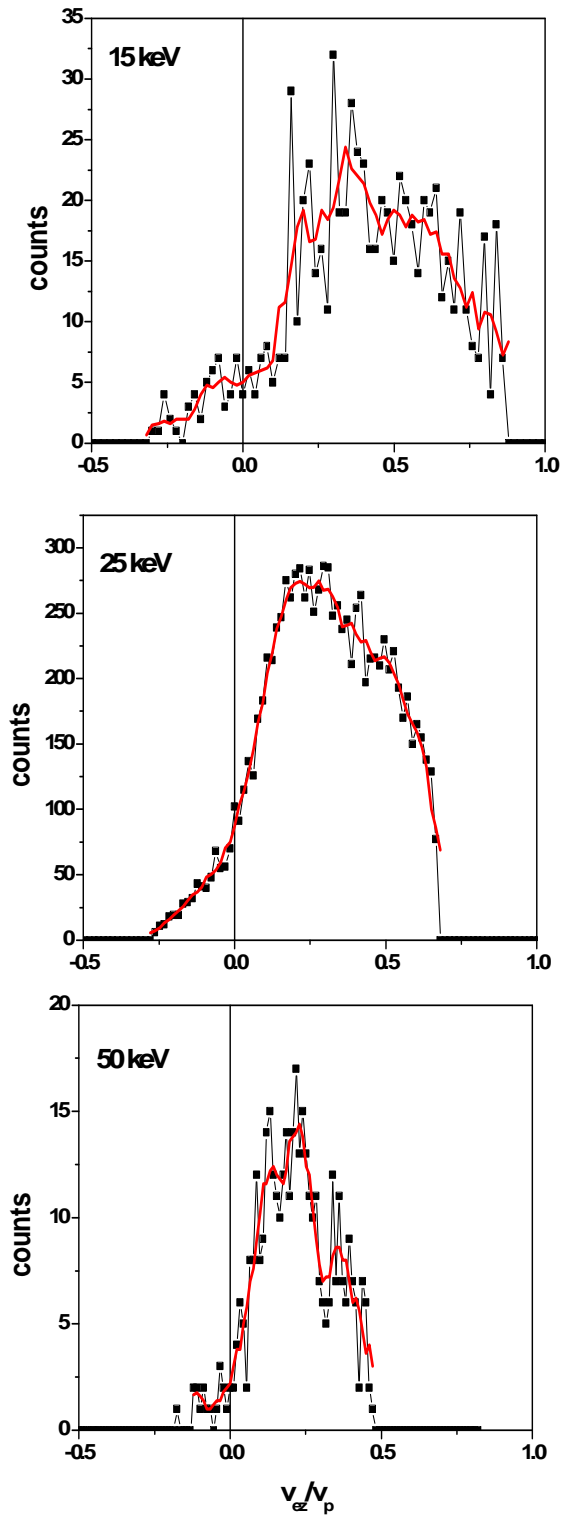


Figure 7.6: Projections of Figure 7.5 onto the longitudinal axis.

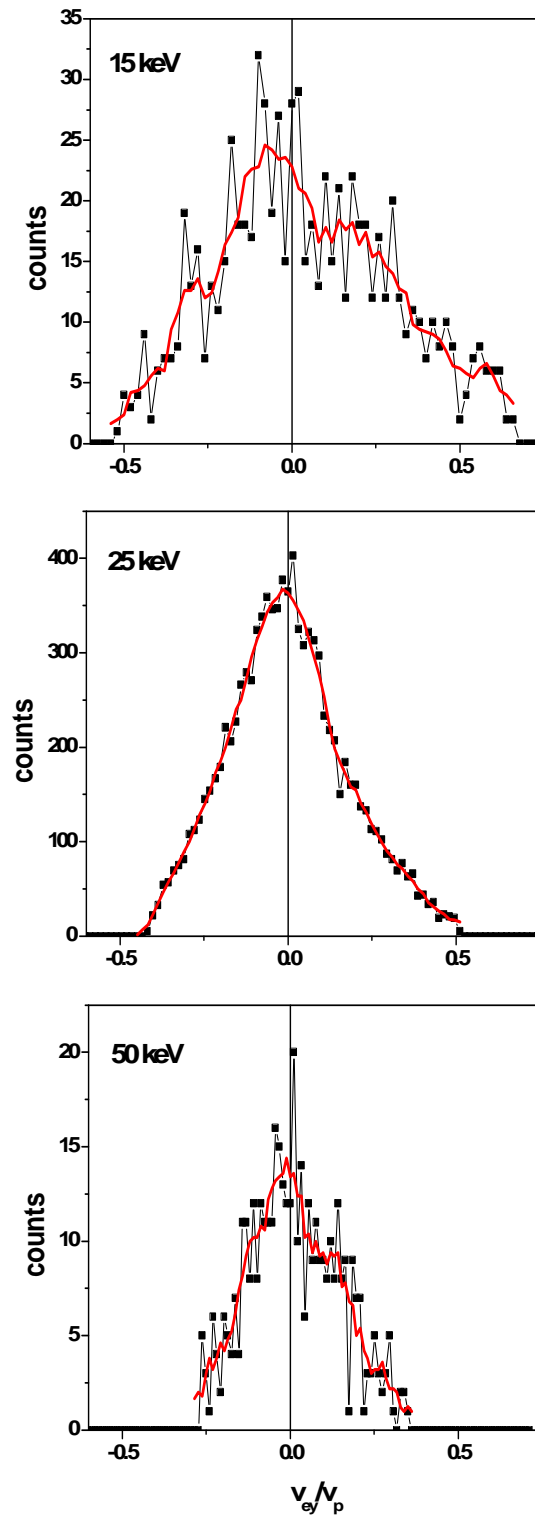


Figure 7.7: Projections of Figure 7.5 onto the transverse axis.

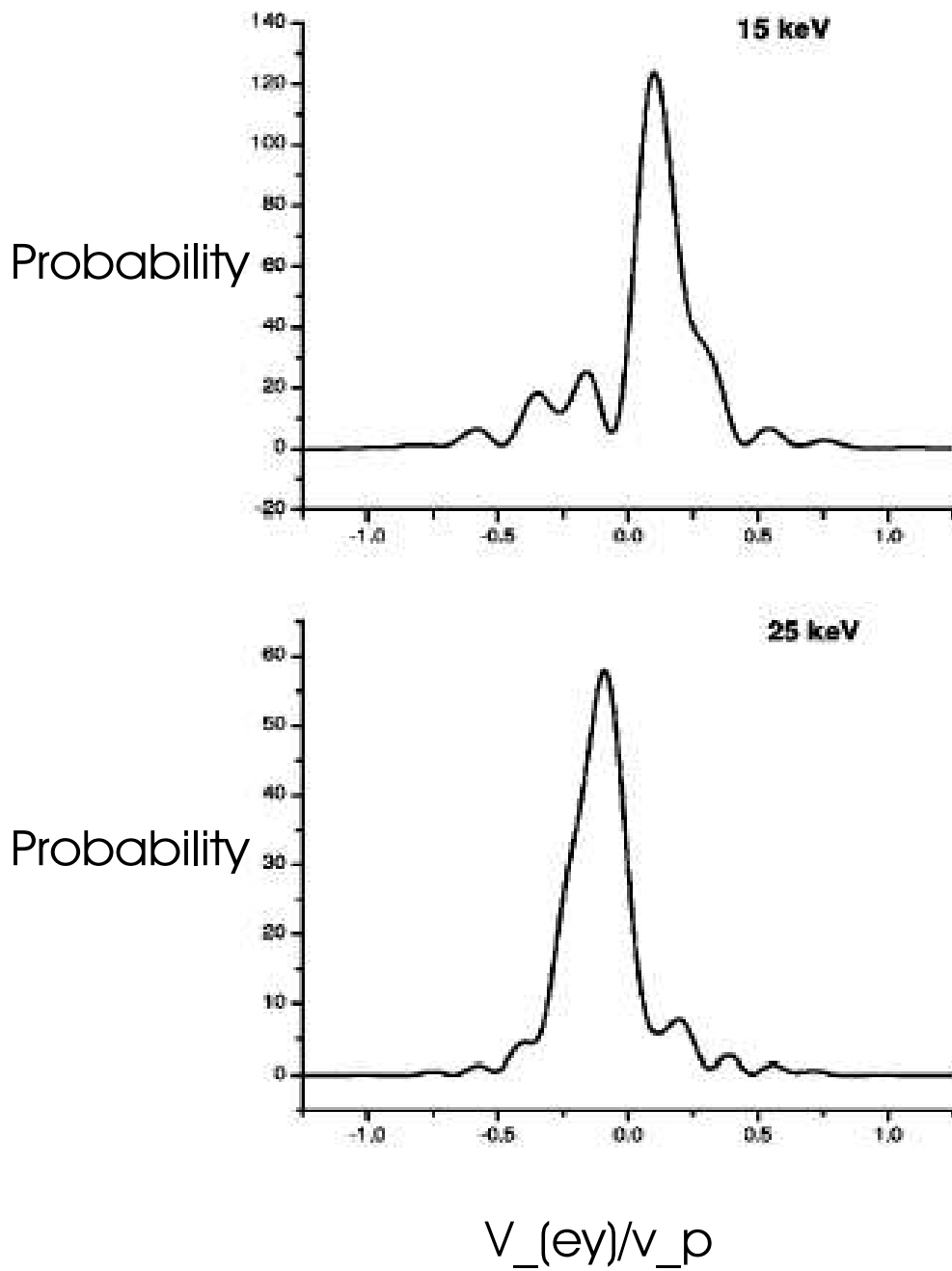


Figure 7.8: Results from [14] for 15 and 25 keV. These are calculated projections of electron velocity distributions on to the transverse axis. The recoil ions are moving along $-y$ direction.

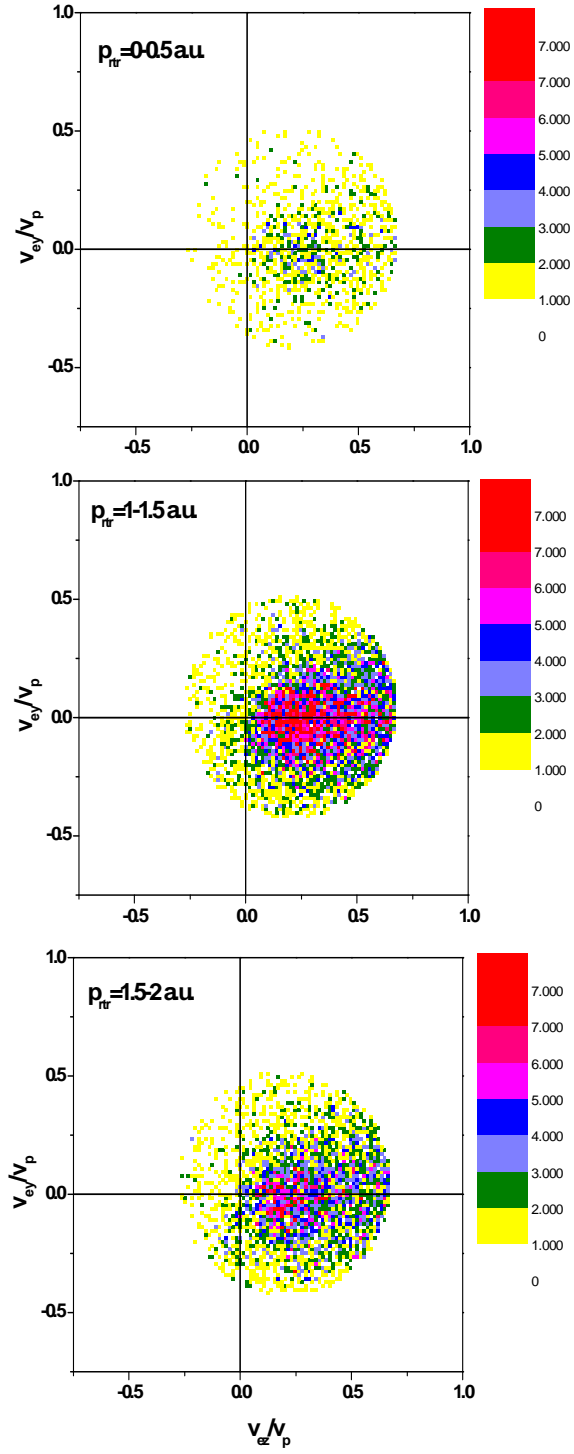


Figure 7.9: v_{ey}/v_p vs v_{ez}/v_p for 25 keV proton impact on H , showing different choices of the transverse momentum.

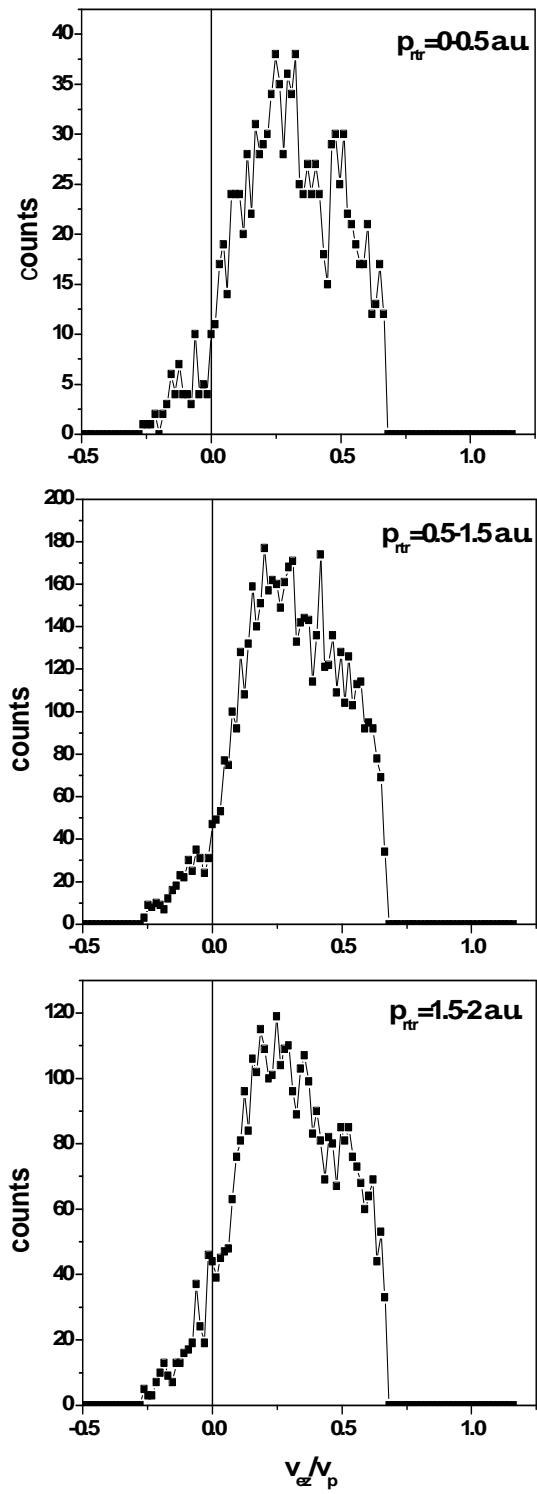


Figure 7.10: Projections of figure 7.9 on to the beam axis.

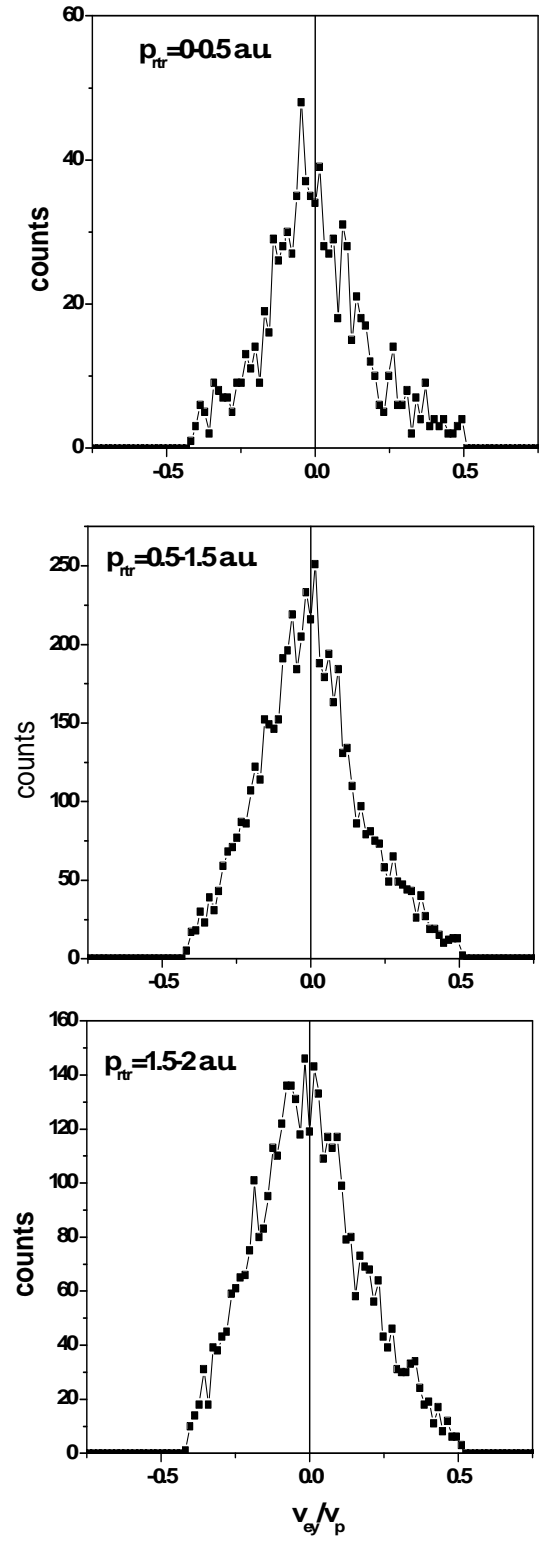


Figure 7.11: Projections of figure 7.9 transverse to the beam axis.

Chapter 8

Conclusions

Our goal in this work was to study ionization and capture processes involving atomic hydrogen, a true one-electron target. We started out with investigating the capture process for the cases of atomic and molecular hydrogen bombarded by Ar^{8+} . State-selective Q -values were measured for different energies. We observed that in the case of an atomic hydrogen target, higher angular momentum states of the projectile were occupied by the captured electron as the impact velocity was increased. This tendency was also seen in the model calculations by ???. However, contrary to predictions of existing close-coupling theories, we saw a large population of $n = 6$ states. This came as a surprise because the close-coupling theory does not predict this and it was believed that the close-coupling theory was mature in this area. Experimental results should have matched the theory exactly. Other experimental work that has been done to date appeared to agree with the theory. Yet none of these experiments were done using an atomic hydrogen target and thus non-rigorous one-electron models for the target had to be used. With the atomic hydrogen target, our results directly remove this uncertainty and the fact that they do not match exactly opens this subject for discussion.

For the case of ionization, proton impact on helium has been a frequent test case in

the literature due to the experimental simplicity of the target. This system had been studied in detail for low and high energies. We aimed to bridge the projectile energy gap between the non-perturbative ‘saddle-point’ region and the perturbative region and how the evolution from the low-energy picture to the high-energy one proceeds. We compared our results to the theoretical TCMSD method. The results for the longitudinal electron velocity distributions were expected since it is known that the distributions will become target-centered as the impact velocity increases. The transverse distributions we observed experimentally did not show the behavior predicted by the theory. We concluded that the major disagreement between theory and experiment can be attributed to a long-range transverse cooling of the electrons in the gradually disappearing saddle potential as the collision partners depart.

Our last experiment was the ionization of atomic hydrogen by proton impact. Our goal was to perform this experiment in the low-energy regime where one would expect to see a ‘finger’ structure in the electron velocity distributions which oscillates with changing impact velocity. We developed an atomic hydrogen source for these experiments. For these experiments we needed to know the transverse recoil ion momentum transfer. In particular the y component of $p_{r\perp}$ along the jet direction defines the direction of the recoil. The expected p_y distribution for ionization of an atomic hydrogen target by a 25 keV proton is about 2 a.u. while the momentum resolution we could obtain was also about 2 a.u. FWHM. This resulted in our not being able to resolve exactly the direction of the recoiling ion. At 5 keV the transverse momentum transfer is expected to go up to be substantially larger which would allow better definition of the recoil ion direction. The reason we did not measure for example a 5 keV collision is that the ionization cross-sections are very low in

this energy region. The low cross-section, thin target and weak proton beam current kept us from being able to achieve results in the energy region we wanted. However, we were able to get preliminary results in the intermediate energy range. This work thus represents only the beginning of a study of ionization in the one-electron H_2^+ system. The lower energy ranges could possibly be achieved with other ion sources that can provide the larger desired currents.

Chapter 9

Appendix

9.1 Electronics Setup

Block diagrams of experimental electronic setup are shown in figures 9.1 and 9.2. The position signals from the detectors were first amplified by CATSA preamplifiers and then sent to amplifiers for further amplification and shaping. Afterwards these position signals were sent to an analog-to-digital converter (ADC). The timing signals were taken from the back channel plates of the detectors and amplified by fast-timing-amplifiers (FTA) and timing-filter-amplifiers (TFA). Afterwards they were noise discriminated by constant-fraction-discriminators (CFD). Finally the timing signals were sent to the time-to-amplitude converters (TAC). For the case of capture experiments the start signal was provided by the projectiles while for the case of ionization experiments it was provided by the electron signal. In both cases the stop signal came from the recoils. the strobe signal was provided by the recoils that were valid stops.

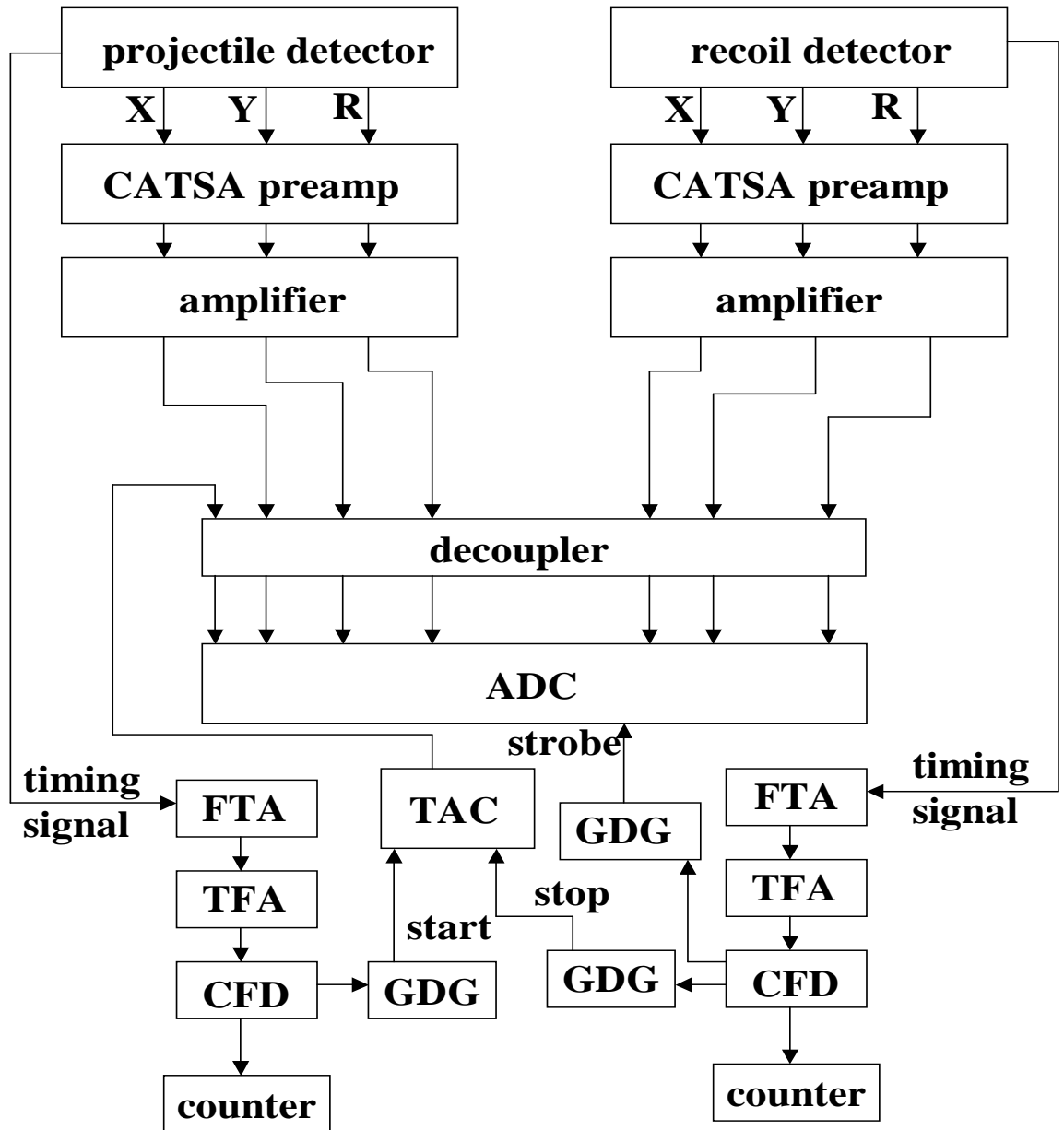


Figure 9.1: Block diagram of basic electronics for capture experiments. The abbreviations used are FTA: fast timing amplifier, TFA: timing filter amplifier, CFD: constant fraction discriminator, TAC: time-to-amplitude converter, GDG: Gate and delay generator, ADC: analog-to-digital converter.

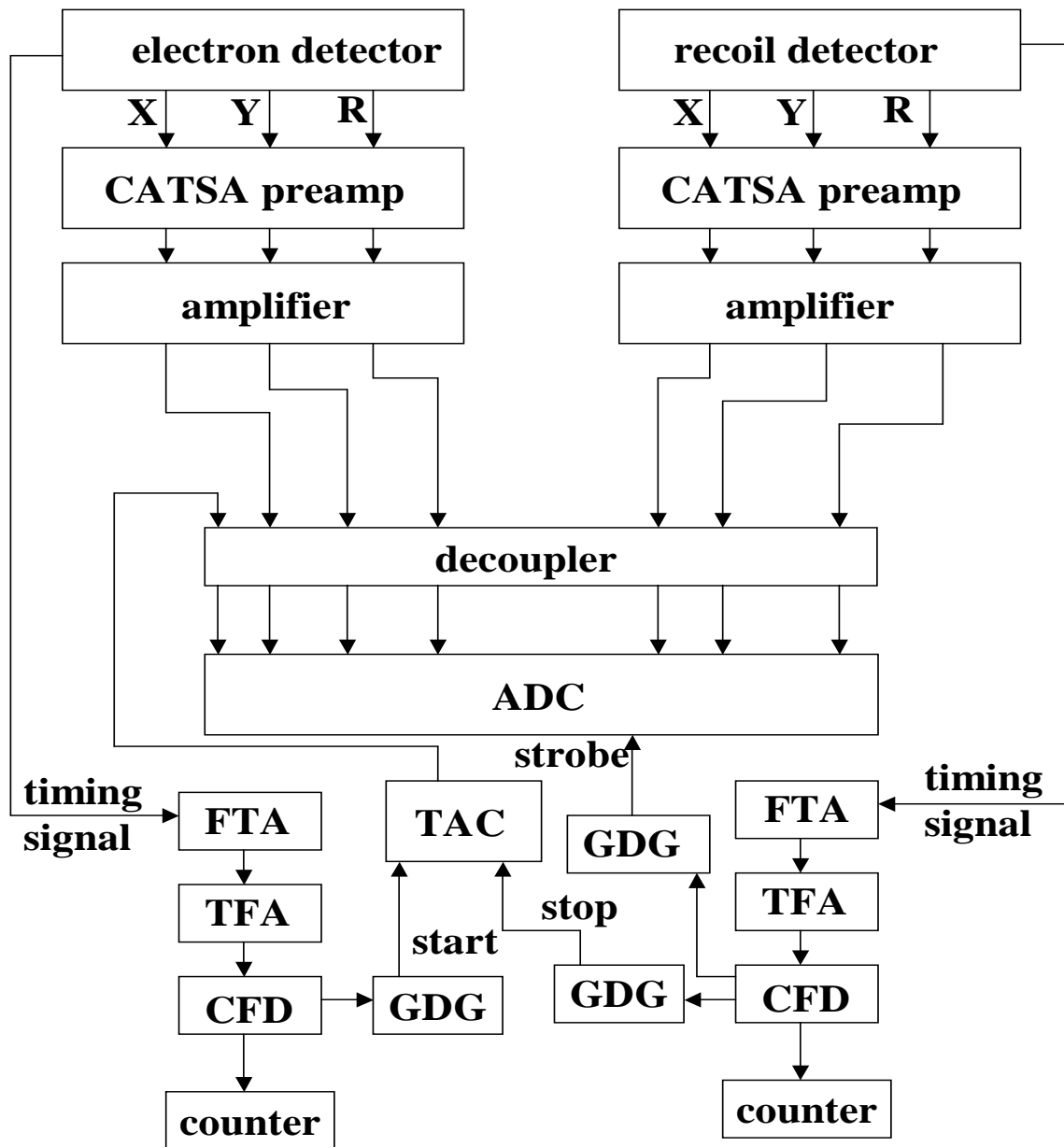


Figure 9.2: Block diagram of basic electronics for ionization experiments. The abbreviations used are FTA: fast timing amplifier, TFA: timing filter amplifier, CFD: constant fraction discriminator, TAC: time-to-amplitude converter, GDG: Gate and delay generator, ADC: analog-to-digital converter.

9.2 The Data Analysis Program For Capture Experiments

PONHE.EVL
EVL FILE FOR COINCIDENCE EXPERIMENTS INVOLVING JET
BY ERGE EDGU
February 07, 1999 (reduced from Mohammad's itcjet.evl)

PARAMETERS AND VARIABLES

```
REAL OFF=12
REAL RIZLO=10
REAL RIZHI=2049
real epzy=40
!
!-----REC. DET.-----
!
REAL RTHS=200
real rthsm=20
REAL RTHH=2049
REAL RCH=250
REAL RAMPZ=1
REAL RAMPY=1
REAL RZSH=0
REAL RYSH=0
REAL RFACTOR=1.5
REAL SRZF
REAL SRYF
REAL SRRF
REAL RV1
REAL RV2
REAL RV3
REAL RS
INTEGER RIZ
INTEGER RIY
INTEGER RIZIY
integer rizl
integer riyl
integer riziyl
!
!-----spectra enlargement-----
!
integer rizm
integer riyM
real stacer5i
real tacerc=256.0
real taccon=1.0
real ryc=70.0
real rycon=4.0
real rzc=70.0
real rzcon=1.0
integer zeone
integer iseed=439787
real temp1
integer testm
integer testmm
real riytemp
real pyitemp
real riztemp
integer pzitemp
integer pZr
integer pyr
integer tacerr
integer ptransr
real pzreal
real pyreal
real tacreal
real tanphi
real xm256
real phi
real aang=0.0
real bang=1.0e9
real cang=0.0
real dang=1.0e9
real tacbgc=256.0
real tacbgcon=1.0
integer stacer5g
real tbg
real 2dpnorm=1.0
real tbgnorm
integer tacsuB
real tacsuBr
real tbgr
real eiztemp
integer eizm
real ezc=256.0
real ezcon=1.0
real ezreal
integer ezitemp
integer rzmeZ
```

```

!
!-----ELEC. DET.-----
!
REAL ETHS=-100
real ethss=0
real ethsm=20
REAL ETHH=2046
REAL ECH=250
REAL EAMPZ=1
REAL EAMPY=1
REAL EZSH=0
REAL EYSH=0
REAL EFACTOR=1.5
REAL SEZF
REAL SEYF
REAL SERF
REAL EV1
REAL EV2
REAL EV3
REAL ES
INTEGER EIZ
INTEGER EIY
INTEGER EIZIY
!
!-----VARIABLES FOR ROTATIONS----- !
!-----REC. DET.-----

REAL RT=0 !ANGLE OF ROTATION FOR REC. DET.
REAL SINRT
REAL COSRT
REAL X1SINRT
REAL X1COSRT
REAL RZ0=65
REAL RY0=65
REAL RZ1
REAL RY1
REAL RZ2
REAL RY2
REAL RZ3
REAL RY3
!-----ELEC. DET.-----
REAL ET=6.195919 !ANGLE OF ROTATION FOR ELEC. DET.
REAL SINET
REAL COSET
REAL X1SINET
REAL X1COSE
REAL EZ0=65
REAL EY0=65
REAL EZ1
REAL EY1
REAL EZ2
REAL EY2
REAL EZ3
REAL EY3
real esnn
!-----TAC-----
REAL TACERL=-100
REAL TACERH=2048
!
!-----GENERAL PURPOSE PARAMETERS-----
REAL ZERO=0.0
REAL ONETHIRD=0.33333333
REAL FOUR=4
REAL THREE=3
REAL EIGHT=8
real one=1.0
REAL OTH=130
!
!-----transverse momentum-----
real rycal=1.0
real rzcal=1.0
real rzg0=260.0
real ryg0=260.0
!
! ===== SORTING =====
OPTION ALLSPEC
option tape

FORMAT SRZ 1 12 1
FORMAT SRY 2 12 1
FORMAT SRR 3 12 1
FORMAT STACER 4 12 1 ! TACER
! FORMAT STACER2 4 12 5 ! TACER/8
format stacer5 4 12 3 !tacer/4
FORMAT SEZ 5 12 1
FORMAT STACEP 5 12 1 ! TACEP
FORMAT STACEP2 5 12 5 ! TACEP/8
FORMAT SEY 6 12 1
FORMAT SER 7 12 1

EVENT 2
IF STACER GT TACERH EXIT
IF STACER LT TACERL EXIT
IF SRZ GT RTHH EXIT

```

```

IF SRY GT RTHH EXIT
IF SRR GT RTHH EXIT
IF SEZ GT ETHH EXIT
IF SEY GT ETHH EXIT
IF SER GT ETHH EXIT
IF SRZ LT RTHS EXIT
IF SRY LT RTHS EXIT
IF SRR LT RTHS EXIT
IF SEZ LT ETHS EXIT
IF SEY LT ETHS EXIT
IF SER LT ETHS EXIT

```

tape

!=====CORRECTION FOR GAINS AND OFFSETS=====

!!

!-----REC. DET.-----

```

GET SRZ
SUB OFF
STA SRZF
STA RV1
GET SRY
SUB OFF
STA SRYF
STA RV2
GET SRR
SUB OFF
STA SRRF
STA RV3

```

!-----ELEC. DET.-----

```

GET SEZ
SUB OFF
STA SEZF
STA EV1
GET SEY
SUB OFF
STA SEYF
STA EV2
GET SER
SUB OFF
STA SERF
STA EV3

```

!

!=====DIVISIONS=====

!-----REC. DET.-----

```

LDA RV3
MUL RFACTOR
ADD RV1
ADD RV2
STA RS
div 3.
sta rsn
if rs eq 0 exit
IF RSN LT RTHS EXIT
LDA RV1
MUL RCH
DIV RS
MUL RAMPZ
SUB RZSH
STA RIZ7
FIX
STA RIZ
lda riz7
mul 16.0
fix
sta rizl
LDA RV2
MUL RCH
DIV RS
MUL RAMPY
SUB RYSH
STA RIY7
FIX
STA RIY
lda riy7
mul 16.0
fix
sta riyl

```

!

!-----ELEC. DET.-----

!

```

LDA EV3
MUL EFACTOR
ADD EV1
ADD EV2
STA ES
div 3.0
sta esnn
if es eq 0 exit
IF ES LT ETHSs EXIT
LDA EV1
MUL ECH
DIV ES
MUL EAMPZ
SUB EZSH

```

```

mul -1.0
add 130.0
STA EIZ7
FIX
STA EIZ
LDA EV2
MUL ECH
DIV ES
MUL EAMPY
SUB EYSH
STA EIY7
FIX
STA EIY
!
!=====DETECTORS ROTATIONS===== !
!-----REC. DET.-----
LDA RIZ7
SUB RZ0
STA RZ1
LDA RIY7
SUB RY0
STA RY1
LDA RT
SIN
STA SINRT
LDA RT
COS
STA COSRT
LDA RZ1
MUL COSRT
STA X1COSRT
LDA RY1
MUL SINRT
ADD X1COSRT
STA RZ2
LDA RZ1
MUL SINRT
STA X1SINRT
LDA RY1
MUL COSRT
SUB X1SINRT
STA RY2
LDA RZ2
ADD RZ0
STA RZ3
FIX
STA RIZ
LDA RY2
ADD RY0
STA RY3
FIX
STA RIY
!
!-----ELEC. DET.-----
!
LDA EIZ7
SUB EZ0
STA EZ1
LDA EIY7
SUB EY0
STA EY1
LDA ET
SIN
STA SINET
LDA ET
COS
STA COSET
LDA EZ1
MUL COSET
STA X1COSET
LDA EY1
MUL SINET
ADD X1COSET
STA EZ2
LDA EZ1
MUL SINET
STA X1SINET
LDA EY1
MUL COSET
SUB X1SINET
STA EY2
LDA EZ2
ADD EZ0
STA EZ3
FIX
STA EIZ
LDA EY2
ADD EY0
STA EY3
FIX
STA EIY
!
!=====SPECTRA INCREMENTS===== !

```

```

!-----TACS-----
TINC STACER TACER
sta stacer
!
!-----REC.-----
TINC SRZF ZR
TINC SRYF YR
TINC SRRF RR
TINC RSN SUMR
TINC RIZ RIY RZY
STA RIZIY
TINC RIZ RZZ
TINC RIY RYY
tinc rizl rzl
! sta srzl
! if rizl lt rizlo exit
! if rizl gt rizhi exit
tinc riyl ryl
tinc rizl riyl rzyl
!
!-----ELEC.-----
TINC SEZF ZE
TINC SEYF YE
TINC SERF RE
TINC ESnn SUME
TINC EIZ EIY EZY
STA EIZIY
TINC EIZ EZZ
TINC EIY EYY

!-----electron det. shrink-----
lda eiz
sub 65
mul
sta eizz2

lda eiy
sub 65
mul
add eizz2
sqrt
sta temp1
ran iseed
sub 0.500
add temp1
sta temp1
sta eip
fix
sta eipzy

if eipzy gt epzy exit

!=====GATES=====
SPEC TACER
GATE G1 TACER 1
GATE G2 TACER 2
GATE G3 TACER 3

tinc stacer5 tacer5
! if rizi9 q9 then
! if stacer g2 then
! tinc eiziy ezyb
! sta sezyb
! endif
! if stacer g1 then
! tinc eiziy ezyg
! sta sezyg
! endif

if rizi9 q9 then
tinc stacer tacerg
sta tacerg
endif
spec tacerg
gate g4 tacerg 4
if stacer g1 then
tinc rizi9 rzyg
endif

! endif
!
!-----enlarged spectra-----
get stacer5
sta temp1
ran iseed
sub 0.500
add temp1
sta temp1
sub tacbgc
mul tacbgcon
add 256.0
sta tbg
fix
sta stacer5g

```

```

get stacer5
sta temp1
ran iseed
sub 0.500
add temp1
sta temp1
sub tacerc
mul taccon
add 256.0
fix
sta testm
if testm lt 1 exit
if testm gt 511 exit
if rizl lt rizlo exit
if rizl gt rizhi exit
get stacer
div 4.0
sta temp1
ran iseed
sub 0.500
add temp1
sta temp1
sub tacerc
mul taccon
add 256.0
sta tacreal
fix
sta stacer5i
!
lda riy7
sta temp1
ran iseed
sub 0.500
add temp1
sta temp1
mul 4.0
sta riytemp
fix
sta pyitemp
!
lda riytemp
sub ryc
mul rycon
add 256.0
sta pyreal
fix
sta riy
lda riz7
mul 4.0
sta riztemp
fix
sta rizm
lda riztemp
sub rzc
mul rzcon
add 256.0
sta pzreal
fix
sta pzitemp
lda eiz7
mul 4.0
sta eiztemp
fix
sta eizm
lda eiztemp
sub ezc
mul ezcon
add 256.0
sta ezreal
fix
sta ezitemp
lda pzreal
add ezreal
sub 256.0
fix
sta rzm
tinc tacreal tacer5m
tinc riy pY5m
tinc tacreal riy 2dpxpyg
sta 2dpxpyst
tinc pzitemp pz5m
!
!-----constructing transverse mom. distribution-----
lda stacer5i
sub 256.0
mul
sta ripx2
lda riy
sub 256.0
mul
add ripx2
sqrt
sta temp1
ran iseed

```

```

sub 0.500
add temp1
sta temp1
sta rip
fix
sta ripxy
tinc ripxy ptrans
tinc pzitemp ripxy ptl
!
!-----reduced spectra-----
lda pzreal
div 4.0
fix
sta pzr
lda pyreal
div 4.0
fix
sta pyr
lda tacrealm
div 4.0
fix
sta tacerr
lda rip
div 4.0
fix
sta ptransr
lda tbg
div 4.0
fix
sta tbgr
tinc pzr ptransr ptll
tinc eiz ripxy ezptrans
tinc eiz pzr ezipm
tinc eiz rmez ezipm
!
!-----
!----- PTRANSVERSE BY CHOICE OF ANGLE -----
lda ripxy
sta rip
! if rip gt 150.0 exit
if rip eq 0.0 exit
lda stacer5i
sub 256.0
sta temp1
ran iseed
sub 0.500
add temp1
sta temp1
sta xm256
fix
sta xmm
lda riym
sub 256.0
sta temp1
ran iseed
sub 0.500
add temp1
sta temp1
sta ym256
fix
sta ymm
if ym256 gt 0.0 then
if xm256 lt 0.0 then
lda ym256
div xm256
atan
div 3.141592654
mul 180.0
add 180.0
sta phitwo
sta temp1
ran iseed
sub 0.500
add temp1
sta temp1
fix
sta phip
tinc rip phip ptphi
sta sptphi
endif
endif
if ym256 lt 0.0 then
if xm256 gt 0.0 then
lda ym256
div xm256
atan
div 3.141592654
mul 180.0
add 360.0
sta phitree
sta temp1
ran iseed
sub 0.500

```

```

add temp1
sta temp1
fix
sta phip
tinc rip phip ptphi
sta sptphi
endif
endif
if ym256 lt 0.0 then
if xm256 lt 0.0 then
lda ym256
div xm256
atan
div 3.141592654
mul 180.0
add 180.0
sta phifour
sta temp1
ran iseed
sub 0.500
add temp1
sta temp1
fix
sta phip
tinc rip phip ptphi
sta sptphi
endif
endif
if ym256 gt 0.0 then
if xm256 gt 0.0 then
lda ym256
div xm256
atan
div 3.141592654
mul 180.0
sta temp1
ran iseed
sub 0.500
add temp1
sta temp1
sta phione
fix
sta phip
tinc rip phip ptphi
sta sptphi
endif
endif
if sptphi q1 then
tinc stacer5i riym rxyq1
endif
if sptphi q2 then
tinc stacer5i riym rxyq2
endif
if sptphi q3 then
tinc stacer5i riym rxyq3
endif
if sptphi q4 then
tinc stacer5i riym rxyq4
endif
!

if sptphi q1 then
! if srzl g1 then
! if eiziy q10 then
! if rizi y q9 then
! if stacerg g1 !if stacer g1 then
tinc eiziy ezyg
! tinc sezyg ezyq9q1
endif
if sptphi q2 then
tinc eiziy ezyb
! tinc sezyb ezyq9q2
! endif
! tinc riz riy rzyg1
endif
! endif
! endif
! if sptphi q2 then
! if eiziy q10 then
! if rizi y q9 then
! if stacerg g2
! tinc riz riy rzyg2
! endif
! endif
! endif
! if sptphi q3 then
! if eiziy q10 then
! if stacerg g3
! tinc eiz eiy ezyq9q3
! tinc riz riy rzyg3
! endif
! endif
! endif

```

```
    if sptphi q4 then
tinc eiz eiy ezyq9q4
endif
END
```

9.3 The Data Analysis Program For Ionization Experiments

arcptr.EVL
EVL FILE FOR COINCIDENCE EXPERIMENTS INVOLVING ATOMIC HYDROGEN TARGET
BY Erge Edgu-Fry and Jeff Stuhlman
July 28, 2002; November 25, 2002; December 5 2002;

RECOIL-PROJECTILE DETECTOR PARAMETERS AND VARIABLES

```
REAL OFF=12
REAL RIZLO=10
REAL RIZHI=2049
!
!----- REC. DET. -----
!
REAL RTHS=200
real rthsm=10
REAL RTHH=2049
REAL RCH=250
REAL RAMPZ=1
REAL RAMPY=1
REAL RZSH=0
REAL RYSH=0
REAL RFACTOR=1.5
REAL SRZF
REAL SRYF
REAL SRRF
REAL RV1
REAL RV2
REAL RV3
REAL RS
INTEGER RIZ
INTEGER RIY
INTEGER RIZIY
integer rizl
integer riyl
integer riziyl
!
!-----spectra enlargement-----
!
integer rizm
integer riy
integer riy2
integer stacpr5i
real tacprc=256.0
real taccon=1.0
real ryc=70.0
real rycon=4.0
real rzc=70.0
real rzcon=1.0
integer zeone
integer iseed=439787
real temp1
integer testm
integer testmm
real riytemp
real pyitemp
real riztemp
integer pzitemp
integer pzitemp2
integer pzi

integer pyr
integer tacpr
integer ptransr
real pzreal
real pyreal
real tacreal
real tacbgc=256.0
real tacbgcon=1.0
integer stacer5g
real tbg
real 2dpnorm=1.0
real tbgnorm
integer tacsu
real tacsu
real tbgr
! real pzitemp
integer eizm
real ezc=256.0
real ezcon=1.0
real ezreal
integer ezitemp
integer rzmez
!
!-----Proj. DET. -----
!
REAL PTHS=-100
REAL PTHH=2046
```

```

REAL PCH=250
REAL PAMPZ=1
REAL PAMPY=1
REAL PZSH=0
REAL PYSH=0
REAL PFACTOR=1.5
REAL SPZF
REAL SPYF
REAL SPRF
REAL PV1
REAL PV2
REAL PV3
REAL PS
INTEGER PIZ
INTEGER PIY
INTEGER PIZIY
!
!-----VARIABLES FOR ROTATIONS-----
!
!-----REC. DET. -----
!
REAL RT=0 !ANGLE OF ROTATION FOR REC. DET.
REAL SINRT
REAL COSRT
REAL X1SINRT
REAL X1COSRT
REAL RZ0=65
REAL RY0=65
REAL RZ1
REAL RY1
REAL RZ2
REAL RY2
REAL RZ3
REAL RY3
!
!-----Proj. DET.-----
!
REAL PT=6.195919 !ANGLE OF ROTATION FOR Proj. DET.
REAL SINPT
REAL COSPT
REAL X1SINPT
REAL X1COSP
REAL PZ0=65
REAL PY0=65
REAL PZ1
REAL PY1
REAL PZ2
REAL PY2
REAL PZ3
REAL PY3
real psnn
!
!-----TAC-----
!
REAL TACPRL=-100
REAL TACPRH=2048
!
! - - - - Source Ratio Variables - - - - -
!
Real Bgdr !Events that are not H or H2
Real HA !Events that are H
Real HM !Events that are H2
Integer TmpCount !Temporary Event count
Real EventCt !Number of events
Integer Count !Events divided by IncSize
Integer IncSize=5000 !Number of events before the ratios
!are calculated
Real HADHM !H to H2 Ratio
Integer IHADHM !Percent H to H2
Real BgdrDEvt !Background to event ratio
Integer HAHMThr=20 !H to H2 Percent Threshold
Integer DoThrInc=1 !If not 1 the Thr inc cond is skipped

      Real OrderOne !For the ratio to present
Real OrderTwo !calculation
Real OrdThree
Real OrdFour
!
!-----Cordinate Transformation Variables-----
!
Real Thetatmp !Retuned From CordTrans subr
Real Radtmp

Real Ycntr !detector space center
Real Zcntr
Real Xcntr

Integer ITyz
Integer IRPyPz

Integer ITyx
Integer IRPyPx

! Image subr !Gets the subroutine going

```

```

!
!
!-----GENERAL PURPOSE PARAMETERS-----
!
REAL ZERO=0.0
REAL ONETHIRD=0.33333333
REAL FOUR=4
REAL THREE=3
REAL EIGHT=8
real one=1.0
REAL OTH=130
Integer Ione=1
Integer Izero=0
!
!-----transverse momentum-----
!
real rycal=1.0
real rzcal=1.0
real rzg0=260.0
real ryg0=260.0
!
!===== SORTING=====
!
OPTION ALLSPEC
option tape
!
!
FORMAT SRZ 1 12 1
FORMAT SRY 2 12 1
FORMAT SRR 3 12 1
FORMAT STACPR 4 12 1 ! TACPR
! FORMAT STACPR2 4 12 5 ! TACPR/8
format stacpr5 4 12 3 !tacpr/4
FORMAT SPZ 5 12 1
FORMAT SPY 6 12 1
FORMAT SPR 7 12 1
!
!
EVENT 2
IF STACPR GT TACPRH EXIT
IF STACPR LT TACPRL EXIT
IF SRZ GT RTHH EXIT
IF SRY GT RTHH EXIT
IF SRR GT RTHH EXIT
IF SPZ GT PTHH EXIT
IF SPY GT PTHH EXIT
IF SPR GT PTHH EXIT
IF SRZ LT RTHS EXIT
IF SRY LT RTHS EXIT
IF SRR LT RTHS EXIT
IF SPZ LT PTHS EXIT
IF SPY LT PTHS EXIT
IF SPR LT PTHS EXIT

tape
!=====CORRECTION FOR GAINS AND OFFSETS=====
!
!
!-----REC. DET.-----
!
GET SRZ
SUB OFF
STA SRZF
STA RV1
GET SRY
SUB OFF
STA SRYF
STA RV2
GET SRR
SUB OFF
STA SRRF
STA RV3
!
!-----Proj. DET.-----
!
GET SPZ
SUB OFF
STA SPZF
STA PV1
GET SPY
SUB OFF
STA SPYF
STA PV2
GET SPR
SUB OFF
STA SPRF
STA PV3
!
!=====DIVISIONS=====
!
!-----REC. DET.-----
!
LDA RV3
MUL RFACTOR

```

```

ADD RV1
ADD RV2
STA RS
div 3.
sta rsn
if rs eq 0 exit
IF RSN LT RTHSm EXIT
LDA RV1
MUL RCH
DIV RS
MUL RAMPZ
SUB RZSH
STA RIZ7
FIX
STA RIZ

    LDA RV2
MUL RCH
DIV RS
MUL RAMPY
SUB RYSH
STA RIY7
FIX
STA RIY
!
!-----Proj. DET.----- !
LDA PV3
MUL PFACTOR
ADD PV1
ADD PV2
STA PS
div 3.0
sta psnn
! if ps eq 0 exit
IF PS LT PTHS EXIT
LDA PV1
MUL PCH
DIV PS
MUL PAMPZ
SUB PZSH
mul -1.0
add 130.0
STA PIZ7
FIX
STA PIZ
LDA PV2
MUL PCH
DIV PS
MUL PAMPY
SUB PYSH
STA PIY7
FIX
STA PIY
!
!=====DETECTORS ROTATIONS===== !
!-----REC. DET.-----
!
LDA RIZ7
SUB RZ0
STA RZ1
LDA RIY7
SUB RY0
STA RY1
LDA RT
SIN
STA SINRT
LDA RT
COS
STA COSRT
LDA RZ1
MUL COSRT
STA X1COSRT
LDA RY1
MUL SINRT
ADD X1COSRT
STA RZ2
LDA RZ1
MUL SINRT
STA X1SINRT
LDA RY1
MUL COSRT
SUB X1SINRT
STA RY2
LDA RZ2
ADD RZ0
STA RZ3
FIX
STA RIZ

lda rz3
mul 16.0
fix
sta rizl
div 4.0

```

```

fix
sta rizll
LDA RY2
ADD RY0
STA RY3
FIX
STA RIY
lda ry3
mul 16.0
fix
sta riyl
div 4.0
fix
sta riyll
!
!-----Proj. DET.-----
!
LDA PIZ7
SUB PZ0
STA PZ1
LDA PIY7
SUB PY0
STA PY1
LDA PT
SIN
STA SINPT
LDA PT
COS
STA COSPT
LDA PZ1
MUL COSPT
STA X1COSPT
LDA PY1
MUL SINPT
ADD X1COSPT
STA PZ2
LDA PZ1
MUL SINPT
STA X1SINPT
LDA PY1
MUL COSPT
SUB X1SINPT
STA PY2
LDA PZ2
ADD PZ0
STA PZ3
FIX
STA PIZ
LDA PY2
ADD PY0
STA PY3
FIX
STA PIY
!
!=====enlarged spectra=====
!
get stacpr5
sta temp1
ran iseed
sub 0.500
add temp1
sta temp1
sub tacbgc
mul tacbgcon
add 256.0
sta tbg
fix
sta stacpr5g
get stacpr5
sta temp1
ran iseed
sub 0.500
add temp1
sta temp1
sub tacprc
mul taccon
add 256.0
fix
sta testm
! if testm lt 1 exit
! if testm gt 511 exit
get stacpr5
sta temp1
ran iseed
sub 0.500
add temp1
sta temp1
sub tacprc
mul taccon
add 256.0
sta tacreal
fix
sta stacpr5i
lda riyll

```

```

sta temp1
ran iseed
sub 0.500
add temp1
sta temp1
! mul 4.0
sta riytemp
fix
sta pyitemp

lda riytemp
sub ryc
mul rycon
add 256.0
sta pyreal
fix
sta riym
lda rizll
! mul 4.0
sta riztemp
fix
sta rizm
lda riztemp
sta temp1
ran iseed
sub 0.500
add temp1
sta temp1
sub rzc
mul rzcon
add 256.0
sta pzreal
fix
sta pzitemp

!!===trans momentum===
lda stacpr5i
sub 256.0
mul
sta ripx2
lda riym
sub 256.0
mul
add ripx2
sqrt
sta temp1
ran iseed
sub 0.500
add temp1
sta temp1
sta rip
fix
sta ripxy
!
!-----Cord Trans-----
!The fortran file subr.for needs to be compiled once
!Use the xsys command USHAREBLD subr.for

! Call CordTrans(Thetatmp,Radtmp,RY3,RZ3,Ycntr,Zcntr)
Real Ytmp
Real Xtmp
Real Rtmp
Real X2tmp
Real Y2tmp
Real Xor

LDA stacpr5i
sub 256
STA Xtmp
LDA Xtmp
Mul
STA X2tmp

LDA riym
sub 256
STA Ytmp
LDA Ytmp
Mul
STA Y2tmp

LDA Y2tmp
Add X2tmp
sqrt
STA Radtmp

LDA Xtmp
DIV Radtmp
STA Xor
if Ytmp LT Zero
LDA Xor
Mul -1
acos
add 3.142
STA Thetatmp

```

```

else
LDA Xor
acos
STA Thetatmp
Endif
// LDA Thetatmp
Mul 57.296
Fix
STA IThyX
LDA Radtmp
Fix
STA IRPyPX
! Tinc IRPyPX IThyx RyxTh
! Sta srxyth
!
!
!=====SPECTRA INCREMENTS===== !
!-----TACS-----

TINC STACPR TACPR
spec tacpr
gate g1 tacpr 1
!
!-----REC.-----
!
TINC SRZF ZR
TINC SRYF YR
TINC SRRF RR
TINC RSN SUMR
TINC RIZ RIY RZY
STA RIZIY

if stacpr g1 then
tinc riz riy rzyg
tinc rizl rzl
endif
TINC RIZ RZZ
TINC RIY RYY

! tinc rizl rzl
tinc riyl ryl

if riziyl q9 then
tinc stacpr tacprg
tinc stacpr5i riym 2dpxpyg
sta spxpy
tinc stacpr5g riym 2dpxpyb
sta spxpyb

tinc pzitemp riym PrzPry
sta riziyl

if spxpy q1 then
tinc pzitemp stacpr5i 2dpzpx
sta spzpx

tinc riziyl gPrzPry
tinc riym ryg
endif
! if spxpy q2 then
! tinc riym ryb
! endif
if spxpy q2 then
tinc riziyl bprzpry
tinc pzitemp stacpr5i 2dpzpxb
endif
endif
!
!-----Proj.-----
!
TINC SPZF ZP
TINC SPYF YP
TINC SPRF RP
TINC psnn SUMP
TINC PIZ PIY PZY
STA PIZIY
TINC PIZ PZZ
TINC PIY PYY
!
!=====GATES=====
!
tinc ripxy ptrans
tinc stacpr5i tacpr5m
tinc riym py5m
tinc pzitemp pz5m
END

```

References

- [1] J. Ullrich *et al.* , Comments At Mol. Phys. **30**, 285 (1994)
- [2] R. Moshhammer *et al.*, Nucl. Instrum. Methods Phys. Res. B **108**, 425 (1996)
- [3] B.P. Paolini and M. A. Khakoo, Rev. Sci. Instrum. **69**,3132 (1998)
- [4] M. Abdallah *et al.*, Phys. Rev. A **57**,4373 (1998)
- [5] E. Y. Kamber *et al.*, Phys. Rev. A **60**, 2907 (1998)
- [6] M. A. Abdallah *et al.*, Phys. Rev. A **58**, 2911 (1998)
- [7] Boudjema *et al.*, J. Phys. B **21**, 1603 (1988)
- [8] C. Harel, H. Jouin, J. Phys. B **21**, 859 (1988)
- [9] T. G. Lee, C. D. Lin, Phys. Rev. A **61**, 062713 (2000)
- [10] R. E. Olson, Phys. Rev. A **27**, 1871 (1983)
- [11] T. G. Winter and C. D. Lin, Phys. Rev. A **29**, 3071 (1984)
- [12] S. Yu Ovchinnikov, J. H. Macek, Phys. Rev. Lett. **75**, 2474 (1995)
- [13] E. Sidky and C.D. Lin, Phys. Rev. A **65**, 012711 (2001)
- [14] D. R. Schultz *et al.*, Phys. Rev. A **65**, 052722 (2002)
- [15] R. Dörner *et al.*, Phys. Rev. Lett. **77**, 4520 (1996)

- [16] M. A. Abdallah *et al.*, Phys. Rev. Lett. **81**, 3627 (1998)
- [17] W. Fritsch, C. D. Lin, Phys. Rev. A **27**, 3361 (1983)
- [18] N. Bohr, J. Lindhard, K. Dan, Vid. Sel. Mat. Phys. Medd. **28**, 1 (1954)
- [19] A. Niehaus, J. Phys. B, **19**, 2925 (1986)
- [20] H. Knudsen, H. K. Haugen, P. Hvelplund, Phys. Rev. A **23**, 597 (1981)
- [21] F. Bliiek, Ph. D. dissertation, Kernfysisch Versneller Insituut, Groningen, (1997)
- [22] C. L. Cocke, private communication
- [23] W. Fritsch, in *Review of Fundamental Processes and Applications of Atoms and Ions*, edited by C. D. Lin, (World Scientific, Singapore, 1993)p. 239
- [24] M. Pieksma, S. Yu Ovchinnikov, J. Phys. B **27**, 4573 (1994)
- [25] M. P. Stöckli *et al.*, Rev. Sci. Instrum., **67**, 1162 (1996)
- [26] E. D. Donets, in *The Physics and Technology of Ion Sources*, edited by I. G. Brown, (John Wiley and Sons, New York, 1989) p. 245
- [27] M. Abdallah, Ph.D. dissertation, Kansas State University, (1997)
- [28] Idaho National Engineering Laboratory, EG and G Idaho, Inc. Idaho Falls, ID 83415
- [29] J. Slevin, W. Stirling, Rev. Sci. Instrum. **52**, 1780 (1981)
- [30] M. V. Frohne, Ph. D. dissertation, Kansas State Univesity, (1994)
- [31] T. G. Lee, private communication
- [32] J. P. Giese *et al.*, Phys. Rev. A **38**, 4494 (1988)
- [33] T. Weber *et al.*, J. Phys. B **33**, 3331 (2000)
- [34] E. Edgü-Fry *et al.*, J. Phys. B **35**, 2603 (2002)

- [35] Physicon Corporation, 12 Hendrick Road, Wareham 02571, Massachusetts
- [36] E. Sidky, C. Illescas, C. D. Lin J., Phys. B **34**, L163 (2001)
- [37] J. Macek, private communication
- [38] E. Sidky, C. Illescas, C.D. Lin, Phys. Rev. Lett. **85**, 1634 (1999)